Structural Changes in Glasses under Periodic Shear Deformation

Saheli Mitra

université PARIS-SACLAY

Structural Changes in Glasses under Periodic Shear Deformation

Modifications Structurelles des Verres Sous Déformation Périodique par Cisaillement

Thèse de doctorat de l'université Paris-Saclay

École doctorale n°564 Physique de l'Ile-de-France (PIF)
Spécialité de doctorat: Physique
Unité de recherche : Université Paris-Saclay, CNRS, Laboratoire de Physique des Solides, 91405, Orsay, France
Référent : Faculté des sciences d'Orsay

Thèse présentée et soutenue à Paris-Saclay, le 23/03/2021, par

Saheli MITRA

Composition du Jury

Martin LENZ Directeur de recherche, LPTMS, Université Paris-Saclay	Président
Cristiano DE MICHELE Maître de conférences, (HDR), "Sapienza" University of Rome	Rapporteur & Examinateur
Emanuela DEL GADO Maître de conférences, (HDR), Georgetown University	Rapporteuse & Examinatrice
Francesco PIAZZA Professeur, Université d'Orléans	Examinateur
Mehdi BOUZID Chargé de recherche, Laboratoire 3SR, Grenoble	Examinateur

Direction de la thèse

Giuseppe FOFFI Professeur, LPS, Université Paris-Saclay	Directeur de thèse

Thèse de doctorat

NNT : 2021UPASP027

I dedicate this thesis to my family, my bosom friends and to all those young minds who once stared their doctoral with high aspirations and love for science.

Acknowledgements

As I have been writing my thesis, wrapping more than three years of work, I feel I have been blessed with wonderful people in my life, whom I would like to acknowledge.

Firstly I would like to express my deepest gratitude to my supervisor Prof. Giuseppe Foffi, LPS, Université Paris-Saclay. He has guided me in every step and during my thesis writing told me numerous times that I can contact him with any possible needs that I might have. The first time we met was over a Skype interview for the selection which later followed by a second interview by Prof. Srikanth Sastry, JNCASR, India. I thank you both for giving me this opportunity to explore working with you.

My sincere thanks to Centre Franco-Indien pour la Promotion de la Recherche Advancée (CEFIPRA) for funding my thesis. Specially many thanks to Sathidevi who helped me a lot when I needed extension. I thank Miss Simona, Campus France who handled my file here in France. I thank my doctoral school EDPIF (Ecole Doctorale Physique en Ile de France), my university Université Paris-Saclay and my laboratory Laboratoire de Physique des Solides (LPS) for accommodating me and providing me all the facilities to do my research work. During my PhD I annually presented our works to Prof. Francesco Zamponi, ENS, Paris and to Prof Marc Gabay, LPS, I thank them for their inputs in the progress of the thesis. I am thankful to my jury members for the evaluation of the thesis.

I thank Google Scholar, SciHub, arXiv, researchgate that gives PhD students easy access to journals. Stack Overflow and other online resources that helps with quickly finding an answer to fix a code. I have used Overleaf throughout for all the writings including this thesis. I thank all the free access providers.

When I applied for the doctoral position I was in my last semester of masters, working in my M.Sc. thesis with Prof. Krishna Kumar, IIT Kharagpur. I thank him for his recommendation. The other person who recommended me is Dr. Saugata Bhattacharyya. SB Sir has been a constant source of inspiration since my bachelors at Vidyasagar College, University of Calcutta. I thank you, you have always believed in me and motivated me.

I thank Prof. Sastry and JNCASR for hiring me as an R&D assistant for three months prior coming to France that gave me an idea about my research field. Students in his group, Vinutha, Anshul, Monoj da, Pallabi di, Saurabh, Varghese, Yagyik and later Himangsu were very friendly. I ended up working with Anshul and I thank him for pushing me and helping me in every way in the project.

I joined my lab LPS in October, 2017. The very first day Giuseppe was waiting for me at the Orsay-Ville station to receive me and take me to the lab. It was a time when I was unaware even about how to use the ticket inside the bus as we didn't have punching machines back in India and he showed me how to! He helped me with all the

official things at the beginning, introduced me to the people. I thank lab directory for the beautiful office I had, the powerful clusters I used and also for the funding support for the summer schools. I thank Veronique, Marie-France, Christoph, Sophie, Eric, Ilan for taking care of basic official necessities. Marie-France has been kind to help me with my french learning but poor me, I still cannot! Sorry to you.

Our theory group is very dynamic and welcoming. In our small cluster of people doing soft-matter, Giuseppe, Frank, Rik, Claudia, Susana and I used to go to lunch together at the canteen and the discussions would range from science to movies! I have felt Giuseppe to be the driving force in this dynamics. I thank you for bearing with me for three years. Claudia and I shared the office and she was like a wise post-doc willing to share her knowledge. I thank her for all the useful discussions. Susana and I became such good friends, we went to vacations together, we would do our groceries together and also work together. First time I worked with her was in a joint project with Frank and Laura Filion. I thank them and Emanuele for including me in their project. I really appreciate Frank's way of doing science. Rik has always advised me on how to prepare for presentations and I thank him for all his suggestions. I am thankful to Anuradha ma'am, she is very supportive and warm, we used to have small picnics with her. Thank you ma'am for your care. Latter Ettiene and Marina joined the group and I enjoy our discussions, thank you. For over one year I have been having coffee breaks with Dibya, Uma, Sougata, Subodh and Suvam. Thank you guys, I had a good time.

There are some friendships that initiated at the lab and then emerged into beautiful personal relationships. I am talking about my Bengali friends. Thanks to the "Bong Connection" I found myself this group of loving people who have become like a family to me. Thank you Pabitra da, Debasmita di, Rajesh da, Sonima di, Dibya da, Riya, Aatreya, Debdipta, Subrata Da. Our gatherings with food and "Adda" are the perfect stress relievers. Probably I irritated most Dibya da with all the unnecessary details of my personal life and he is like a patient elder brother guiding and misguiding me all the time.

At the beginning Deepanjan was there for me to cope with the changes, living far away from my family. Later there was a time when I struggled with both my professional and personal life and somehow depression got a hold of me. At that time Prithwijoy, my oldest friend over ten years would call me several times a week and help me deal with it. I thank him as he was a true friend in hard times. I am thankful to my friends Joydeep, Tanwistha and Indranil for keeping in touch. I would also like to acknowledge Mumpi didi, Sourav da, Suprita di, Subhadip da, Rajeev, Pranshu who guided me in different points of my career.

One constant support that I have is from my family. Baba and Maa calls me almost everyday to ask if i am doing okay. Baba would say even though he doesn't understand about my research all he wishes is for me to achieve great things in life. Maa keeps waiting for the news of my homecoming. In last years my sister Neha has managed everything at home. It is either Neha or Mumpi didi I would reach out to in any need of counsel. I thank you all. I also thank my extended family who I know wishes the best for me.

I have been staying in the same place during my PhD. I thank Mohammed and Loubna for renting a studio in their house. Thanks to Loubna, I have tasted many Moroccan cuisines that she would lovingly prepare.

Lastly but not the least I thank you Anish for making the last few months little less stressful, making me happy and being my friend.

Contents

Résumé

Un état vitreux se caractérise par un état arrêté de système amorphe qui a une limite d'élasticité finie. Les matériaux vitreux existent dans une large gamme d'échelles de longueur. Dans la préparation et l'application des verres, l'étude de la rhéologie est d'une importance capitale pour tester la réponse du matériau lorsqu'il est soumis à différentes conditions telles que la contrainte appliquée. Dans cette thèse, nous avons étudié par calcul les changements structurels dans des modèles de verre sous déformation périodique de cisaillement à travers la transition d'élasticité.

Nous avons travaillé sur deux modèles de formeurs de verre, à savoir le système Kob Andersen Lennard Jones (KALJ) à la densité $\rho = 1.2$ et le système répulsif Wahnström (WH) à la fraction de volume $\phi = 0.58$. Les matériaux vitreux en régime de surrefroidissement présentent un paysage énergétique potentiel accidenté rempli de minima, maxima et points de selle locaux. Avec le temps, le système évolue et explore cette surface énergétique complexe. Au départ, nous avons équilibré notre système à certaines températures, puis nous avons minimisé l'énergie à une température nulle. Ainsi, nous nous retrouvons avec des configurations appartenant à un minimum local. Les structures minimales locales sont connues comme étant les structures inhérentes (IS) et elles représentent le verre. Ensuite, nous cisaillons le verre en limite athrémique selon le protocole AQS (Athermal Quasi Static) pour de nombreux cycles de déformation avec une certaine amplitude de déformation γ_{max}. Un cycle complet sera une déformation $\gamma = 0 \rightarrow \gamma_{\max} \rightarrow 0 \rightarrow -\gamma_{\max} \rightarrow 0$, où strain $\gamma = \Delta L/L$, L étant la longueur de la boîte. Fig.1 est une représentation schématique du protocole de déformation.

En raison de la déformation cyclique par cisaillement, le système atteint un état d'énergie stable. Pour les valeurs faibles de $\gamma_{\max}$, ces états stables sont des états d'absorption. Les particules se réarrangent localement pendant un cycle de déformation et reviennent à leur position initiale à la fin du cycle. Mais si la valeur $\gamma_{\max} > \gamma_{\mathrm{y}}$, au-dessus de la limite, le système devient diffusif. Les particules subissent de grands réarrangements irréversibles et ne reviennent pas à leur position initiale. Il est intéressant de noter que ces réarrangements plastiques sont corrélés et forment une bande localisée de particules avec une forte valeur de déformation. C'est ce qu'on appelle le shear banding ou la localisation de la déformation. Dans la partie gauche de la figure 2, les énergies en régime permanent du système KALJ ont été montrées comme une fonction de $\gamma_{\max}$ à travers $\gamma_{\mathrm{y}} \approx 0,07$. Nous pouvons observer une transition brutale de l'état absorbant à l'état diffusant. Au-dessus de l'état diffusant, le système est constitué d'une

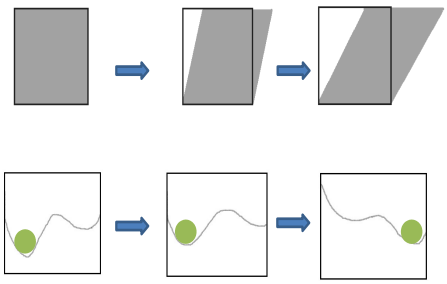

Figure 1: Schéma de l'évolution du paysage énergétique potentiel avec déformation de la boîte de simulation. Dans AQS, la boîte est déformée par petits pas de $d\gamma$ suivi d'une minimisation de l'énergie. Avec une grande déformation, le système passe à un nouveau minimum d'énergie.

bande de cisaillement, illustrée à droite, Fig. 2. Les particules rouges formant la bande ont une mobilité beaucoup plus grande que les particules bleues. L'énergie à l'intérieur du SB est également plus élevée par rapport au reste des systèmes [1].

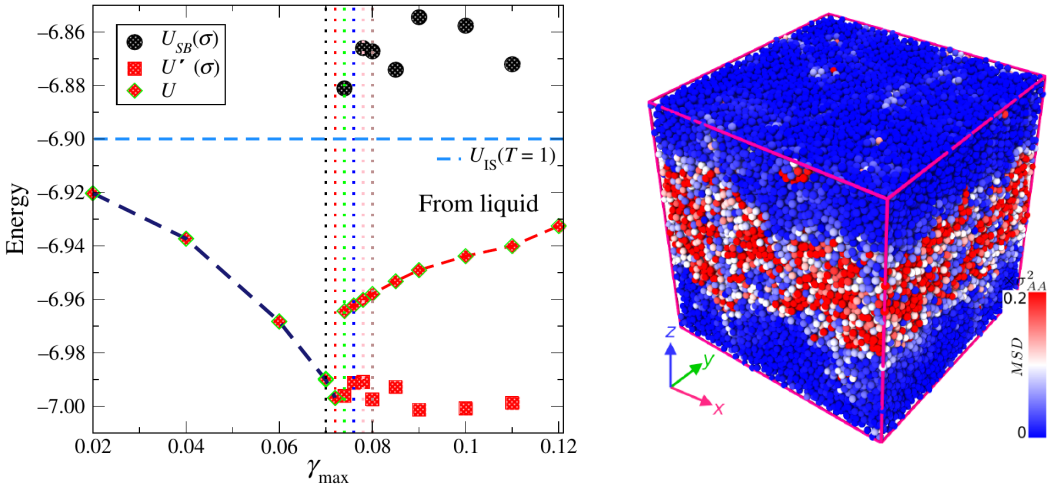

Figure 2: A gauche : Energie à l'état stable du système KALJ initialement préparé à haute température $T = 1$ et densité $\rho = 1.2$ en fonction de l'amplitude de la déformation γ_{max}. En dessous du rendement ($\gamma_y \approx 0,07$), l'énergie en régime permanent U diminue, et au-dessus du rendement, elle augmente. Mais une analyse plus approfondie à l'intérieur et à l'extérieur de la bande de cisaillement montre que l'énergie à l'intérieur de la bande de cisaillement $U_{SB}(\sigma)$ est beaucoup plus élevée que l'énergie globale du système. Mais, loin de la bande de cisaillement, $U'_{SB}(\sigma)$ l'énergie reste au même niveau bas de γ_y. C'est vrai : Bande de cisaillement trouvée dans l'état stable de $\gamma_{\max} = 0.09$. Les particules sont colorées en fonction de leurs déplacements entre deux cycles consécutifs [1].

Dans cette thèse, *(i)* nous avons étudié les changements structurels à long terme dans les verres à travers le rendement du contexte de "l'hyperuniformité" dans le système KALJ. *(ii)* Dans les états stables, nous avons également examiné les changements de l'ordre structurel local à travers la céder et sa relation avec les réarrangements plastiques dans le système WH. Dans les deux cas, nous avons analysé de façon cruciale les systèmes en présence

de bandes de cisaillement.

Hyperuniformity

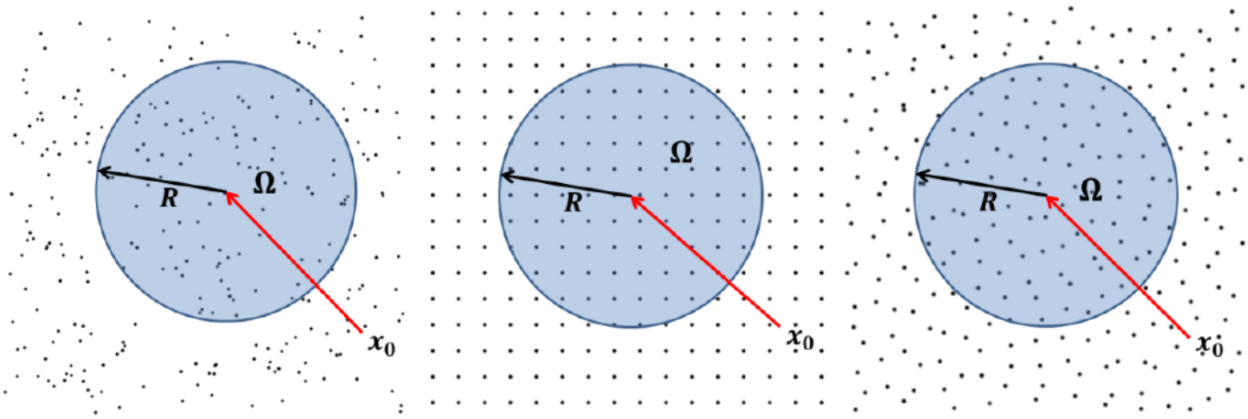

Figure 3: Représentation schématique de la fenêtre d'échantillonnage Ω de rayon R dans trois types de systèmes, de gauche à droite : système désordonné aléatoire, système ordonné et système désordonné hyperuniforme. x_0 est le centre de la fenêtre [2].

L'hyperunimormité dans un système englobe la suppression des fluctuations de densité à de grandes échelles de longueur. À titre d'exemple, nous pouvons nous référer aux différents types de distributions de points présentés dans la Fig. 3. Si une fenêtre sphérique de taille R est placée dans différentes parties du système, nous aurons des fluctuations dans la densité du nombre de points à l'intérieur de la fenêtre. Nous pouvons définir la variance de la densité de nombre $\rho(R)$,

$$\Delta^2(R) = <\rho(R)^2> - <\rho(R)>^2 . \tag{1}$$

Pour une distribution aléatoire de type Poisson en dimension d, $\Delta^2(R) \sim R^{-d}$, alors que pour un arrangement ordonné $\Delta^2(R) \sim R^{-(d+1)}$. Le système désordonné hyperuniforme est une classe spéciale de systèmes se situant entre un système aléatoire et un système ordonné où la variance de densité décroît plus rapidement que R^{-d}. Pour une configuration ponctuelle, la suppression de la variance de densité du nombre dans la limite des grandes longueurs d'onde est liée au facteur de structure de disparition dans la limite des vecteurs de basses ondes. Pour les configurations de points hyperuniformes, comme $k \to 0$, $S(k) \sim k^{\alpha} \to 0$. Pour l'exposant d'hyperuniformité $0 < \alpha < 1$, les échelles de variance de densité numérique sont $R^{-(d+\alpha)}$. En équilibre thermique, $S(0)$ est lié à la compressibilité χ_T.

Les états hyperuniformes de la matière ont été présentés comme un nouvel état exotique de la matière. Au cours des deux dernières décennies, l'hyperuniformité a été découverte dans de nombreux systèmes, y compris des systèmes biologiques, et en référence à des transitions de phase hors équilibre. Pour les systèmes entraînés avec des transitions d'état absorbant à diffusif, les états absorbants se sont avérés hyperuniformes. Dans cette thèse, nous étudions pour la première fois l'hyperuniformité dans un système de verre piloté. Nous travaillons avec

le système KALJ préparé à une densité de $\rho = 1.2$ et une température de 1.0. Pour ce système sous cisaillement cyclique en limite AQS, l'amplitude de rendement est de $\gamma_{\max} \approx 0.07$. Nous étudions l'hyperuniformité en calculant la compressibilité isotherme définie pour les systèmes binaires, $\tilde{\chi}_{\mathrm{T}}(\mathrm{k}) = \rho k_B T \chi_T(k)$. Pour l'hyperuniformité, $\tilde{\chi}_{\mathrm{T}}(\mathrm{k}) \sim k^{\alpha}$ dans la limite inférieure de k. Extrait de la figure 4 (à gauche), nous constatons que dans les états absorbants, $\tilde{\chi}_{\mathrm{T}}(\mathrm{k}) \sim k^{\alpha \sim 0,4}$ est hyperuniforme. Cependant, au-dessus du rendement, il existe des fluctuations de densité élevées comme le reflète la remontée de $\tilde{\chi}_{\mathrm{T}}(\mathrm{k})$ au niveau du vecteur d'onde le plus bas. Une autre chose à noter est que l'hyperuniformité s'étend aux échelles de longueur finie, aux vecteurs d'onde les plus bas $\tilde{\chi}_{\mathrm{T}}(\mathrm{k})$ s'écarte de l'ajustement de la loi de puissance et atteint une valeur finie. Ce type de comportement a été signalé pour de nombreux autres systèmes, dont on sait qu'il est effectivement hyperuniforme.

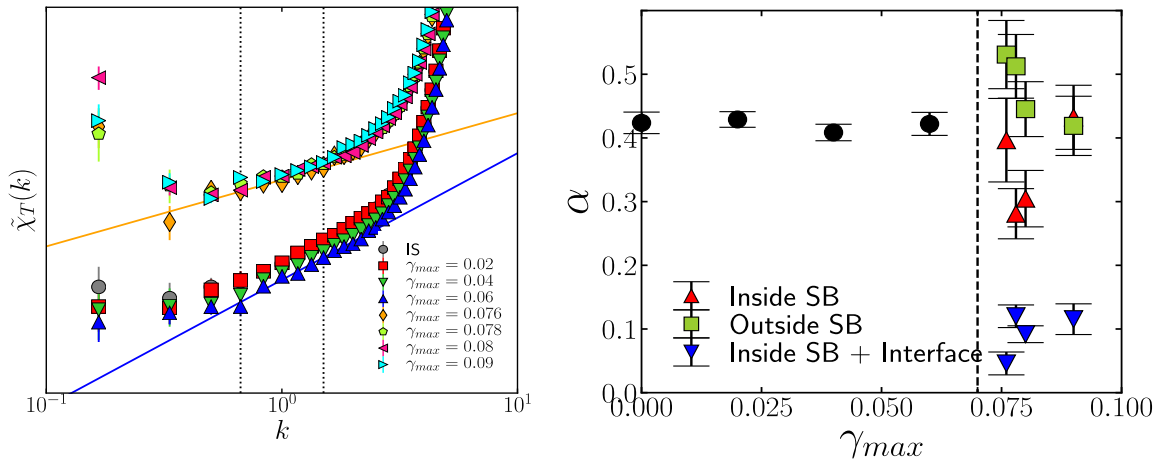

Figure 4: A gauche : Compressibilité $\tilde{\chi}_T(k)$ pour les cas d'amplitudes de cisaillement γ_{max} au-dessous et au-dessus de l'amplitude critique de rendement $\gamma_y \simeq 0,07$ sont indiqués avec des symboles différents. Les données relatives aux IS ont également été incluses. Dans les cas ci-dessus, $\tilde{\chi}_T(k)$ a été déplacé vers le haut pour une meilleure visibilité. Les lignes pleines (bleu et orange) montrent la loi de puissance adaptée aux courbes de compressibilité. Les lignes verticales en pointillés marquent le régime du vecteur d'onde ajusté à la loi de puissance k^{α}.
A droite : L'exposant de variance de la densité numérique α (voir le texte pour plus de détails) pour les cas où γ_{max} est inférieur à l'amplitude de rendement γ_y sont représentés par des cercles noirs. Lorsque l'interface est incluse, l'exposant tombe à de faibles valeurs indiquant un manque d'hyperuniformité. Séparément à l'intérieur et à l'extérieur de la bande de cisaillement, le système est hyperuniforme.

Nous avons également calculé $\Delta^2(R)$ dans le système en présence d'une bande de cisaillement. Pour $\gamma_{\max} > \gamma_{\mathrm{y}}$, nous avons extrait l'exposant d'hyperuniformité α pour les fenêtres d'observation placées dans les sous-volumes à l'intérieur de la bande de cisaillement, à l'extérieur de la bande de cisaillement et pour un cas où l'interface entre ces deux régimes a été considérée. Les résultats sont présentés dans la partie droite de la figure 4. Ci-dessous, le rendement, $\alpha \approx 0.4$. Au-dessus du rendement, les côtés intérieur et extérieur du système SB restent hyperuniformes. Lorsque l'interface est prise, l'hyperuniformité est perdue, ce qui est cohérent avec les résultats obtenus par la reprise de la compressibilité pour l'ensemble du système. Par conséquent, nous concluons qu'au-dessus du rendement, c'est l'interface qui perturbe l'hyperuniformité du système global.

Structure locale et plasticité

En cas de déformation par cisaillement, le paysage énergétique potentiel du système vitreux change lentement, comme le montre le panneau inférieur de la figure 1. Pour une amplitude de cisaillement suffisamment importante, un minimum local disparaît, entraînant une instabilité mécanique dans le système. En conséquence, les particules se déplacent localement à la recherche d'un nouveau minimum d'énergie. Pour un système amorphe, l'endroit et la manière dont ces réarrangements se produiront présentent un intérêt fondamental. Il y a eu de nombreuses tentatives pour trouver des paramètres d'ordre structurel local afin de prédire où les réarrangements se produiront. Dans cette thèse, nous avons choisi deux descripteurs structurels pour répondre à la question de savoir si, dans des états stables de cisaillement cyclique, les structures locales jouent un rôle quelconque dans la détermination des particules qui auront de grands déplacements pendant un cycle de déformation. Nos descripteurs sont les suivants :

Tétrahédralité dans les structures locales n_{tet}

La tétrahédraalité n_{tet} mesure pour chaque particule localement combien d'amas tétraédriques elle est impliquée. n_{tet} a été introduit pour corréler la structure locale avec l'hétérogénéité dynamique dans le régime vitreux des mélanges de sphères dures [3]. Il a été constaté que des valeurs plus élevées de n_{tet} sont bien corrélées avec les particules se déplaçant plus lentement.

Deux entropie excédentaire du corps S_2

L'entropie de deux corps en excès S_2 peut être calculée à partir des fonctions de distribution radiale mollifiée par particule [4]. S_2 mesure la perte d'entropie due aux corrélations positionnelles, une valeur négative inférieure de S_2 correspond à une structure plus ordonnée. Nous avons travaillé sur le système WH sous déformation de cisaillement cyclique pour lequel l'amplitude de rendement est de $\gamma_{\text{y}} \approx 0,06$. Nous avons cisaillé des verres en utilisant le protocole AQS, initialement préparés à la fraction de volume $\phi = 0.58$ et aux températures $T = 0.7$ et $T = 1.5$. Dans des états stables, nous avons mesuré les déplacements non-affines D^2_{min} des particules pendant un cycle de déformation, introduit par Falk et Langer [5],

$$D^2_{min} = \frac{1}{n}\sum_n [(r_j(t) - r_i(t)) - \Gamma(r_j(0) - r_i(0))]^2. \tag{2}$$

Ici, $r_{i,j}(0)$ est la position des particules au début d'un cycle de déformation et $r_{i,j}(t)$ est leur position dans la boîte déformée au moment t, ce qui renvoie aux étapes de déformation de l'AQS (voir annexe) pendant un cycle. La somme est sur les voisins et la matrice Γ est telle qu'elle minimise les déplacements carrés moyens réels des atomes voisins par rapport à ce qu'auraient été leurs déplacements sous un cisaillement uniforme. Nous avons

classé les 5% de particules les plus "mobiles" et les 5% de particules "statiques" en notant leurs valeurs maximales de $\mathrm{D}^2_{\mathrm{min}}$ pendant un cycle de déformation. Ensuite, nous avons comparé les descripteurs structurels des particules mobiles et statiques au début d'un cycle. Pour un cas, $T = 0,7$ dans un état stable de $\gamma_{max} = 0,06$ les résultats sont présentés dans la Fig. 5. Les particules statiques ont une valeur moyenne inférieure de S_2 et une valeur supérieure de n_{tet}. Cela démontre en effet que les particules ayant des déplacements plus importants ont un environnement structurel local différent.

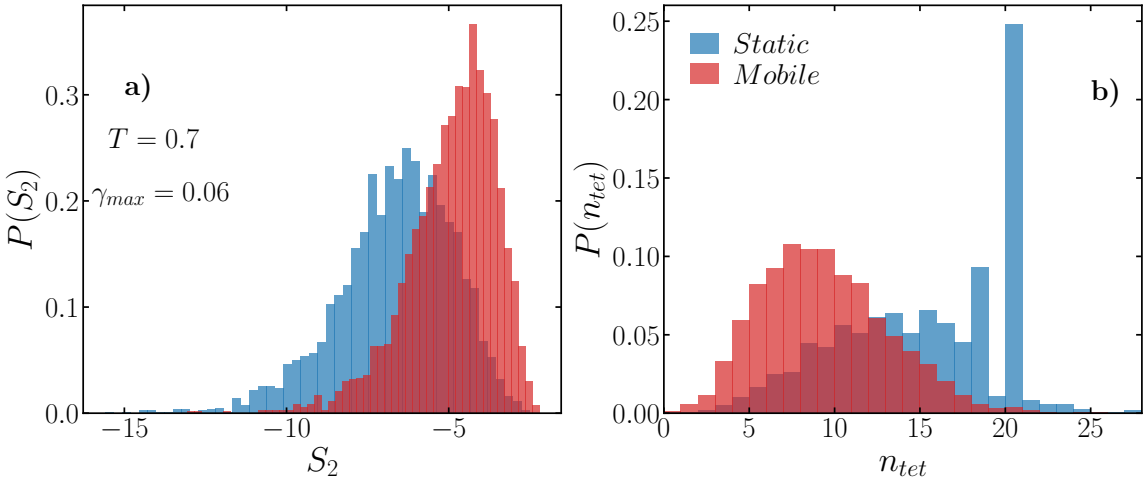

Figure 5: Pour le cas où $T = 0,7$ en régime permanent de $\gamma_{max} = 0,06$, distribution de S_2 en a) et de n_{tet} en b) au début d'un cycle, pour les particules ayant les valeurs de déplacement les plus faibles (bleu) et les plus élevées (rouge) $max(D^2_{min})$ à la fin d'un cycle.

Nous constatons également que dans les particules statiques, il y a une abondance de $n_{\mathrm{tet}} = 20$. Ceci est intéressant car un amas icosaédrique local peut être décomposé en tétraèdres de 20 et l'amas icosaédrique a été exploré pendant de nombreuses années en tant que structures localement favorisées en corrélation avec le ralentissement dynamique des verres. Au-dessus du rendement, les particules mobiles appartiendraient au régime de bande de cisaillement dynamique tandis que les particules statiques se trouveraient en dehors de la bande de cisaillement. Nous avons effectué une analyse de la classification topologique des amas (TCC) [6] en présence de la bande de cisaillement et avons spécialement calculé la variation spatiale de l'amas icosaédrique dans le système. Les résultats sont présentés dans la Fig. 6. Tout d'abord, le profil de déplacement carré moyen entre deux cycles consécutifs dans la direction Z est tracé. Cela montre la position de la bande de cisaillement dans le système. Ensuite, la fraction de particules impliquées dans le regroupement icosaédrique est tracée le long de la même direction Z. Nous constatons qu'en dehors de la bande de cisaillement, près de 30% des particules sont impliquées dans les amas icosaédriques. Mais en dehors de la bande de cisaillement, cette participation est négligeable. Nos résultats montrent une différence structurelle claire entre les sous-volumes du système en présence de la bande de cisaillement.

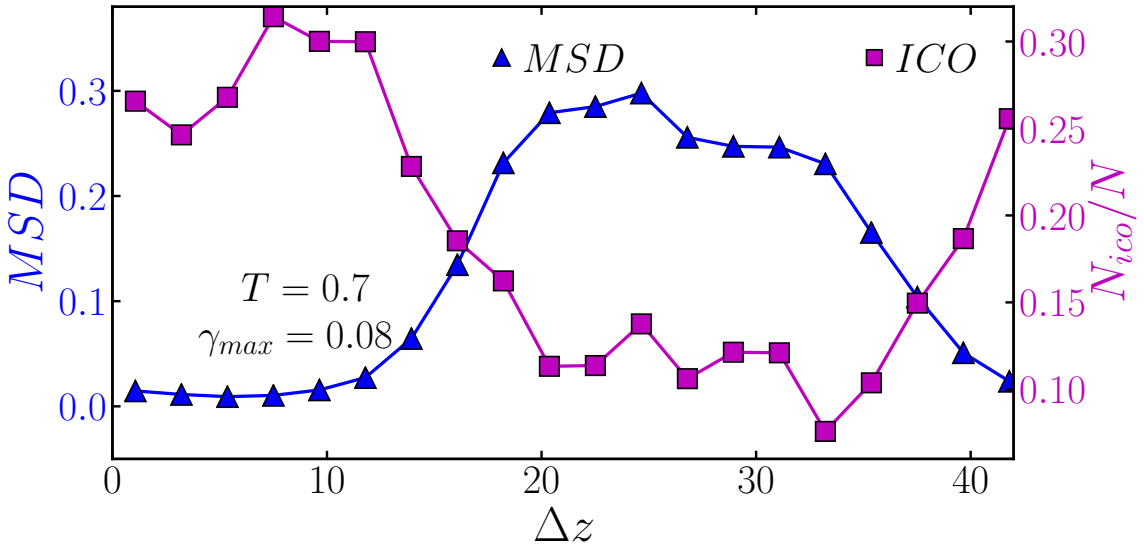

Figure 6: Pour le cas de $T = 0.7$ et $\gamma_{max} = 0.08$ en régime permanent, nous traçons le déplacement carré moyen des particules le long de Z (triangles bleus, capturant l'emplacement de la bande de cisaillement. Nous traçons également la fraction des particules impliquées dans l'amas icosaédrique le long de Z.

Summary

A glassy state is characterised as an arrested state of amorphous system that has a finite yield stress. Glassy materials exist through a wide range of length scales. In preparation and application purposes of glasses the study of rheology is of immense importance to test material's response when subjected to different conditions such as applied stress. In this thesis we have computationally studied structural changes in model glasses under periodic shear deformation across yielding transition.

We have worked on two models of glass formers, namely Kob Andersen Lennard Jones (KALJ) system at density $\rho = 1.2$ and repulsive Wahnström (WH) system at volume fraction $\phi = 0.58$. Glassy materials in supercooled regime has a rugged potential energy landscape filled with local minima, maxima and saddle points. With time system evolves and explores this complex energy surface. Initially we equilibrated our system at certain temperatures and then we minimized the energy at zero temperature. Thus we end up with configurations belonging to a local minimum. Local minimum structures are known to be the inherent structures (IS) and they represent the glass. Next we shear the glass in athremal limit following Athermal Quasi Static (AQS) protocol for many deformation cycles with certain strain amplitude γ_{max}. A complete cycle will be strain $\gamma = 0 \rightarrow \gamma_{\rm max} \rightarrow 0 \rightarrow -\gamma_{\rm max} \rightarrow 0$, where strain $\gamma = \Delta L/L$, L being the box-length. Fig.7 is a schematic representation of the deformation protocol.

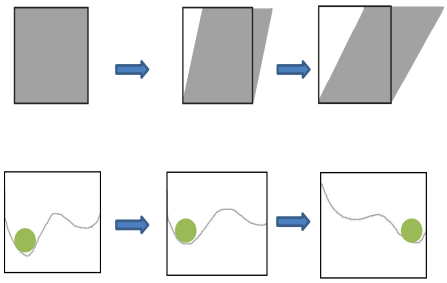

Figure 7: Schematic diagram of evolution of potential energy landscape with deformation of simulation box. In AQS, the box is deformed with small steps of $d\gamma$ followed by energy minimization. With large deformation, system jumps to new energy minimum.

As a result of cyclic shear deformation, the system reaches a steady energy state. For low $\gamma_{\max}$ values, these steady states are absorbing states. Particles locally rearrange during a deformation cycle and at the end of a cycle comes back to their initial positions. But if the $\gamma_{\max} > \gamma_y$, above yielding the system becomes diffusive. The particles undergo large irreversible rearrangements and fail to come back to their positions. Interestingly above yielding these plastic rearrangements correlate and forms a localized band of particles with high strain value. This is known as shear banding or strain localization. In the left of fig. 8, steady state energies of KALJ system have been shown as a function of $\gamma_{\max}$ across $\gamma_y \approx 0.07$. We can see a sharp transition from absorbing to diffusive state. Above yielding the system consists a shear band, shown in the right. The red particles forming the band have much higher mobility compared to the blue particles. The energy inside the SB is also higher compared to the rest of the systems [1].

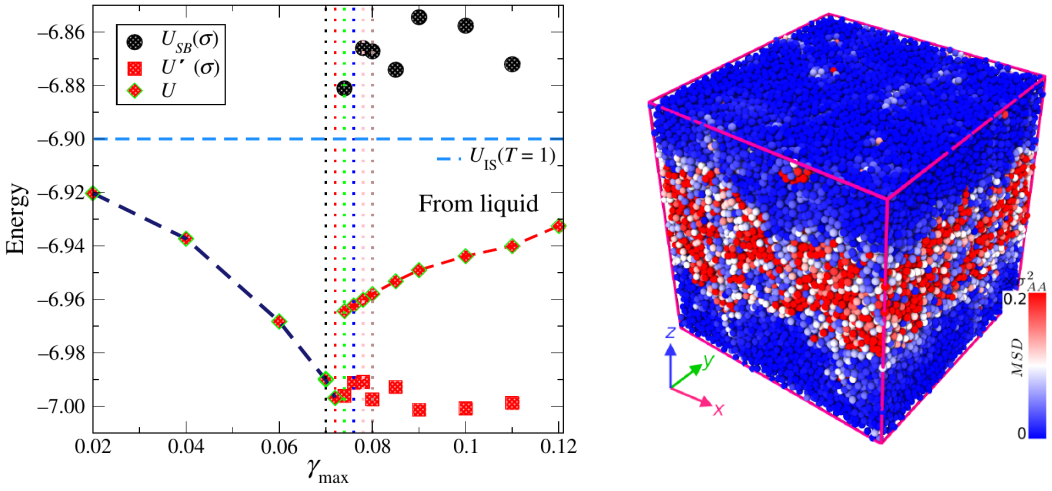

Figure 8: Left: Steady state energy of KALJ system initially prepared at high temperature $T = 1$ and density $\rho = 1.2$ as a function of strain amplitude γ_{max}. Below yielding, ($\gamma_y \approx 0.07$) steady state energy U decreases, and above yielding jumps to higher value. But a deeper analysis inside and outside of shear band shows that energy inside shear band $U_{SB}(\sigma)$ is much higher than the overall energy of the system. But, far from shear band, $U'_{SB}(\sigma)$ the enrgy remains at the same low level of γ_y. Right: Shear band found in the steady state of $\gamma_{\max} = 0.09$. Particles are coloured as per their displacements between two consecutive cycles [1].

In this thesis, *(i)* we have investigated long range structural changes in glasses across yielding from the context of "hyperuniformity" in KALJ system. *(ii)* In steady states, we have also examined changes in local structural order across yielding and its relation with plastic rearrangements in WH system. In both the problems, we have crucially analized the systems in presence of shear band.

Hyperuniformity

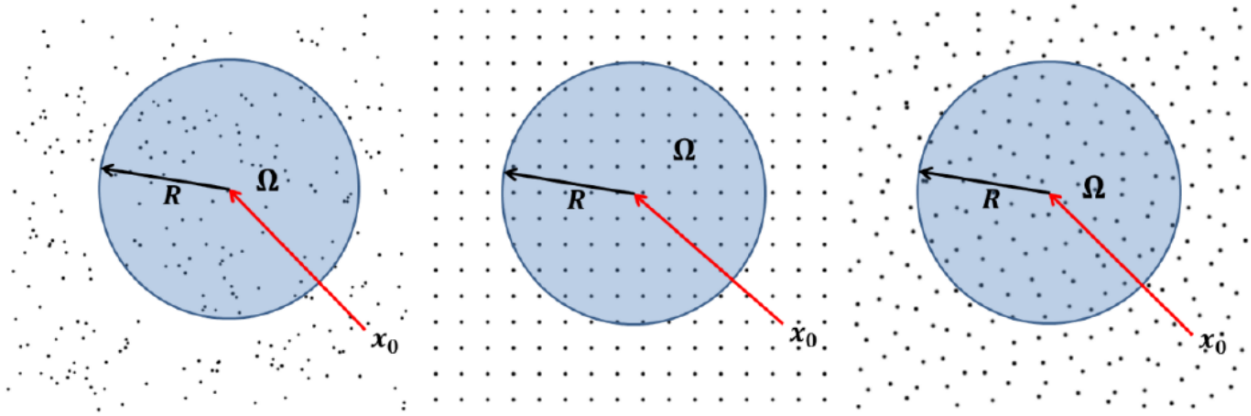

Figure 9: Schematic representation of sampling window Ω of radius R in three types of systems, from left to right : randomly disordered system, ordered system and hyperuniform disordered system. x_0 is the center of the window [2].

Hyperunimormity in a system encompasses the suppression of density fluctuations at large length scales. As an example we can refer to the different types of point distributions presented in Fig. 9. If a spherical window of size R is placed in different parts of the system, we shall have fluctuations in the number density of points within the window. We can define variance in number density $\rho(R)$,

$$\Delta^2(R) = < \rho(R)^2 > - < \rho(R) >^2 . \tag{3}$$

For a random Poisson type distribution in d dimension, $\Delta^2(R) \sim R^{-d}$, whereas for an ordered arrangement $\Delta^2(R) \sim R^{-(d+1)}$. Hyperuniform disordered system is a special class of systems lying in between a random and an ordered system where the density variance decays faster than R^{-d}. For a point configuration, suppression of number density variance in long wavelength limit is related to the vanishing structure factor in low wave vector limit. For hyperuniform point configurations, as $k \to 0$, $S(k) \sim k^\alpha \to 0$. For hyperuniformity exponent $0 < \alpha < 1$, number density variance scales as $R^{-(d+\alpha)}$. In thermal equilibrium, $S(0)$ is related to the compressibility χ_T.

Hyperuniform states of matter has been claimed to be a new exotic state of matter. For last two decades hyperuniformity has been discovered in many systems including biological systems and with reference to non equilibrium phase transitions. For driven systems with absorbing to diffusive state transitions the absorbing states have been found to be hyperuniform. In this thesis we first time investigate hyperuniformity in driven glass system. We work with KALJ system prepared at density $\rho = 1.2$ and temperature 1.0. For this system under cyclic shear in AQS limit, the yielding amplitude is $\gamma_{\max} \approx 0.07$. We study hyperuniformity by computing isothermal compressibility defined for binary systems, $\tilde{\chi}_{\mathrm{T}}(\mathrm{k}) = \rho k_B T \chi_T(k)$. For hyperuniformity, $\tilde{\chi}_{\mathrm{T}}(\mathrm{k}) \sim k^\alpha$ in low k limit. From Fig. 10 (left) we find that in absorbing states $\tilde{\chi}_{\mathrm{T}}(\mathrm{k}) \sim k^{\alpha \sim 0.4}$ is hyperuniform. However, above yielding there exists high density fluctuations as

reflected by the upturn of $\tilde{\chi}_{\mathrm{T}}(\mathrm{k})$ at lowest wave vector. Another thing to notice is that the hyperuniformity extends for finite length scales, at lowest wave vectors $\tilde{\chi}_{\mathrm{T}}(\mathrm{k})$ deviates from the power-law fit and attains a finite value. This kind of behaviour has been reported for many other systems, known has effectively hyperuniform.

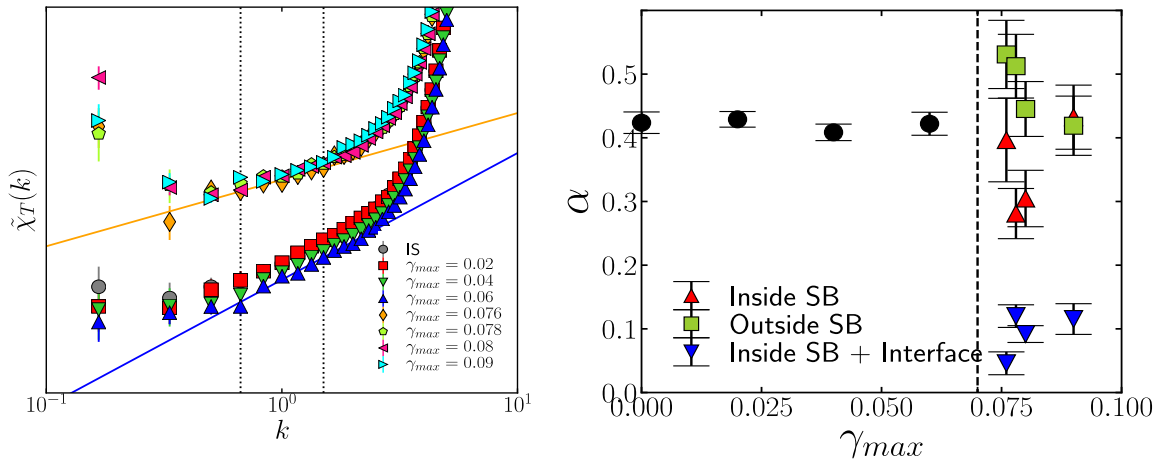

Figure 10: Left: Compressibility $\tilde{\chi}_T(k)$ for the cases of shear amplitudes γ_{max} below and above critical yielding amplitude $\gamma_y \simeq 0.07$ are shown with different symbols. Data for IS has also been included. In the cases above yielding, $\tilde{\chi}_T(k)$ has been shifted upwards for clear visibility. The solid lines (blue and orange) show the power law fit to the compressibility curves. The vertical dotted lines mark the wave vector regime fitted with the power law k^{α}. Right: Number density variance exponent α (see text for details) for the cases of γ_{max} below yielding amplitude γ_y are shown as black circles. When the interface is included, the exponent drops to low values indicating a lack of hyperuniformity. Separately inside and outside the shear band the system is hyperuniform.

We also calculated $\Delta^2(R)$ in the system in presence od shear band. For $\gamma_{\mathrm{max}} > \gamma_{\mathrm{y}}$, we extracted hyperuniformity exponent α for observation windows placed in the sub-volumes inside shear band, out side of shear band and for a case where the interface between these two regimes have been considered. Results are shown in the right of Fig. 10. Below yielding, $\alpha \approx 0.4$. Above yielding, inside and out side of SB system remains hyperuniform. When the interface is taken, hyperuniformity is lost, consistent with the results obtained from upturn in compressibility for the whole system. Therefore we conclude that above yielding it is the interface that disrupts hyperuniformity of the overall system.

Local structure and plasticity

Upon application of shear deformation the potential energy landscape of the glassy system slowly changes, as has been shown in the bottom panel of Fig. 7. For large enough shear amplitude a local minimum disappears causing mechanical instability in the system. As a result, locally particles rearrange in search for new energy minimum. For an amorphous system where and how these rearrangements will take place is of fundamental interest. There has been many attempts to come up with local structural order parameters to predict where the rearrangements will happen. In this thesis we have chosen two structural descriptors to address the question that in steady states of

cyclic shear if the local structures play any role in determining which particles will have large displacements during a deformation cycle. Our descriptors are as follows:

Tetrahedrality in local structures n_{tet}

Tetrahedrality n_{tet} measures for each particle locally how many tetrahedral clusters it is involved in. n_{tet} was introduced to correlate local structure with dynamic heterogeneity in glassy regime of hard sphere mixtures [3]. It was found that higher values of n_{tet} correlates well with the slower moving particles.

Two body excess entropy S_2

Two body excess entropy S_2 can be calculated from mollified radial distribution functions per particle [4]. S_2 measures the loss of entropy due to positional correlations, a lower negative value of S_2 corresponds to a more ordered structure.

We have worked on WH system under cyclic shear deformation for which the yielding amplitude is $\gamma_{\text{y}} \approx 0.06$. We sheared glasses using AQS protocol, initially prepared at volume fraction $\phi = 0.58$ and temperatures $T = 0.7$ and $T = 1.5$. In steady states we measured the non-affine displacements D^2_{min} of the particles during a deformation cycle, introduced by Falk and Langer [5],

$$D^2_{min} = \frac{1}{n}\sum_n [(r_j(t) - r_i(t)) - \Gamma(r_j(0) - r_i(0))]^2. \tag{4}$$

Here, $r_{i,j}(0)$ is the position of the particles at the beginning of a deformation cycle and $r_{i,j}(t)$ is their positions in deformed box at time t, which refers to the deformation steps of AQS (see appendix) during one cycle. The sum is over the neighbours and the matrix Γ is such that it minimizes actual mean square displacements of neighbouring atoms compared to what would have been their displacements under uniform shear. We classified the 5% most "mobile" and 5% "static" particles by noting their maximum values of D^2_{min} during one cycle of deformation. Then we compared the structural descriptors of mobile and static particles at the beginning of a cycle. For one case, $T = 0.7$ in steady state of $\gamma_{max} = 0.06$ the results are shown in Fig. 11. The static particles have lower mean value of S_2 and higher value of n_{tet}. This demonstrates indeed particles having larger displacements have different local structural environment.

We also find that in static particles there is an abundance of $n_{\text{tet}} = 20$. This is interesting because A local icosahedral cluster can be decomposed into 20 tetrahedrons and icosahedral cluster has been explored for many years as locally favoured structures in correlation with dynamic slow down of glasses. Above yielding the mobile particles would belong to the dynamic shear band regime whereas the static particles will lie outside of shear band. We performed

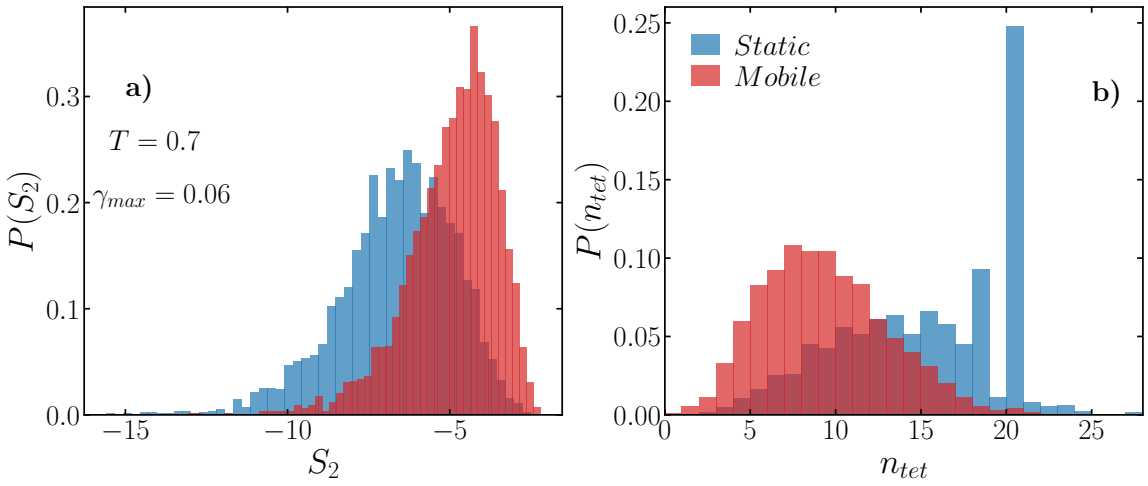

Figure 11: For the case of $T = 0.7$ in steady state of $\gamma_{max} = 0.06$, distribution of S_2 in a) and n_{tet} in b) at the beginning of a cycle, for particles with lowest (blue) and highest (red) values of displacements $max(D^2_{min})$ at the end of a cycle.

Topological Cluster Classification (TCC) [6] analysis in presence of shear band and specially computed the spacial variation of icosahedral clustering in the system. Result is shown in Fig. 12. First, mean square displacement profile between two consecutive cycles along Z direction is plotted. This shows the position of shear band in the system. Then fraction of particles involved with icosahedral clustering is plotted along the same Z. We find that outside shear band almost 30% of the particle has involvement with icosahedral clusters. But outside of shear band this is negligible. Our results show clear structural difference between sub-volumes of the system in presence of shear band.

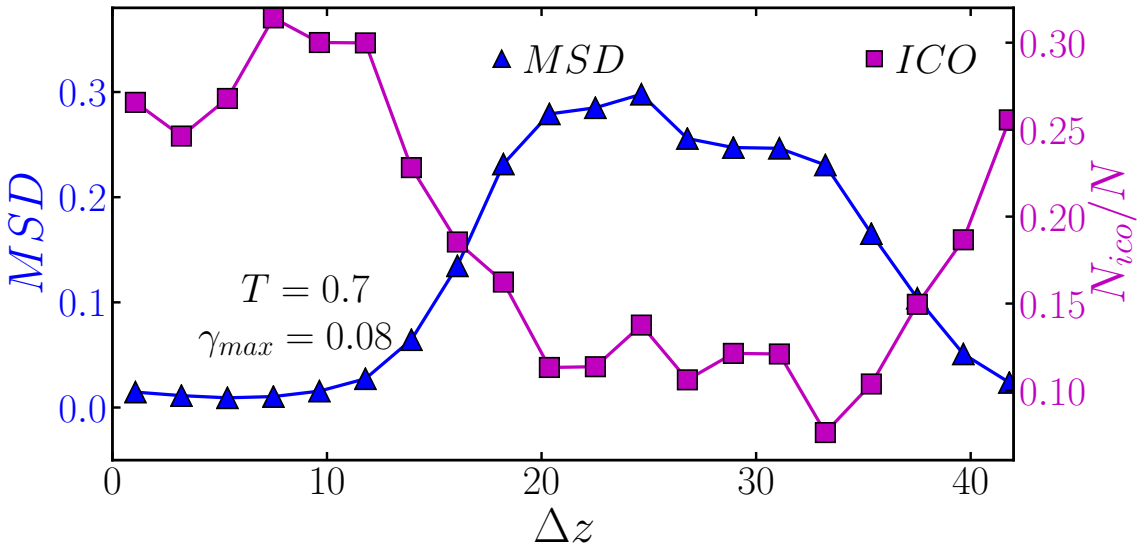

Figure 12: For the case of $T = 0.7$ and $\gamma_{max} = 0.08$ in steady state we plot mean square displacement of the particles along Z (blue triangles, capturing the location of shear band. We also plot fraction of particles involved in icosahedral cluster along Z.

Chapter 1

Introduction I: Glasses and response to shear deformation

1.1 The glass state

In the famous article "The Nature of Glass Remains Anything but Clear" by Kenneth Chang published in The New York times in 2008 the author quotes from the Nobel Prize-winning physicist Philip W. Anderson (1995),

The deepest and most interesting unsolved problem in solid state theory is probably the theory of the nature of glass and the glass transition.

In last decades there has been an immense amount of research articles dedicated to the understanding of glass transition. Theoretical advancements based on mean field approximations, mode coupling theories while are able to predict some crucial features of glass transitions, they are in no way complete [7]. Computer simulations have flourished the research as they give easy way to test the theories as well as perform experiments to predict qualitatively the phenomenological aspects of glasses under different conditions.

In general glasses are very long lived meta-stable states of matter which remain non-crystalline [8]. Glasses are amorphous, they have no long-range order like a liquid but they are practically solid. The main question of interest is that at the atomic level how can an amorphous arrangement give rise to finite yield stress, which is the characteristic of a solid phase, meaning solids resist the attempt to change their shapes.

Glasses involve a wide range of length scales. Our everyday life is filled with glassy materials. The obvious examples of glass people would give are probably that of the oxide glasses, such as window glass. Most common building block for the transparent glasses is silica SiO_2, which exists both in crystalline and amorphous state at room temperatures as shown in Fig. 1.1. Other examples of systems at glassy states will include metallic glasses, polymeric glasses, colloidal glasses involving a wide range of length scales [9].

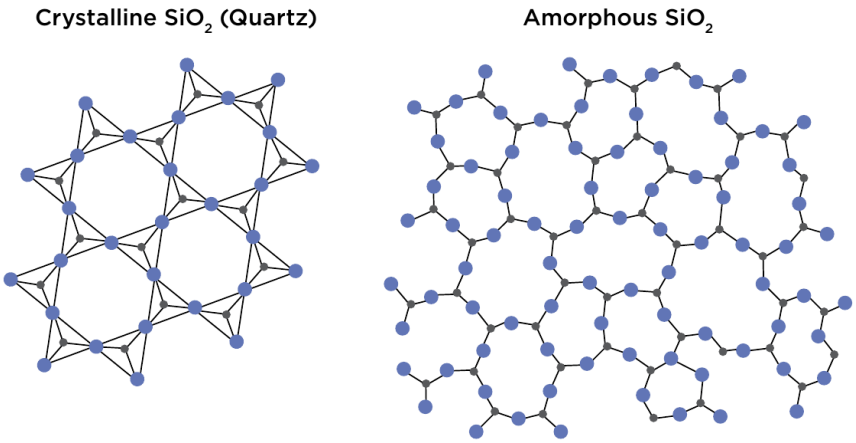

Figure 1.1: SiO_2 in crystalline and amorphous phase (glass). Blue circles represent oxygen atom and black circles are the Si atoms [10].

To make a glass usually the materials are melt at high temperatures and then it is rapidly cooled down to avoid crystallization. For example for silica the melting temperature is as high as $1700\,℃$. However, cooling rates, addition of other materials result in glasses with different physical properties . Fig. 1.2 shows a very typical phase diagram for glass transition. Glass transition occurs at temperatures lower than the melting temperature T_m. Melting temperature is a well defined fixed temperature for a material. At melting temperature, given enough time, the system crystallises and releases latent heat. Whereas, glass transition is a continuous process, there is no latent heat involved and there is no well defined glass transition temperature T_g. As shown in Fig. 1.2, T_g also depends on the protocol of obtaining the glass.

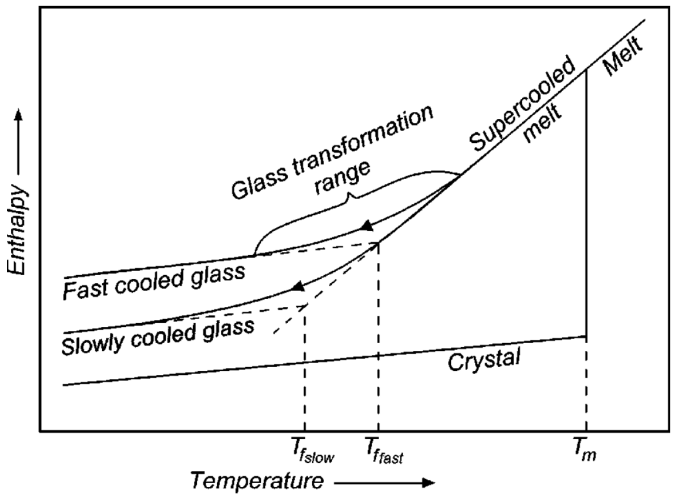

Figure 1.2: Schematic phase diagram of a glass forming liquid: enthalpy or equivalently volume versus temperature. Glass transition temperature $T_g = T_{fast}$ or T_{slow} depends on cooling rate. T_m is the melting temperature [11].

Glass transition temperature T_g is not related to a thermodynamic transition. It is a temperature below which the system has very high viscosity and very large relaxation time with respect to experimental time scale. Below T_g the dynamics slows down dramatically and physical properties slowly evolve to far from equilibrium states, known as "aging" of glass [12].

1.1.1 Changes of properties across glass transition

Upon fast cooling below the melting temperature glassy materials reach a metastable "supercooled" regime. This transition is accompanied by very rich phenomenological changes. We shall very shortly touch upon few key points following the review by Berthier and Biroli [7]. The time scale over which density fluctuations relax is of the order of picoseconds at T_m but at T_g it is of the order of $100s$. This increase of time scale τ_α is one of the signatures of glass transition. The mechanical properties also change dramatically as reflected by increase in viscosity η. At T_g the viscosity increases to the order of 10^{12} Pa.s, in contrast typical liquids have $\eta <\approx 0.1$. Conventionally T_g is chosen to be the temperature where η is close to 10^{12}.

The variation of relaxation time or viscosity as a function of temperature is given by the "Angel plot" [13] shown in Fig. 1.3.

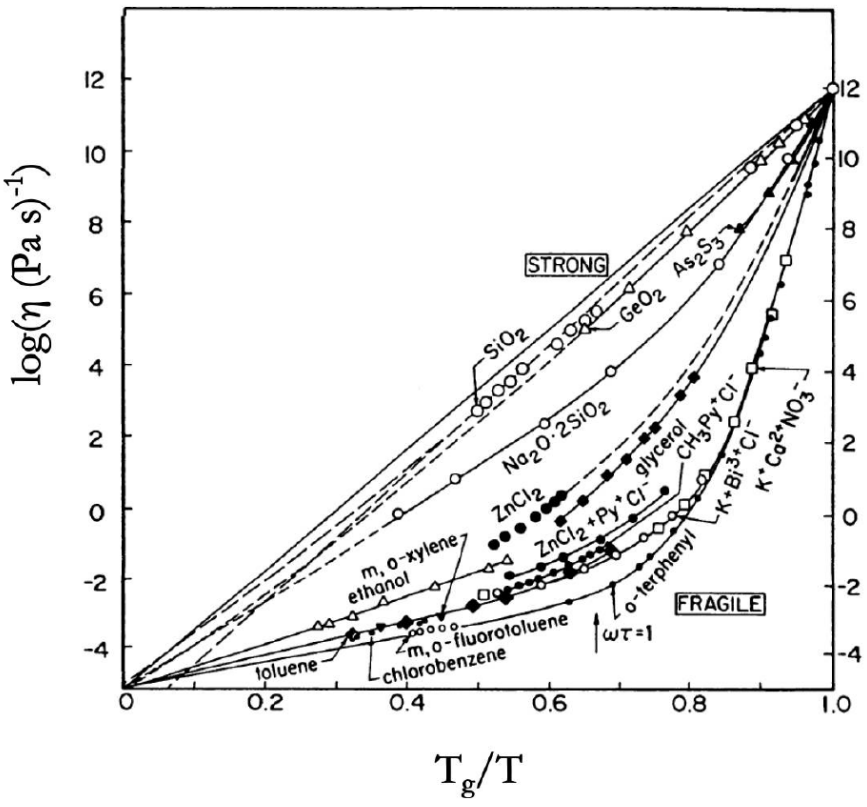

Figure 1.3: Viscosity with temperature scaled with glass transition temperature T_g for different systems. "Strong" glasses show Arrhenius type variation whereas "fragile" glasses show super-Arrhenius behaviour [13].

For "strong" glass formers viscosity and the relaxation time τ_α has the following "Arrhenius" behaviour with temperature T,

$$\eta \propto \exp\Big(\frac{E}{k_B T}\Big). \tag{1.1}$$

Here, k_B is the Boltzmann's constant and E gives a notion of effective activation energy accounting to local relaxation by breaking some kind of bond. The "fragile" glasses on the other hand shows a "super-Arrhenius" behaviour and The fit is given by Vogel-Fulcher-Tamman law (VFT),

$$\eta \propto \exp\Big(\frac{E}{k_B(T-T_0)}\Big). \tag{1.2}$$

This indicates that at a finite temperature T_0 the relaxation time and viscosity diverges. However there are other proposed functional forms for the fit [14], but experiments fail to universally choose one over others. In fragile glasses the glass formation has been suggested to be a collective phenomenon.

Another interesting observation was found regarding the excess entropy S_{ex}, a difference between system entropy from corresponding crystal. Extrapolating of S_{ex} for temperatures below T_g, one can obtain a finite temperature T_k, known as the Kauzmann temperature where S_{ex} becomes zero [15]. This means, below T_k entropy of the disordered system becomes less than the entropy of ordered crystal phase. However, S_{ex} is related to the configurational entropy and no fundamental theory restricts the glass phase to have lower S_{ex}.

Even though there is a diverging time scale at glass transition temperature T_g, this transition so far has not been connected to diverging length scale associated to static density correlation function. However, dynamic density correlation function undergoes significant changes across glass transition temperature. We can define intermediate scattering function $F(\mathbf{k},t)$ as,

$$F(\mathbf{k},t) = \Big\langle \frac{1}{N}\rho_{\mathbf{k}}(t)\rho_{-\mathbf{k}}(0)\Big\rangle. \tag{1.3}$$

Here $\rho_{\mathbf{k}} = \sum_{j=1}^{N} \exp(i\mathbf{k}\cdot\mathbf{r}_j)$ is the Fourier transform of density. The function measures decay of structural correlation with time corresponding to a length scale $\lambda \sim \frac{2\pi}{|\mathbf{k}|}$. Typically for $\mathbf{k} = \mathbf{k}_{peak}$, the value of the wave vector at the position of the first peak of static structure factor $S(k) = \Big\langle \frac{1}{N}\rho_{\mathbf{k}}(0)\rho_{-\mathbf{k}}(0)\Big\rangle$ is chosen which gives the idea how fast the closest neighbours decorrelate with time. In Fig. 1.4 intermediate scattering function for molten silica in supercooled regime is shown [16]. At low temperatures there are distinct regimes of interest. $F(\mathbf{k},t)$ at first decays quite fast, then a plateau appears followed by a second relaxation. The fast decay is the ballistic regime (short times), the plateau is the β relaxation (intermediate times) and finally the second decay is the α relaxation (long times). The plateau appears when the particles are stuck within the cages formed by its neighbours but eventually they break the cages decorrelates from their initial positions by α relaxation which accounts for the escape of the particles from the cages and the motion of the cages. Here it is worth to note that this cage effect is a descriptive idea that works at the level

of Mean Field Theory (MFT), which is pretty clear and applicable in colloidal hard spheres and remains strongly linked to Mode Coupling Theories (MCT) [17, 18, 19, 20]. The regime of α relaxation can be fitted to a stretched exponential function $\sim \exp(-(t/\tau_\alpha)^\gamma)$ and relaxation time τ_α can be extracted.

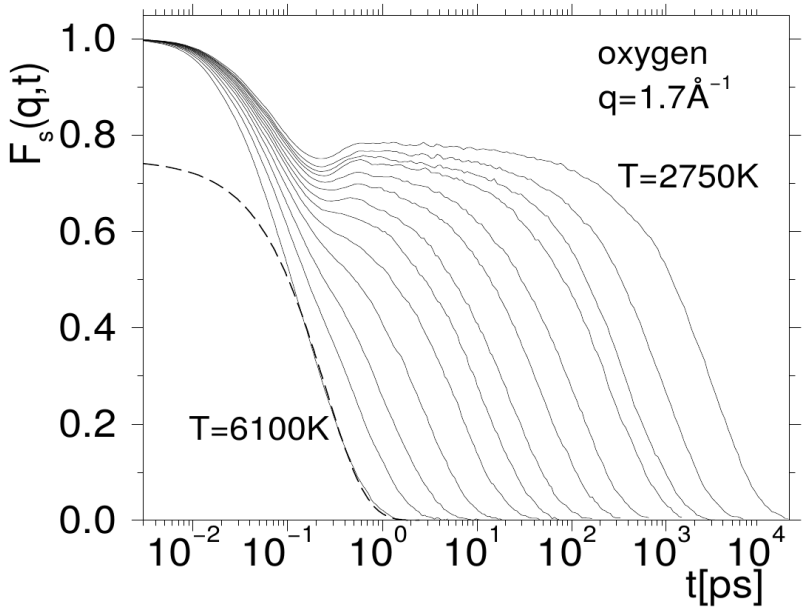

Figure 1.4: Self part of the intermediate scattering function $F_s(q,t)$ for oxygen atoms of a silica melt at different temperatures, corresponding to wave vector $q = 1.7\text{Å}^{-1}$ [16],

1.1.2 Potential Energy Landscape (PEL) view

The time evolution and flow properties of any N particle system originate from the interactions between the particles, given by a potential energy $\Phi = \Phi(\mathbf{R})$, where $\mathbf{R} = \{\mathbf{r}_1, .., \mathbf{r}_N\}$ are the particle coordinates. For example Φ can have effects of electrostatic interactions, polarization, hydrogen bonding, electron cloud repulsion etc and then as done in molecular dynamics simulations, Newton's equation of motion can be solved to track the particles in time. The potential energy surface is a rugged landscape as has been illustrated in Fig. 1.5 [21], full with local minima, maxima and saddle points. Minimas represent mechanically stable arrangement of the particles where all forces and torques are zero. The deepest minima correspond to zero temperature perfect crystal arrangements. Higher lying minimas meanwhile correspond to amorphous phases. System with equilibration tries to reach to deeper in the energy basins [22].

At low temperatures, the configuration **R** is forced to seek deeper energy basins. Only local collective rearrangements take place to move toward a little deeper energy basin. This makes the system highly heterogeneous in

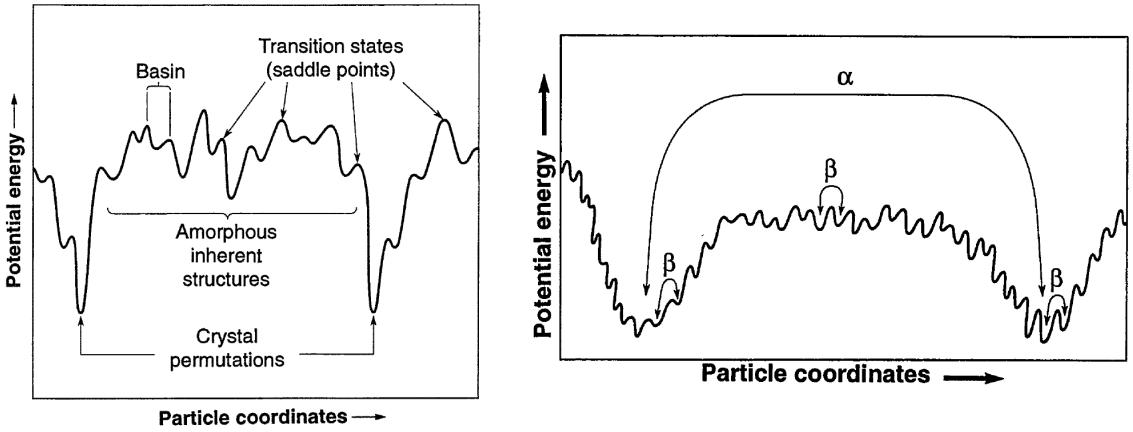

Figure 1.5: Left: Energy basin of a system of particles. Energy minimum states are known to be "inherent structures". Right: For a glassy system the β and α relaxations correspond to different sorts of exploration of inherent structure basins [21]

intermediate time scales where locally some parts of the system has higher displacements compared to the others. This is known as dynamic heterogeinity in super cooled regime. However over longer time a region with higher mobility can become the slower moving region. There are two time scales involved. β relaxations occur due to transition from neighbouring basins. Whereas, α relaxation occurs when system leaves one deeper metastable basin to reach to another, as have been expressed in the right side plot of Fig. 1.5.

1.1.3 Jamming phase diagram

Broadly a jammed state refers to a disordered phase of a material that behaves like a solid, with finite yield stress. In the context of glass transition temperature T_g, we have discussed that glass forming liquids can reach to a disordered arrested state when it is rapidly cooled. This kind of jamming thus has a "thermal" origin. However apart from rapid cooling, we can find a jammed state in other systems as a result of high density or application of shear. For example granular materials when shaken starts flowing, but becomes jammed for low shaking intensity, known as "shear jamming" [23, 24]. Colloidal systems transform to a jammed state when the density or packing fraction is increased [25, 26]. In colloidal particles the increase of relaxation time as the jammed state is approached has "entropic" origin, while shear jamming has "kinetic" origin. Liu and Najel [27] proposed the idea of an unified "jamming phase diagram" connecting these three routes to jamming, shown in Fig. 1.6. The question is weather glass transition and other mechanisms leading to an arrested amorphous state are different aspects of same "jamming" transition.

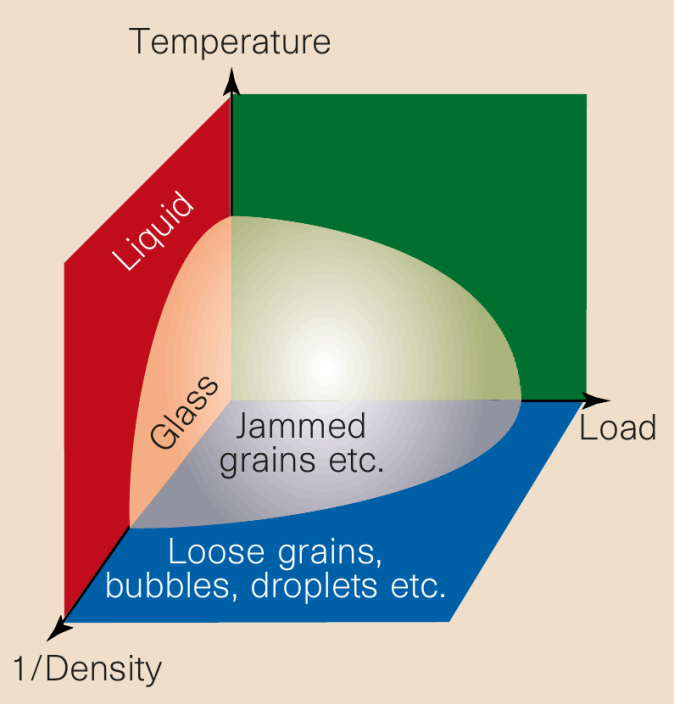

Figure 1.6: A proposed phase diagram for jamming, Three axes depend on temperature, density and load or shear stress [27].

1.1.4 Metallic glasses

Discovery of metallic glasses has been called a revolution in material science [28] due to its novel characteristics. They are very flexible and deformable like plastics.They are $4-5$ times stronger than their metallic counterparts. They have magnetic properties with less hysteresis loss and less eddy current loss making them suitable for transformer and MEMS (Micro-Electromechanical System) applications. Some examples of metal-metal metallic glasses are Ni - Nb (Nickel Niobium), Mg - Zn (Magnesium zinc), Cu - Zr (Copper Zirconium). Metallic glasses can be also formed by metals and metalloids such as, metals like Fe, Co, Ni and metalloids like B, Si, C, P. Metallic glasses have high electrical resistance and hence is used to make accurate standard resistance, computer memories and magnetic resistance sensors. They are also used in surgery in cutting tools due to high resistance to corrosion. There are many other uses of metallic glasses [29] and demands for developing basic scientific understanding of such systems. In this thesis we have chosen two model binary glass formers, the Kob-Andersen Lennard Jones (KALJ) and repulsive Wahnström (WH) model which are representatives of metallic glasses and we studied their structural changes under cyclic shear deformation (models described in Appendix).

1.2 Mechanical response of glass

Glass is an amorphous system behaving as solids: this statement makes us question how can we say if a given system's behaviour is like a solid? The answer lies in the study of its response to mechanical deformation. In this spirit, a system of bubbles, in which the surface tension is able to restore its shape when deformation is applied, is in a glassy state and "behaving" as solid. When stress is applied to deform a glassy system, it resists the deformation and this resistance against applied stress can be measured via elastic moduli, as we shall shortly discuss. Some other definitions which are important from industrial point of view are, strength: how much stress it can bear before breaking; hardness: resistance towards abrasion, for example scratch on the surface; impact resistance and chemical resistance. All these combined helps us to choose proper materials for proper use. In the rest part of this section we shall generally describe characteristics of glassy systems under uniform and periodic shear deformation.

1.2.1 Stress-strain curve

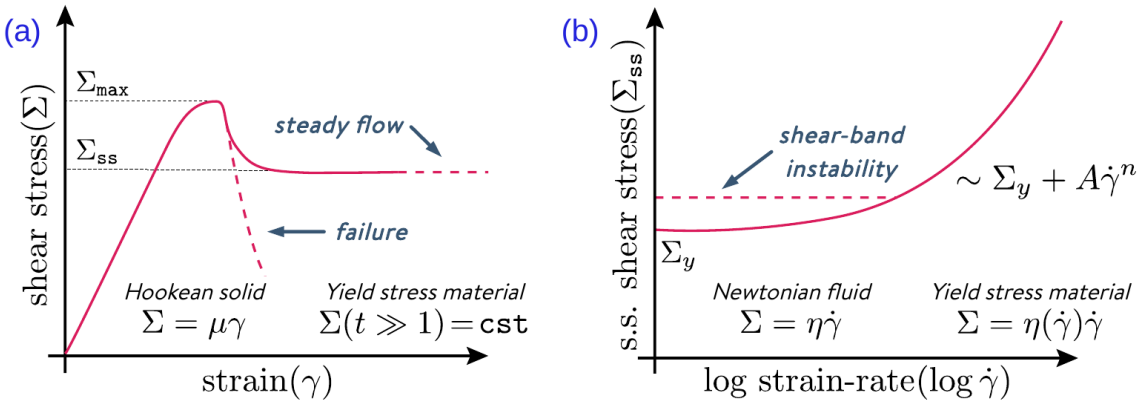

Figure 1.7: Schematic representation of response of amorphous solids to deformation. (a) Evolution of stress Σ with shear strain γ, with a stress overshoot Σ_{max}. When material fails, which generally happens before strain localization, the stress dramatically drops down. (b) Steady-state flow curve, dependence of steady state shear stress Σ_{ss} on shear rate $\dot{\gamma}$, axes are semi-logarithmic. If the flow is split into macroscopic shear bands, a stress plateau is generally observed [30].

Fig. 1.7 is a representation of the behaviour of amorphous solids under deformation [30]. Stress is defined as the applied force F per unit area A,

$$\Sigma = \frac{F}{A} \tag{1.4}$$

The strain describes the deformation in glass. In $1d$ it will be fractional change in length due to compression or stretch,

$$\gamma = \frac{\Delta L}{L}, \tag{1.5}$$

where L is the original length of the material. There are many protocols of shearing a material in the laboratory: using rheometers, applying stress in one direction, using gravity in tilted plane. We can monitor the response of a material $\Sigma(t)$ with time t as a function of imposed strain $\gamma(t)$ or strain rate $\dot{\gamma}(t)$. For a system if thermal fluctuations are negligible, it can be treated as an athermal system. Therefore in this limit of vanishing temperature the structural changes in the system is dominated by shear deformation only. As can be observed from Fig. 1.7(a), for small strains or for small applied stress the stress-strain has a linear elastic behaviour, following Hook's law,

$$\Sigma = \mu\gamma. \tag{1.6}$$

The proportionality constant μ is the elastic modulus (Young's). So in this part the deformations are reversible in nature, system can go back to its initial state when load is removed. For larger deformation, at a critical value of strain γ_y the system yields. Beyond γ_y the deformation in the system is irreversible, known as the plastic deformation. For "brittle" materials as soon as γ_y is crossed, the system fails or breaks. An example will be the window glass or silica glass. Whereas for "ductile" materials there is a flow regime beyond γ_y where particles in the system adjust their positions and results in permanent deformation in the system. Example will be metallic alloys. In steady state, the flow curve is given by Herchel-Bulkley law,

$$\Sigma = \Sigma_y + A\dot{\gamma}^n, \tag{1.7}$$

with $n > 0$, as has been shown in Fig. 1.7(b). The ductile behaviour makes the system flexible and easier to mould to any form.

The ductility highly depends on the preparation protocol of a glass [31, 32]. In simulations also different techniques can be employed to study yielding in ductile or brittle material, an example from the paper of Richard et al. [33] has been shown in Fig. 1.8. In this work $2d$ systems are sheared with strain γ in athermal limit. One of the system is bi-disperse (disks with two different radii) interacting through Lennard Jones (LJ) potential, other one is a poly-disperse (POLY) packing with purely repulsive interactions. The LJ system has been quenched using three protocols, namely instantaneous quenches from high temperature liquid (HTL), equilibrated supercooled liquid states (ESL) and gradual quench (GQ) where the system is gradually quenched from high to low temperature. For polydisperse, the glass is first equilibrated at a certain temperature T_{ini} and then instantaneously quenched to $T = 0$ by energy minimization. We find from Fig. 1.8 that for POLY , at lowest temperature theere is abrubt stress drop in the stress-strain curve, after which system goes to the steady flow state. So, the structure at the lower temperatures

are more brittle compared to higher temperatures. Whereas, for LJ system we mainly find ductile bevaviour where the transition from elastic to flow state is smooth. Although for GQ protocol the system is less ductile. The systems we have used in the thesis, KALJ and WH are ductile in nature.

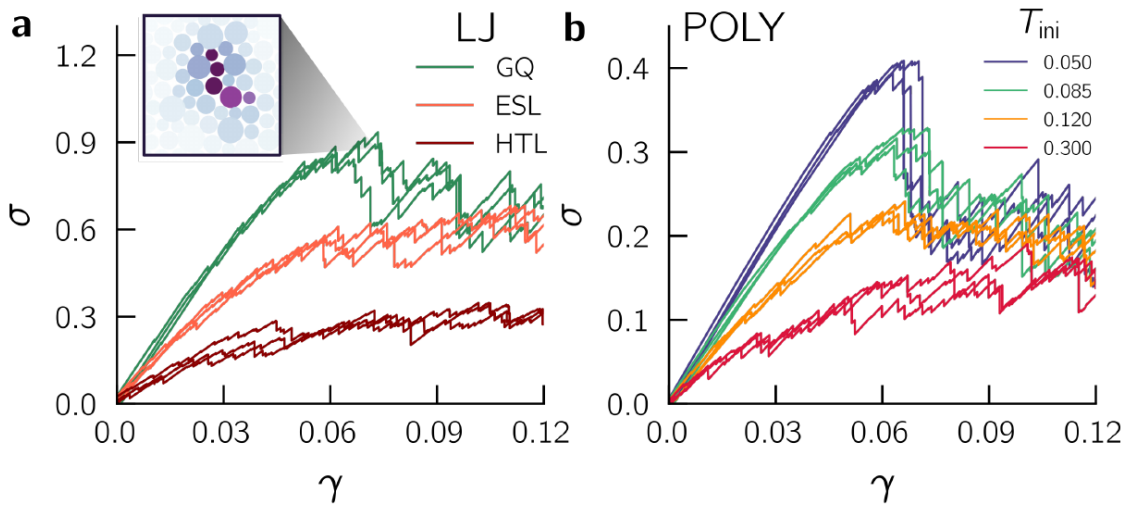

Figure 1.8: Stress strain curve for (a) Lennard Jones system with different quench protocols, inset shows a set of particles with plastic rearrangements; and (b) Polydispere systems quenched from different initial temperatures T_{ini} [33].

What is the mechanism of plastic flow? A very nice review in the context of metallic glass is given by Hufnaget et al [34]. As the system is sheared, particles undergo local rearrangements. Time scales associated with the driven systems are much shorter than aging time scales. Therefore, some thermal systems can be treated as athermal [30]. At low temperatures or in athermal limit the system is residing close to its energy minimum configurations, the inherent structures. Deformation of the system essentially deforms the potential energy landscape. Because of shear deformation a local energy minimum can slowly disappear and the system becomes mechanically unstable and therefore forced to move towards a new alternative minimum. Very small number of particles take part in search of new minima by locally rearranging themselves. These are known as plastic events and a zone where rearrangements happen is known as shear-transformation zone (STZ). Is it possible to identify STZ in a given system? In chapter 4, we have shortly discussed about STZ in the introduction.

1.2.2 Shear banding

Under shear deformation amorphous metallic glasses show a very complex local rearrangements of particles. At small strains these rearrangements are reversible. At large stresses the rearrangements are dissipative involving mechanical instabilities. A very interesting effect observed in shearing is the strain localization in the system, also

known as shear-banding [35, 36]. In Fig. 1.9 two instances of shear band formation in the steady flow state, one obtained from simulation (A) and the other from experiment (B) are presented.

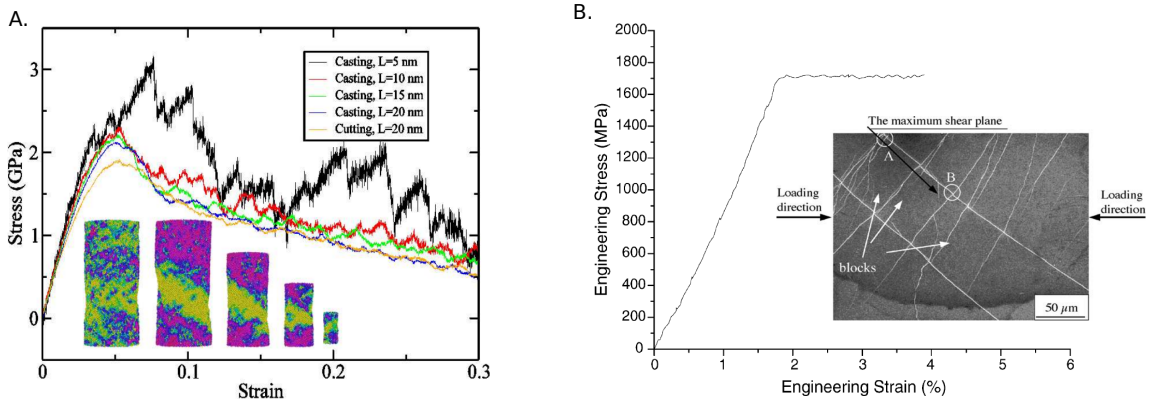

Figure 1.9: A. Stress strain curve obtained from the simulation data of nano-wires with different casting lengths. The insets correspond to samples at 10% strain rates, where the atoms have been coloured from red (0% shear strain) to yellow (20% larger shear strain)according to shear strain. We can clearly see localization of shear strain [37]. B. Stress-strain curve obtain from experiments on bulk metallic glass $Zr_{41.2}Ti_{13.8}Cu_{12.5}Ni_{10}Be_{22.5}$ by situ scanning electron microscopy (SEM) quasi-static uniaxial compression experiments at room temperature. Inset shows typical deformation patterns of multiple intersecting and branched shear bands [38].

Review on shear bands in metallic glasses can be found in [39]. One perception is homogeneous nucleation. It is thought that STZ is activated throughout the system and at some point during the deformation a percolation threshold is reached and they link-up to form a shear band. A second take on shear band formation is that a stress concentration originates in some place of the system and then a mature shear front propagates through the system forming the band [40]. However this second model is more appropriate for high-rate loading. Shrivastav et al. [41] for Lennard Jones glass unveiled that due to finite shear rate inhomogeneous flow regimes form in the system. At lower strain rate percolating cluster of mobile regions evolves to a long-lived shear band. In general, the large shear strain values in the shear band indicates that the structure inside and outside the band is different. For metallic glasses there can be single shear band with intense shear [42], or multiple bands with minimal shear [38] or homogeneous distribution depending on the material [43], conditions and protocols. The local energy [1] and local density of the shear band is different from the unsheared system [44]. In Fig. 1.10 we show the direct measurement of this density variation of shear band in a metallic glass [44].

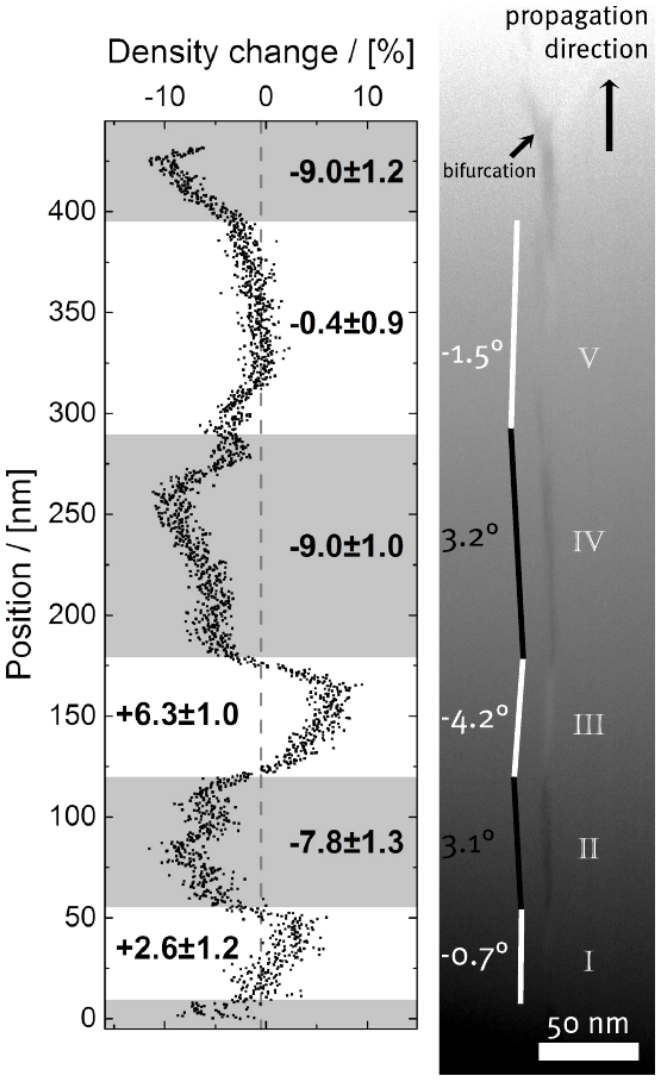

Figure 1.10: The image of shear band found in cold-rolled $Al_{88}Y_7Fe_5$ propagating from bottom to top is shown in the right. Corresponding density variation with respect to undeformed state is shown in right [44].

1.2.3 Cyclic shear

Cyclic shear deformation is a well known technique in testing the rheology of a material and even to improve it. By cyclic shear we mean that the strain $\gamma(t)$ on the system is varied cyclically, with some amplitude γ_{max}. In Lennard-Jones type ductile material it is difficult to identify yielding strain γ_y from the almost continuous stress-strain curve (Fig. 1.8). When a system is periodically driven for many cycles, a steady energy state is reached. In steady energy states of cyclic shear, the yielding transition is sharper compared to the unidirectional shear [45, 46, 47]. This becomes clear when steady state values of stress σ_{max} is plotted against amplitude γ_{max}, as was reported by Leishangthem et al [48] (Fig. 1.11).

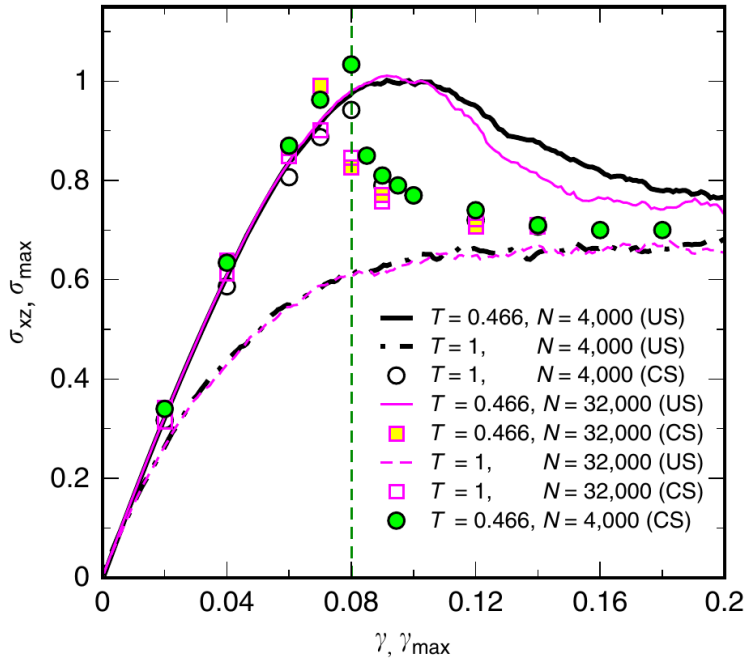

Figure 1.11: Stress strain curve for Kob Andersen Lennard Jones system under uniform shear (US) and cyclic shear (CS) corresponding to two initial temperatures T and different system sizes N. Yielding strain value is shown by broken vertical green curve [48]

Fiocco et al. [49] reported that under oscillatory shear deformation the Kob-andersen Lennard Jones glass reaches a steady energy state after a short transient. Fig. 1.12 shows the evolution of energy and mean square displacements at the end of each cycle of deformation for various γ_{max} values, across the critical yielding amplitude γ_y.

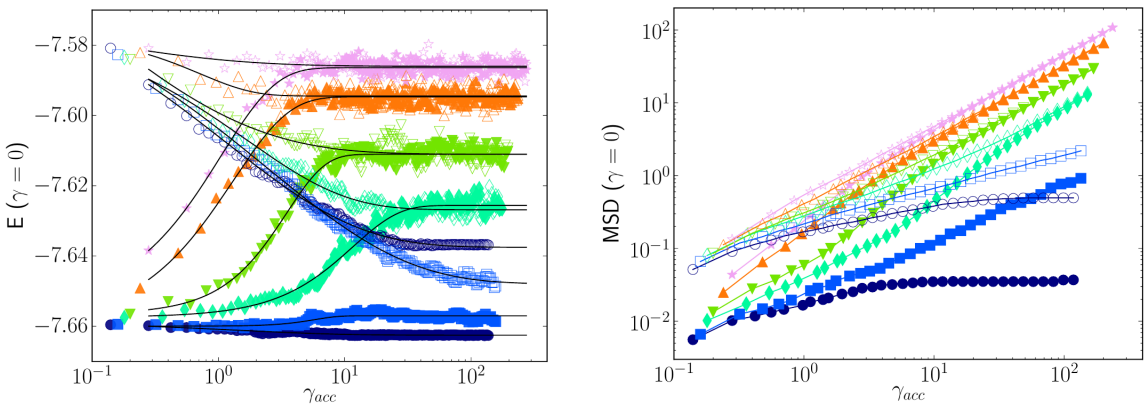

Figure 1.12: Left: Energy of the KALJ system is plotted against accumulated strain at the end of each cycle of deformation. Filled symbols are for a system initially prepared at low temperature $T_{ini} = 0.466$ and open symbols are for $T_{ini} = 1.0$. Different sysbols correspond to different values of strain amplitudes γ_{max}: 0.07 (circle), 0.08 (square), 0.09 (diamond), 0.1 (down triangle), 0.12 (up triangle) and 0.14 (star). Above yielding amplitude $\gamma_y \approx 0.07$ energy levels for two T_{ini} merge. Right: Mean square displacements of the particles at the end of each cycle with reference to the initial configuration. In steady state there is a transition from absorbing to diffusive state at γ_y [49].

There is a clear non-equilibrium transition from absorbing state to diffusive state at γ_y. In absorbing state the system has reached to a configuration where particles during the deformation cycle moves reversibly, so from one cycle to the next, the net displacement is zero, hence the MSD becomes a constant. On the other hand, above yielding, we have a diffusive state, growing mean square displacements. In the later case the particle arrangements are irreversible.

We notice from the energy plot that before reaching to the steady state in the transient, the energy of the high temperature glass decreases. High temperature glass and hence high energetic glass going to deeper energy minimum states as a result of shear is known as the mechanical annealing [50, 51]. However, for low temperature glass we clearly observe the gain in the energy in the diffusive states (Fig. 1.12). This is known as energy rejuvenation in glass [52, 53]. This high energy in this system is associated with the formation of shear band in the system. Parmar et al. [1] have done a detailed thermodynamic analysis of single the shear band found in KALJ system of size $N = 64000$ for amplitudes γ_{max} above yielding. Above yielding the local energy inside strain localized shear band is much higher compared to the part of the system outside shear band, as we find in Fig. 1.13. Once shear band is formed, particles inside shear band move chaotically from one cycle to the next, giving rise to the mean square displacements. Outside shear band the displacements are minimal.

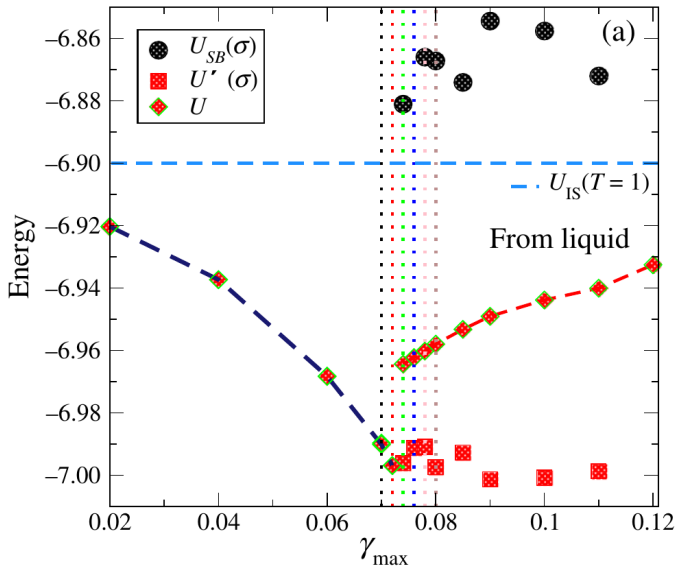

Figure 1.13: Steady state energy of KALJ system initially prepared at high temperature $T = 1$ and density $\rho = 1.2$ as a function of strain amplitude γ_{max}. Below yielding, ($\gamma_y \approx 0.07$) steady state energy U decreases, and above yielding jumps to higher value. But a deeper analysis inside and outside of shear band shows that energy inside shear band $U_{SB}(\sigma)$ is much higher than the overall energy of the system. But, far from shear band, $U'_{SB}(\sigma)$ the enrgy remains at the same low level of γ_y [1].

The absorbing and disspitative nature of the system below and above yielding can be realised by plotting the

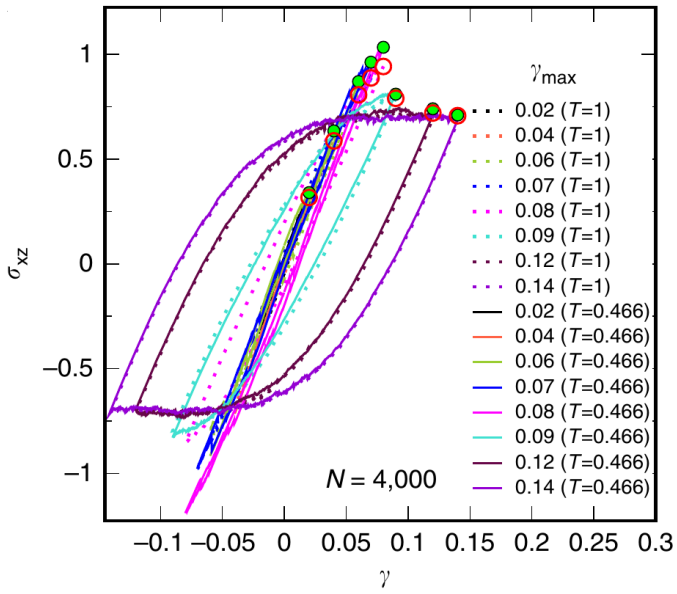

Figure 1.14: KALJ system at density $\rho = 1.2$ under periodic deformation in athermal limit: stress-strain curve in the steady states of cyclic shear fir various strain amplitudes below and above yielding amplitude $\gamma_y \approx 0.07$. For both the temperatures T, we fins above yielding the hysteresis curves have larger area. Maximum value of stresses has been showed in circular symbols [48].

stress-strain curve of the system during a deformation cycle in steady state as in Fig. 1.14 [48]. Area under the curve is proportional to the work done by the system. Below yielding the curves are really narrow, in contrast to above yielding the area suddenly increases. This is because, in the steady states below yielding only a handful of particles locally rearrange. But above yielding particles have higher displacements and dissipate energy. It is worth mentioning that that shear band of high strain localization found above yielding has higher energy because it is a band of particles with large irreversible plastic flow.

In this thesis

Yielding in glasses has been identified as a dynamical phase transition. One open question remains if the system undergoes critical structural changes across yielding. In this thesis we have addressed this question by examining structural changes in model glass system under cyclic shear deformation. This has been done from two directions. Firstly, in the KALJ system we investigate "Hyperuniformity" across yielding and in the shear banded system. The concept of hyperuniformity is related to the long range direct correlations and density fluctuations in the system. We dedicate a complete chapter Introduction II, where we discuss about hyperuniformity. Then in Chapter 3 we discuss the results for KALJ system. Secondly, we investigate the connection between local structures and plastic rearrangements in the steady states of cyclic shear deformation in WH system in Chapter 4. We analyze the changes in mean local ordering in the system across yielding and extract the nature of local clusters inside and outside of shear band. In chapter 5 we have concluded our results from both the chapters. Appendix contains

details of numerical simulation of our model glass forming systems. At the end of the thesis we have short abstracts in both English and French.

Chapter 2

Introduction II: About Hyperuniformity

2.1 Basic concepts

Nature of statistical fluctuations are crucial in understanding and characterising a wide range of systems at equilibrium and as well as out of equilibrium. Can we characterise how a set of points are distributed in space? "Hyperuniformity" emerges as an answer to this question. It is a special property which describes suppression of number density fluctuations at large length scales. A great review on hyperuniform states of matter was published by Salvator Torquato, one of the pioneering researchers who explored hyperuniformity in various contexts, in 2018 [2]. This review is the main inspiration for this chapter. In a many particle-system in d dimensions, if we sample different parts of the system or different realizations of the system with a spherical window of size R, the number of points inside the window shall have fluctuations. With growing window sizes, if the number variance,

$$\sigma_N^2(R) = < N(R)^2 > - < N(R) >^2, \tag{2.1}$$

scales slower than the volume $\sim R^d$, that implies fluctuations are suppressed in large length scales and the system is hyperuniform. Equivalently, One can express in terms of number density variance, by dividing the number of points inside a window with volume of the window,

$$\Delta^2(R) = < \rho(R)^2 > - < \rho(R) >^2, \tag{2.2}$$

and for hyperuniformity $\Delta^2(R)$ decays faster than R^{-d} in large R limit.

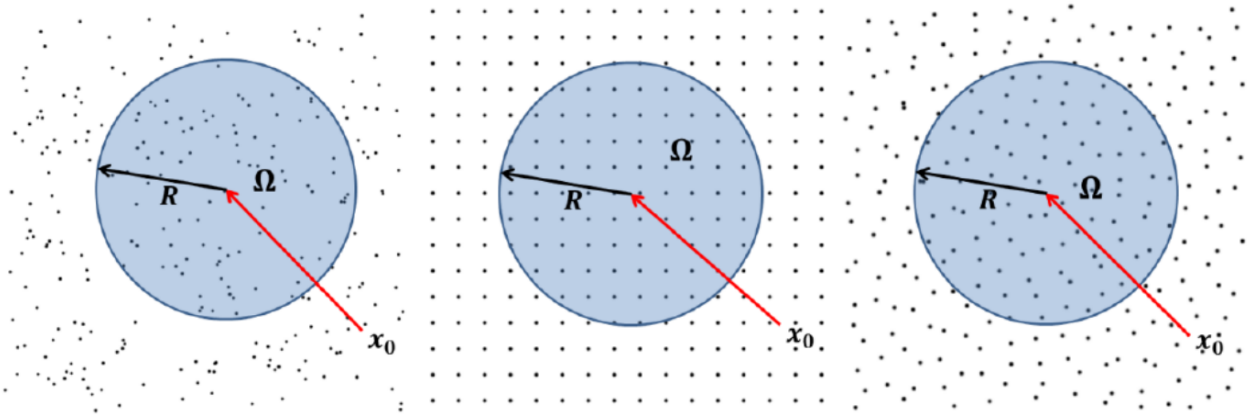

Figure 2.1: Schematic representation of sampling window Ω of radius R in three types of systems, from left to right : randomly disordered system, ordered system and hyperuniform system. x_0 is the center of the window [2].

Fig. 2.1 illustrates three types of point distributions. On the left we have random Poisson type point distribution. In this case the number variance grows with window volume, $\sigma_N^2(R) \sim R^d$. In the middle we have an ordered arrangement. Note that here fluctuations will arise only due to the surface of the window and hence we shall have, $\sigma_N^2(R) \sim R^{d-1}$. This is an example of ordered hyperuniform system. At the right we have the most interesting case. It is an example of disordered hyperuniformity, the scaling of $\sigma_N^2(R)$ is slower than R^d, but not as slow as R^{d-1}. This intermediate occurrence of fluctuation-suppression manifests a new exotic state of matters. All perfect crystals, perfect quasi-crystals are hyperuniform and so is special disordered systems. Therefore it provides a unified framework to characterize structures of these materials and also to differentiate systems on the degree of hyperuniformity. At large length scales disordered hyperuniform systems are able to suppress fluctuations like a crystal and in smaller length scales it behaves as a liquid or glass where it is completely isotropic. This accounts for novel applications as we shall touch upon. Also, a consequence of decaying number density variance at large length-scales is that, in long-wavelength limit, i.e. as wave vector $\mathbf{k} \to 0$, the structure factor,

$$S(\mathbf{k} \to 0) \to 0, \tag{2.3}$$

following density-fluctuation theorem. Now, structure factor is proportional to the scattering intensity from the material. Fig. 2.2 shows the scattering pattern from an ordered crystal and disordered "stealthy" hyperuniform system [54, 55]. In the later, we observe that there is a range of wave vectors surrounding the origin where there is no scattering.

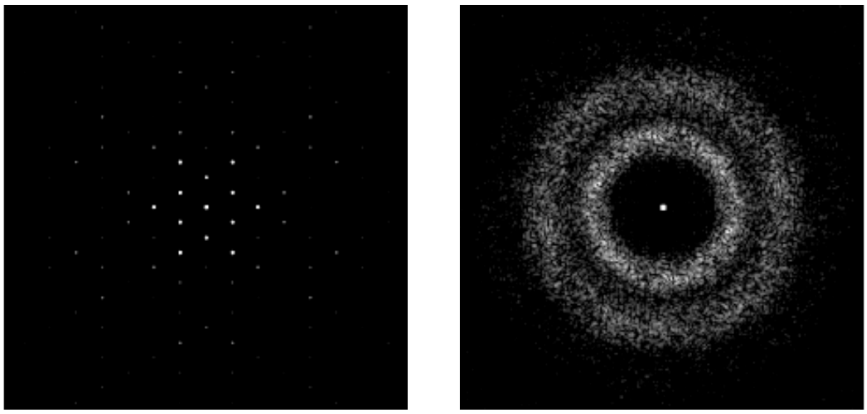

Figure 2.2: Scattering from two very distinct hyperuniform systems. Left: A six-fold symmetric crystal and Right: A disordered "stealthy" hyperuniform system [2].

Hyperuniformity has been only explored in last two decades. One of its earliest appearance was in cosmological models [56] where hyperuniformity was termed as "super-homogeneous" distribution connecting the properties of Arrison-Zeldovich like spectra and this revelation was called to be "glass like universe". At present there are plenty of instances where hyperuniformity has been found, both in equilibrium and non-equilibrium systaems. Examples include maximally random jammed (MRJ) hard-particle packings [57, 58, 59, 60, 61], granular media [62, 63], colloidal packing [64, 65], emulsions [66], avian photoreceptors [60], quantum ground states [67], classical disordered ground states [54, 68, 69, 70], eigen values of random matrices [71, 72], non-equilibrium phase transitions [73, 74, 75, 76, 77, 78].

2.2 Mathematical formulations: Point processes

In the following subsections we shall discuss the relationship between isothermal compressibility and number variance, we shall define radial distribution function $g(r)$, structure factor $S(k)$ and we shall show in vanishing wave vector limit the relationship between $S(k)$ and number variance. Thereafter we shall consider spherical windows sampling a point process and discuss how in large window size limit number variance inside the window relates to $S(k)$.

2.2.1 Number variance and compressibility χ_T

In grand canonical ensemble where both exchange of particles and exchange of energy are possible, the grand potential is defined as,

$$\Omega = F - N\mu. \tag{2.4}$$

Here F is the Helmholtz Free energy $F = U - TS$ and μ is the chemical potential. U is internal energy, T is the temperature and S is the entropy. The probability density in this grand canonical ensemble is given by,

$$f_0(r^N, p^N, N) = \frac{exp[-\beta(H - N\mu)]}{\Xi}. \tag{2.5}$$

Here $\beta = \frac{1}{K_B T}$, H is the Hamiltonian, and Ξ is the grand canonical partition function given by,

$$\Xi = \sum_{N=0}^{\infty} \frac{exp(N\beta\mu)}{h^{3N} N!} \int\int exp(-\beta H) dr^N dp^N \tag{2.6}$$

$$= \sum_{N=0}^{\infty} \frac{z^N}{N!} Z_N, \tag{2.7}$$

where for a system of N particles $dr^N dp^N \equiv dr_1 dr_2 ... dr_N dp_1 dp_2 ... dp_N$, $z = \frac{exp(\beta\mu)}{\Lambda^3}$, $\Lambda = (\frac{2\pi\beta\hbar^2}{m})^{1/2}$ and $Z_n = \int dr_1 dr_2 ... dr_N$. The probability $p(N)$ that the ensemble contains N particles is,

$$p(N) = \frac{1}{h^{3N} N!} \int\int f_0 dr^N dp^N = \frac{1}{\Xi} \frac{z^N}{N!} Z_N. \tag{2.8}$$

Therefore average number of particles will be given by,

$$< N >= \sum_{N=0}^{\infty} N p(N) = \frac{1}{\Xi} \sum_{N=0}^{\infty} N \frac{z^N}{N!} Z_N = \frac{\partial ln\Xi}{\partial lnz}. \tag{2.9}$$

Differentiating by lnz we obtain,

$$\frac{\partial < N >}{\partial lnz} = z \frac{\partial}{\partial z} (\frac{1}{\Xi} \sum_{N=0}^{\infty} N \frac{z^N}{N!} Z_N) \tag{2.10}$$

$$= \frac{1}{\Xi} \sum_{N=0}^{\infty} N^2 \frac{z^N}{N!} Z_N - (\frac{1}{\Xi} \sum_{N=0}^{\infty} N \frac{z^N}{N!} Z_N)^2 \tag{2.11}$$

$$=< N^2 > - < N >^2 =< (\Delta N)^2 > . \tag{2.12}$$

Now, the isothermal compressibility is defined as,

$$\chi_T = -\frac{1}{V} (\frac{\partial V}{\partial P})_T. \tag{2.13}$$

To establish the relation between isothermal compressibility and number fluctuation, we note, Helmholtz free energy is an extensive property, that is dependent on system size. So, one can write,

$$F = N\phi(\rho, T). \tag{2.14}$$

Where ϕ is free energy per particle. Since $\mu = (\frac{\partial F}{\partial N})_{T,V}$, we get,

$$\mu = \phi + N\frac{\partial \phi}{\partial \rho}\frac{\partial \rho}{\partial N} \tag{2.15}$$

$$= \phi + \rho\frac{\partial \phi}{\partial \rho}. \tag{2.16}$$

Therefore,

$$(\frac{\partial \mu}{\partial \rho})_T = 2(\frac{\partial \phi}{\partial \rho})_T + \rho(\frac{\partial^2 \phi}{\partial \rho^2}). \tag{2.17}$$

We know from thermodynamics, pressure $P = -(\frac{\partial F}{\partial V})_{T,N}$. Since, $\rho = \frac{N}{V}$, $\frac{\partial}{\partial V} = -\frac{\rho^2}{N}\frac{\partial}{\partial \rho}$ and it gives,

$$P = \rho^2(\frac{\partial \phi}{\partial \rho})_T. \tag{2.18}$$

Differentiating w.r.t. ρ at constant temperature,

$$(\frac{\partial P}{\partial \rho})_T = 2\rho(\frac{\partial \phi}{\partial \rho})_T + \rho^2(\frac{\partial^2 \phi}{\partial \rho^2})_T = \rho(\frac{\partial \mu}{\partial \rho})_T. \tag{2.19}$$

Again, $(\frac{\partial P}{\partial \rho})_T = \frac{\partial P}{\partial V}\frac{\partial V}{\partial \rho} = -\frac{V^2}{N}\frac{\partial \rho}{\partial V}$. So from the definition of isothermal compressibility $(\frac{\partial P}{\partial \rho})_T = \frac{1}{\rho \chi_T}$.
As, $(\frac{\partial \mu}{\partial \rho})_T = (\frac{\partial \mu}{\partial N})(\frac{\partial N}{\partial \rho}) = V(\frac{\partial \mu}{\partial N})$, we have $\rho\frac{\partial \mu}{\partial \rho} = \frac{1}{\rho \chi_T}$.
We already had, $\frac{<(\Delta N)^2>}{<N>} = \frac{K_B T}{<N>}\frac{\partial <N>}{\partial \mu}$. Therefore it simply follows,

$$\frac{<(\Delta N)^2>}{<N>} = \rho K_B T \chi_T. \tag{2.20}$$

From Equation 2.20 we find that in thermodynamic equilibrium compressibility χ_T of the system is related to the variations in number fluctuations in grand canonical ensemble.

2.2.2 Radial distribution function $g(r)$

For a point-process "n-particle density" $\rho_N^{(n)}$ can be defined as,

$$\rho_N^{(n)}(r^n) = \frac{N!}{(N-n)!}\frac{1}{Z_N}\int exp(-\beta V_N) dr^{(N-n)}. \tag{2.21}$$

Basically, $\rho_N^{(n)}(r^n)dr^N$ is the probability of finding n particles within the volume element dr^N, irrespective of the coordinates of rest of the particles and irrespective of their momenta. Therefore it would hold that,

$$\int \rho_N^{(n)} dr^n = \frac{N!}{(N-n)!}. \tag{2.22}$$

For instance the single particle density,

$\int \rho_N^{(1)} dr^1 = N$, for uniform field, this gives, $\rho_N^{(1)} = \rho = \frac{N}{V}$.

Now the n-particle distribution function $g_N^{(n)}(r^n)$ is defined as,

$$g_N^{(n)}(r^n) = \frac{\rho_N^{(n)}(r_1 ... r_n)}{\prod_{i=1}^{n} \rho_N^{(1)}(r_i)}. \tag{2.23}$$

For homogeneous systems,

$$\rho^n g_N^{(n)}(r^n) = \rho_N^{(n)}(r^n). \tag{2.24}$$

Now let us write these in terms of delta functions. Let us find the average of $\delta(r - r_1)$.

$$\begin{aligned} < \delta(r-r_1) > &= \frac{1}{Z_N} \int \delta(r-r_1) exp[-\beta V_N(r_1, r_2.., r_N)] dr^N \\ &= \frac{1}{Z_N} \int ... \int exp[-\beta V_N(r, r_2.., r_N)] dr_2 ... dr_N. \end{aligned}$$

Comparing with the definition of n-particle distribution function, we can see,

$$\rho_N^{(1)}(r) = < \sum_{i=1}^{N} \delta(r - r_i) > .$$

Similarly, it will follow,

$$\rho_N^{(2)}(r) = < \sum_{i=1}^{N} \sum_{j=1}^{N} \delta(r - r_i) \delta(r - r_j) > .$$

Now we can write,

$$\begin{aligned} < \frac{1}{N} \sum_{i=1}^{N} \sum_{j=1}^{N} \delta(r - r_j + r_i) > &= < \frac{1}{N} \sum_{i=1}^{N} \sum_{j=1}^{N} \delta(r' + r - r_j) \delta(r' - r_i) > \\ &= \frac{1}{N} \int \rho_N^{(2)}(r' + r, r'). \end{aligned}$$

So, for homogeneous and isotropic system,

$$< \frac{1}{N} \sum_{i=1}^{N} \sum_{j=1}^{N} \delta(r - r_j + r_i) > = \frac{\rho^2}{N} \int g_N^{(2)}(r, r') dr' = \rho g(r). \tag{2.25}$$

The definition of $g(r)$ implies on the average the number of particles lying within the range of r to $r + dr$ from a reference particle is $4\pi r^2 \rho g(r) dr$, peaks in the plot of $g(r)$ versus r represent "shells" of neighbours around the reference particle.

2.2.3 Ornstein–Zernike Equation

The radial distribution function $g^{(n)}(r^N) \to 1$ for large mutual separations. Therefore total pair correlation function for a statistically homogeneous and isotropic system is defined as,

$$h(r) = g(r) - 1. \tag{2.26}$$

$h(r)$ measures the influence of a particle at position $\mathbf{r}_2$ on a particle at position $\mathbf{r}_1$, separated by the distance $r = |\mathbf{r}_2 - \mathbf{r}_1|$. Ornstein and Zernike proposed that this total correlation function can be decomposed into a "direct" and "indirect" part.

$$h(r) = c(r) + \rho \int c(|r - r'|)h(r')dr'. \tag{2.27}$$

The interpretation is, the total correlation $h(1,2)$ between the particles 1 and 2 is due to their direct correlation $c(1,2)$ plus indirect correlation via other particles. Taking Fourier transform (F.T.),

$$\hat{h}(k) = \hat{c}(k) + \rho \int \int c(|r - r'|)h(r')dr' \exp(-ikr)dr.$$

Writing $\exp(-ikr)$ as $exp(-ik(r-r'))\exp(-ikr')$ from the properties of F.T. we can obtain,

$$\begin{aligned} \hat{h}(k) &= \hat{c}(k) + \rho\hat{c}(k)\hat{h}(k) \\ &= \frac{\hat{c}(k)}{1 - \rho\hat{c}(k)}. \end{aligned}$$

2.2.4 Structure factor and zero wave-vector limit

Structure factor is defined from the density density correlation in k-space,

$$S(\vec{k}) = \frac{1}{N} < \tilde{\rho}(\vec{k})\tilde{\rho}(-\vec{k}) > \tag{2.28}$$

$$= \frac{1}{N}\Big\langle \sum_{i=1}^{N}\sum_{j=1}^{N} \exp(i\vec{k}\cdot\vec{r}_i)\exp(-i\vec{k}\cdot\vec{r}_j)\Big\rangle. \tag{2.29}$$

Further expanding,

$$\begin{aligned} S(\vec{k}) &= 1 + \frac{1}{N}\Big\langle \int\int \exp\left(-i\vec{k}\cdot(\vec{r}-\vec{r}')\right)\sum_{i=1}^{N}\sum_{j=1,i\neq j}^{N}\delta(\vec{r}-\vec{r}_i)\delta(\vec{r}'-\vec{r}_j)d\vec{r}d\vec{r}'\Big\rangle \\ &= 1 + \frac{1}{N}\int\int \exp\left(-i\vec{k}\cdot(\vec{r}-\vec{r}')\right)\rho(\vec{r},\vec{r}')d\vec{r}d\vec{r}' \\ &= 1 + \frac{\rho^2}{N}\int\int \exp\left(-i\vec{k}\cdot(\vec{r}-\vec{r}')\right)g(\vec{r},\vec{r}')d\vec{r}d\vec{r}'. \end{aligned}$$

For statistically homogeneous systems, $g(\vec{r},\vec{r}')$ only depends on the radial distance $r = |\vec{r}-\vec{r}'|$,

$$S(\vec{k}) = 1 + \rho \int \exp(-i\vec{k}\cdot\vec{r}) g(r) d\vec{r}. \tag{2.30}$$

We have defined total correlation function $h(r) = g(r) - 1$, in terms of F.T. of total correlation function $\tilde{h}(\vec{k})$,

$$S(\vec{k}) = 1 + \rho\tilde{h}(\vec{k}) = \frac{1}{1-\rho\tilde{c}(\vec{k})}. \tag{2.31}$$

Form compressibility equation we know, $\rho K_B T \chi_T = 1 + \rho \int [g(r) - 1] dr$.

Since $\hat{h}(k) = \int h(r) exp(-ikr) dr$, so, $\hat{h}(0) = \int h(r) dr$.

Therefore, we can see,

$$\rho K_B T \chi_T = 1 + \rho\hat{h}(0) = S(0). \tag{2.32}$$

Therefore, in zero wave vector limit, structure factor is related to compressibility.

Structure factor, number variance and compressibility at zero wave-vector limit

Combining Eq. 2.20 and Eq. 2.32, we can see that in an equilibrium grand canonical system,

$$\frac{<(\Delta N)^2>}{<N>} = \rho K_B T \chi_T = S(0) \tag{2.33}$$

This equation holds the relationship between the two main observables in the study of hyperuniformity where in k-space we are interested in low-wavector limit of structure factor and we study the number variance with growing length scales.

However, the relationship with compressiblity, $S(0) = \rho K_B T \chi_T$ only holds for equilibrium systems. But irrespective of a system in equilibrium or not we can extablish the relationship $S(0) = \frac{<(\Delta N)^2>}{<N>}$ for infinitely large windows, as we shall see in the next sub-section.

Structure factor and number variance in the limit of large window size

Number variance as a function of window size

Coming to real space fluctuations, when observation windows Ω of size **R** (vector for non-spherical windows, depend on the parameters) is placed in the system with the center of the window at $\mathbf{x}_0$ and then $\mathbf{x}_0$ is varied to sample different parts of the system, we can compute number variance. Introducing window indicator function w to count

particles inside a certain window,

$$w(\mathbf{x}-\mathbf{x}_0;\mathbf{R}) = \begin{cases} 1 & ,\mathbf{x}-\mathbf{x}_0 \in \Omega \\ 0 & ,\mathbf{x}-\mathbf{x}_0 \notin \Omega. \end{cases} \tag{2.34}$$

The number of points inside the window is then,

$$N(\mathbf{x}_0,\mathbf{R}) = \sum_{i=1} w(\mathbf{r}_i-\mathbf{x}_0;\mathbf{R}). \tag{2.35}$$

In thermodynamic limit if ρ is the global density and $v_1(\mathbf{R})$ is the volume of the window, on the average number of particles inside a window of size **R** will be,

$$< N(\mathbf{R}) >= \rho v_1(\mathbf{R}) = \rho \int_{\mathbb{R}^d} w(\mathbf{r};\mathbf{R}) d\mathbf{r}, \tag{2.36}$$

We can express number density variance as a function of window size,

$$\begin{aligned} \sigma_N^2(\mathbf{R}) =& < N^2(\mathbf{R}) > - < N(\mathbf{R}) >^2 \\ =& \int_{\mathbb{R}^d} \rho_1(\mathbf{r}) w(\mathbf{r}_1-\mathbf{x}_0;\mathbf{R}) d\mathbf{r}_1 + \int_{\mathbb{R}^d}\int_{\mathbb{R}^d} \left[\rho_2(\mathbf{r}_1,\mathbf{r}_2) - \rho_1(\mathbf{r}_1)\rho_1(\mathbf{r}_2)\right] w(\mathbf{r}_i-\mathbf{x}_0;\mathbf{R}) d\mathbf{r}_1 d\mathbf{r}_2 \\ =& < N(\mathbf{R}) > \left[1+\rho \int h(\mathbf{r})\alpha_2(\mathbf{r};\mathbf{R}) d\mathbf{r}\right], \end{aligned}$$

where, $\alpha_2(\mathbf{r};\mathbf{R})$ is given by

$$\alpha_2(\mathbf{r};\mathbf{R}) = \frac{v_2^{int}(\mathbf{r},\mathbf{R})}{v_1(\mathbf{R})}. \tag{2.37}$$

Here v_2^{int} is the *scaled intersection volume* function for two windows seperated by a distance **r**,

$$v_2^{int}(\mathbf{r},\mathbf{R}) = \int w(\mathbf{x}_0;\mathbf{R}) w(\mathbf{x}_0+\mathbf{r};\mathbf{R}) d\mathbf{x}_0. \tag{2.38}$$

For example in case of two spherical windows overlapping v_2^{int} will be the common volume of the lens formed by them. By construction, for $\mathbf{r}=0$, $\alpha_2=1$ and it is non zero only when there is an overlap.

Using Parsaval's theorem of Fourier transform, number variance equation can be re-written in terms of structure factor $S(\mathbf{k})$,

$$\sigma_N^2(\mathbf{R}) =< N(\mathbf{R}) > \left[\frac{1}{(2\pi)^d} \int_{\mathbb{R}^d} S(\mathbf{k}) \tilde{\alpha}_2(\mathbf{k};\mathbf{R}) d\mathbf{k},\right]$$

where $\tilde{\alpha}_2(\mathbf{k};\mathbf{R})$ is the F.T. of $\alpha_2(\mathbf{r};\mathbf{R})$.

In infinite wavelength limit

In large length scale limit, the size of the window grows and we have, $v_1(\mathbf{R}) \to \infty$, the Fourier transform of scaled intersection volume $\tilde{\alpha}_2(\mathbf{k};\mathbf{R}) \to (2\pi)^d \delta(\mathbf{k})$, where $\delta(\mathbf{k})$ is the d dimensional Dirac delta function. In this limit, the variance has the following form,

$$\lim_{v_1(\mathbf{R})\to\infty} \frac{\sigma_N^2(\mathbf{R})}{< N(\mathbf{R}) >} = \lim_{\mathbf{k}\to 0} S(\mathbf{k}) = 1 + \rho \int h(\mathbf{r}) d\mathbf{r}. \tag{2.39}$$

Since for hyperuniform system, $\lim_{\mathbf{k}\to 0} S(\mathbf{k}) = 0$, we get,

$$\lim_{v_1(\mathbf{R})\to\infty} \frac{\sigma_N^2(\mathbf{R})}{< N(\mathbf{R}) >} = 0. \tag{2.40}$$

As promised, Eq. 2.39 gives us the relation between structure factor and number density variance in the infinite wavelength limit, which holds true for both equilibrium and non-equilibrium systems.

2.3 Classification of hyperuniform systems

For a monodisperse point configuration, hyperuniformity is linked to vanishing structure factor. In the vicinity of origin, a power-law form of structure factor is found for hyperuniform systems [79],

$$S(|\mathbf{k}|) \sim |\mathbf{k}|^{\alpha} \tag{2.41}$$

with a positive exponent $\alpha > 0$. Mathematical analysis presents three classifications of hyperuniform systems depending on α.

Classes	α	$\sigma_N^2(R)$
Class I	$\alpha > 1$	$\sim R^{d-1}$
Class II	$\alpha = 1$	$\sim R^{d-1} \ln R$
Class III	$0 < \alpha < 1$	$\sim R^{d-\alpha}$

Few examples of the above classes are,

Class I:

All crystals [56], many quasi-crystals [80], stealthy hyperuniform ground states [54, 55], one-component plasmas [81], perfect glasses [82], purturbed lattices [83, 84].

Class II:

Maximally random jammed packings [57, 59], density fluctuations in early universe [85], some quasi-crystals [80], fermionic point process [67], superfluid helium, some purturbed lattices,perfect glasses [82].

Class III:

Classical disordered ground states [86], random organization models, perfect glasses [82], perturbed lattices[87]

2.4 Size disperse systems

2.4.1 Volume fraction variance and spectral density

Generalized hyperuniormity can be applied to systems beyond point distributions. Examples include two-phase media, polydisperse systems where particles are of different diameters. Two phase media involves partition of the space into disjoint regions with interfaces, a good example would be system with bubbles. In such systems instead of particle numbers, fluctuation of local volume fractions of one phase is of interest,

$$\sigma_v^2(R) =< \tau_i^2(R) > -\phi_i^2 \tag{2.42}$$

where ϕ_i is the global volume fraction of phase i and τ_i is the local volume fraction. For hyperuniformity, $\sigma_v^2(R)$ decays faster than $\sim R^{-d}$. In k-space, similarly a spectral density $\tilde{\chi}_v(\mathbf{k})$ has been defined which employs the same hyperuniformity criteria as of with the structure factor $S(\mathbf{k})$. Size disperse systems can also be treated to be made up of different "phases", which basically are the species of particles with different diameters. For sphere packings of radius a [88],

$$\tilde{\chi}_v(\mathbf{k}) = \frac{1}{V}\Big|\sum_{j=1}^{N} \exp -(\mathbf{k}\cdot\mathbf{r}_j)\tilde{m}(k;a)\Big|^2 \tag{2.43}$$

$$\tilde{m}(k;a) = \Big(\frac{2\pi}{ka}\Big)^{\frac{d}{2}} a^d J_{\frac{d}{2}}(ka) \tag{2.44}$$

Here, V is the volume of the system and $J_\nu(x)$ is the Bessel function of first kind of order ν. Here to note, for point particles, structure factor is given by,

$$S(\mathbf{k}) = \frac{1}{N}\Big|\sum_{j=1}^{N} \exp -(\mathbf{k}\cdot\mathbf{r}_j)\Big|^2 \tag{2.45}$$

So we can see in $\tilde{\chi}_v(\mathbf{k})$ the size disperse particles are treated as point particles with some form factor $\tilde{m}(k;a)$.

One of the issues encountered in computing volume fraction variance in real space is the surface effect of the window, specially since in computer simulations we have a limitation of system sizes. Wu et al. [89] has compared two ways of computing volume fraction as shown in Fig. 2.3. Authors have argued in favour of choosing Fig. 2.3(a) in correctly recovering hyperuniform traits for bi-disperse additive soft core frictionless disks above jamming in two

dimensions.

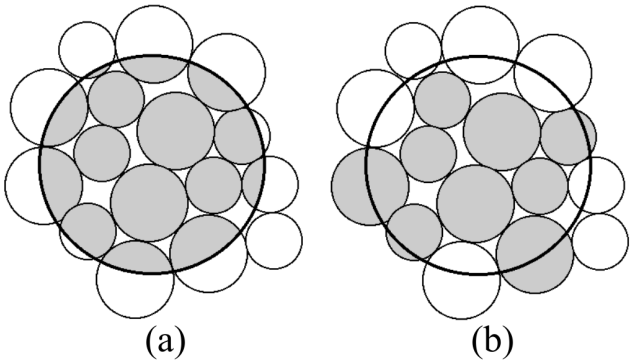

Figure 2.3: Schematic diagram depicting two ways of computing volume fraction for a spherical window: (a) Definition I: For the particles residing close to the window surface, the fraction of volume inside the window is taken into account, (b) Definition II: If the center of the particle lies within the window, its volume is included [89].

Another suggestion to deal with real-space fluctuations was given by Ikeda et al. [90] for a mono-disperse systems above jamming. Instead of treating the centers of the particles as a point particle distribution with a Dirac delta type distribution, a Gaussian density field can be defined, in $3d$,

$$\psi(\vec{x}) = \sum_i f(\vec{x} - \vec{r}_i) \tag{2.46}$$

$$f(\vec{x}) = \left(\frac{\delta}{\pi}\right)^{\frac{3}{2}} \exp(-\delta|\vec{x}|^2). \tag{2.47}$$

δ can be tuned for particle sizes. This is a coarse grained density field and density variance can be obtained as,

$$\Delta^2_\psi(R) = <\psi(\vec{x};R)^2> - <\psi(\vec{x};R)>^2 \tag{2.48}$$

$$= \frac{9\rho}{4\pi R^3} \int_0^\infty \frac{dk}{k} f(k)^2 S(k) J_{\frac{3}{2}}(kR)^2. \tag{2.49}$$

The factor $f(k) = \exp(-(\frac{k^2}{4\delta}))$ represents the modification over point distribution. A coarse grain model like this suppresses local fluctuations and reveals the nature large length scale behaviour more accurately.

2.4.2 Compressibility in search of hyperuniformity

Berthier et. al. [63] showed that for polydisperse jammed systems a good indicator of hyperuniformity is the wave vector dependent compressiblity $\chi_T(k)$ instead of the structure factor. Even though the meaning of isothermal compressiblity in such non-equilibrium system is unclear it was found that compressibility is getting suppressed at large length scale, showing hyperuniformity. See Fig. 2.4.

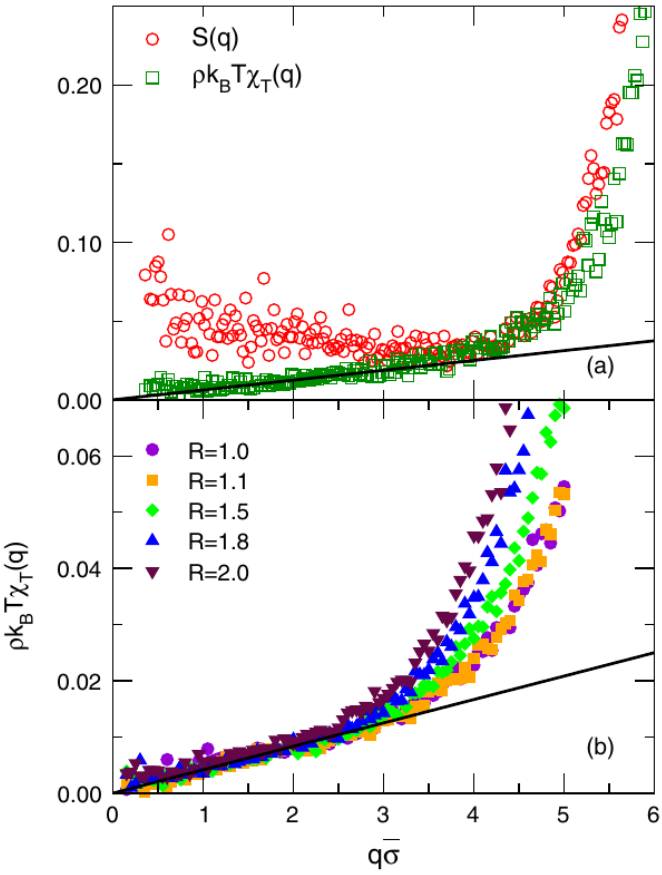

Figure 2.4: (a) In "jammed" state structure factor $S(q)$ and compressibility $\chi_T(q)$ with wave vector q for a $2d$ packing of hard-disks obtained experimentally. In the low wave vector regime it is the compressibility that tends to vanish, showing hyperuniform trend [63]. (b) Compressibility for numerically obtained binary systems with various size ratios, all showing hyperuniformity [63].

2.5 Some aspects of Hyperuniformity

Hyperunifirmity: an inverted critical phenomenon

For a fluid system Ornstein and Zernike [91] had defined the direct correlation function $c(\mathbf{r})$ which is of significance importance in studying fluctuations near the critical point. The total correlation function $h(\mathbf{r})$ can be decomposed into a direct part given by $c(\mathbf{r})$ and an indirect contribution. Especially in Fourier space, the relationship is,

$$\tilde{c}(\mathbf{k}) = \frac{\tilde{h}(\mathbf{k})}{S(\mathbf{k})} = \frac{\tilde{h}(\mathbf{k})}{1+\rho\tilde{h}(\mathbf{k})} \tag{2.50}$$

For hyperuniform systems, $\tilde{h}(\mathbf{k}=0) = -1/\rho$. Therefore in $k \to 0$ limit as $S(\mathbf{k})$ vanishes, the direct correlation function $\tilde{c}(\mathbf{k})$ diverges to $-\infty$. This implies volume integral of $c(r)$ does not exist and real space direct correlation function $c(r)$ is long ranged. This is a complete opposite behaviour from that observed in thermal or magnetic critical points. In thermal or magnetic critical points it is the total correlation function that becomes long-ranged and direct correlation

functions are short ranged. In this sense, hyperuniformity has been termed as "inverted" critical phenomenon.

By the analogy to thermal critical points, the direct correlation function of hyperuniform system is expected to have the following power-law decay,

$$c(\mathbf{r}) \sim \frac{1}{|\mathbf{r}|^{d-2+\eta}}. \tag{2.51}$$

Here, $(2-d) < \eta < 2$ is the new critical exponent of hyperuniformity.

Multihyperuniformity

If each of the components in a system is independently hyperuniform, this makes the total system also hyperuniform. This phenomenon is known as multihyperuniformity. Crystals whose components are periodically arranged are trivial examples of multihyperuniform systems. Disordered multihyperuniform systems are harder to design. A naturally arising example is distribution of cone cells in avian retina [92]. Another example is multi-component plasma in equilibtrium at finite temperatures [93, 94].

Effective hyperuniformity: Hyperuniformity index H

Hyperuniformity is a long wavelength property. But in laboratory experiments and numerical simulations there can be noises and constraints on system sizes. Therefore often we end up with systems that are "nearly" or "effectively" hyperuniform. Effective hyperuniformity can be determined by hyperuniformity index H, as being described below.

From practical point of view, we can hardly obtain a perfect hyperuniform material whose structure factor is completely zero at the origin. So the next best thing in determining hyperuniformity is to introduce hyperuniformity index H defined as follows,

$$H = \frac{S(\mathbf{k} \to 0)}{S(\mathbf{k}_{peak})}. \tag{2.52}$$

$\mathbf{k}_{peak}$ denotes the wave vector $\mathbf{k}$ where the first peak of the structure factor arises. If the value of H is lower than some cut-off, the system is termed to be effectively hyperuniform [95, 88]. Usually a system is characterised as hyperuniform if $H \leq 10^{-3}$, but this is subjective. A good reference can be if H is significantly lower than the disordered liquid phase of the system, it is hyperuniform.

In Fig. 2.5 we show the use of hyperuniformity index in the determination of different phases of amorphous ice [95].

2.6 Hyperuniformity in nonequilibrium systems

Hyperuniformity has been observed in many nonequilibrium states. Here we are listing few such interesting instances, often related to non-equilibrium phase transition.

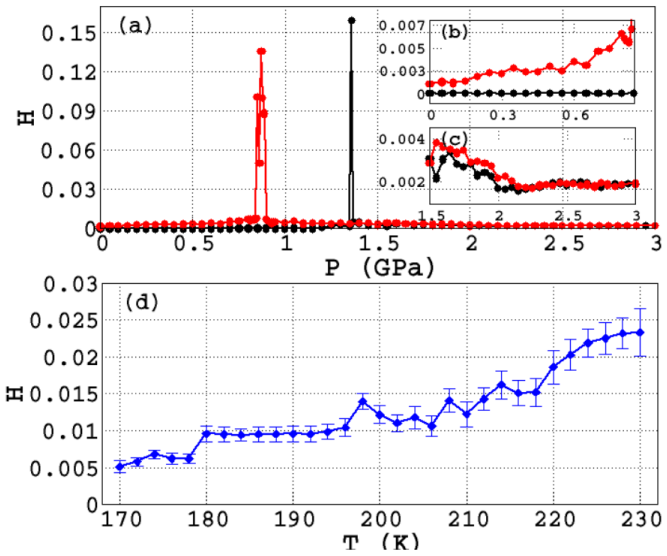

Figure 2.5: Hyperuniformity index $H = \frac{S(0)}{S(k_{peak})}$: (a) During compression of hexagonal (Ih, black) and low density amorphous (LDA, red) ice. Peaks corrrespond to transition from Ih to HDA and LDA to HDA (High density amorphous). (b) and (c) are zoom of the data in (a). (d) H during cooling of liquid water at pressure $P = 0.1$ GPA [95].

2.6.1 Jamming

A jammed packing is a configuration where each particle is in contact with its nearest neighbours. A "strictly" jammed system is the one that does not allow any uniform volume decreasing strains of the system boundary and hence has infinite bulk and shear moduli. A special case is Maximally Randomly Jammed (MRJ) system where the system is maximally random and strictly jammed. We can define a critical jamming density ρ_c or critical volume fraction ϕ_c arising geometrically for a system so that configurations with $\rho > \rho_c$ or $\phi > \phi_c$ will be "jammed". An MRJ state is a prototypical glass which is maximally disordered and perfectly rigid. For sphere packings in MRJ condition the average number of particle contacts are $2d$ where d is the dimensionality.

Torquato and Stillinger has provided a conjecture regaring which type of jammed systems will be hyperuniform:

Conjectture: *Any strictly jammed saturated infinite packing of identical spheres is hyperuniform [79].*

This conjecture excludes systems where there is presence of "rattlers". Another important thing is the saturation condition. This prescribes that imperfections, e.g., removal of certain number of disks from a triangular lattice, can break down hyperuniformity. Till now there is no evidence contradicting this conjecture.

2.6.2 Driven systems

Absorbing state models depicts very good examples of a nonequilibrium transition between an active and an absorbing state. In active state particles evolve with never ending dynamics, where as in absorbing state after a short

transient particles stop evolving. In many absorbing state models this criteria of transition is given by a critical volume fraction ϕ_c, or critical density ρ_c, or strain amplitude γ_c or strain rate $\dot{\gamma}_c$. Hexner and Levin found that in different models of "Manna" universality class [96], namely, a) conserved lattice gas model ($2d$ and $3d$) [97, 98], b) Manna model ($1d$) and c) Random organization model [99] ($1d$ and $2d$) the system exhibits hyperuniformity in absorbing states [74]. In periodically driven microfluidic emulsions at the onset of reversible to irreversible state the system was found to self-organize into hyperuniform state [75].

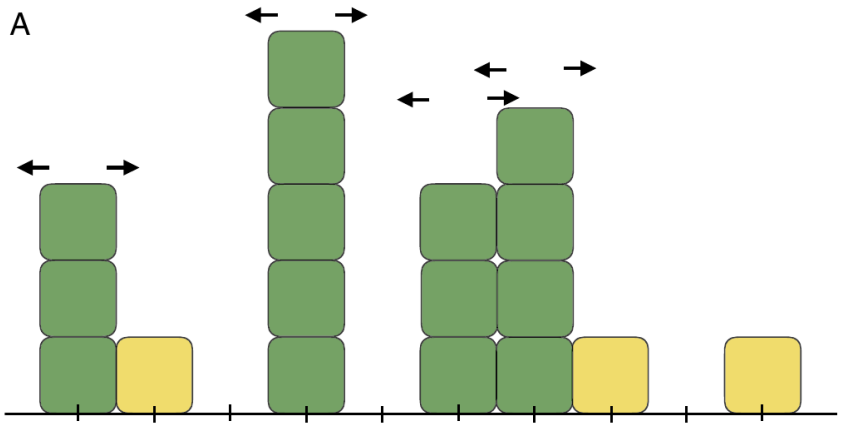

Figure 2.6: Schematic representation of $1d$ Manna model. A site is active if it has $z > 2$ particles. Particles in active state (shown in green) are randomly moved to either right or left generating a new configuration. The dynamics is then repeated [77].

Fig. 2.6 shows a schematic description of manna model [77] in $1d$. Manna model is a bosonic lattice model, each lattice site can be occupied by unlimited number of particles. A particular lattice site is considered "active" if the particle occupancy is above some threshold value, in which case particles are moved to nearest sites. However, total number of particles is conserved via periodic boundary conditions. Initially a distribution of particles on lattice sites are taken. A site considered active if it has more than two particles (a choice made by the authors). The dynamics evolves by moving the particles in active sites to its neighbouring sites randomly. The model exhibits a critical density ρ_c above which system is always evolving, that is in diffusive active state and below this density after a transient an absorbing state can be reached. In the study of periodically driven systems Hexner et al. [77] has shown that hyperuniformity in absorbing states are robust against noise, diffusion or activity.

Fig. 2.7 shows structure factor and density variance for $2d$ Manna model for different numbers of re-activation cycles. We find that for higher number of cycles the system is hyperuniform for larger length scales ξ. Therefore, depending on cycles the system shows hyperuniformity up to **finite length scales**. At $\xi \approx \xi_1 \approx 10$ the configurations corresponsing to cycles$= 1$ shows a transition from hyperuniform to non-hyperuniform state (Fig. 2.7 B). On the other hand, from $S(k)$ we find that the configurations belonging to cycles$= 100, 1000$ becomes more hyperuniform at length scales larger than ξ_1, changing exponent $\alpha \sim 0.45 \rightarrow 1$.

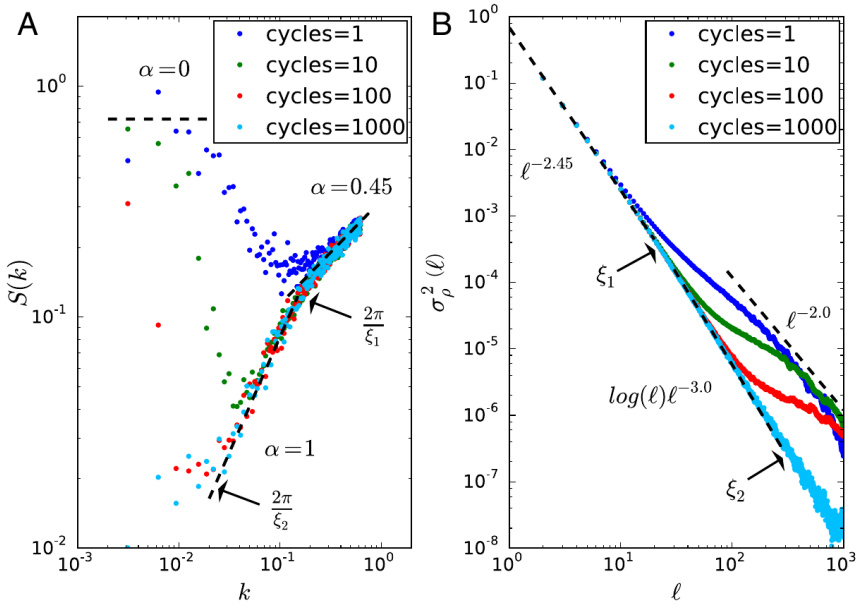

Figure 2.7: For $2d$ Manna model at density $\rho = 1.28 < \rho_c = 1.306$, A) Structure factor $S(k)$, exponent α corresponds to power-law fit and B) density variance with growing length scale l, for different activation cycles. The system is re-activated when absorbing state is reached by random displacements. [77]

Absorbing state transitions are found in a wide range of driven systems. For example, superconducting vortices in oscillating magnetic field [100], driven glassy systems [49], emulsions show this out of equilibrium transition. The robustness of hyperuniformity and tunability in absorbing states demand more exploration.

2.7 Applications

Disordered hyperuniform systems are special since they suppress fluctuations like a crystal arrangement at large length scales and yet they are isotropic in nature like liquids. This in turn can be used in achieving materials with exotic properties. Here we are listing some utilities of hyperuniform systems.

Hyperuniformity has been discovered in biological systems. Two exciting findings are *(i)* distribution of cone cells in avian retina [92] and *(ii)* the immune system [101]. *(i):*A highly regular arrangement of cone cells is most favourable for optimal vision in animals. A two dimensional triangular lattice arrangement of light detectors serves this purpose. Deviation from the ideal case leads to poor visual representation. In a chicken's eye there are five types of cone cells. Four of them are single coloured (violet, blue, green and red) and one responsible for luminance. However inspecting the arrangement of their cone cells it was found that they are not at all well arranged like in a crystal but is disordered. Then how can they have good vision? surprisingly it was discovered that all these component cone cells are arranged in a hyperuniform distribution. The multi-hyperuniform nature of avian cone cell arrangements was the best possible solution for optimal vision, given they are disordered. *(ii):* Adaptive immune system protects organisms from the attack of various pathogens. The receptor proteins in the immune system recognizes the types

of pathogens and interacts with the antigens to build up defense mechanism. Mayer et al. [101] studied the repertoire of lymphocyte receptors in the adaptive immune system and developed general framework for predicting the optimal repertoire that minimizes the cost of infections contracted from a given distribution of pathogens. They found that limited populations of immune receptors can self-organize to provide effective immunity where the distribution of receptor peaks are hyperuniform.

Stealthy hyperuniform systems as has been described earlier are the first disordered systems showing complete photonic band gaps comparable to the size of photonic crystals with added benefit of isotropy [102]. This inspires designing waveguide geometries unhindered by crystallinity and anisotropy [103, 104]. It is predicted that electro-magnetic wave can travel through hyperuniform materials without loss. This prediction involves expansion of effective di-electric constant ε_e [105]. Another study has shown that Lunesvurg lens based on a disordered hyperuniform design has superior radiation properties compared to metamaterial designs [106]. Leseur et al. has demonstrated that it is possible to get high density materials of stealthy hyperuniform scatterers which is transparent for a range of wavelengths [107].

Stealthy hyperuniform system with higher extent of short range order can attain maximal effective diffusion [108]. Dispersion from stealthy materials can have nearly optimal effective conductivity [106]. Super conductor vortices with hyperuniform pinning site geometries delivers higher critical currents [109].

Suppression of volume fraction fluctuations in disordered hyperuniform composite materials results into suppression of crack propagation within matrix phase [110]. Hyperuniform composites can also posses higher brittle fracture strength [111].

Chapter 3

Hyperuniformity in sheared glass

3.1 Introduction

Hyperuniformity essentially is related to the suppression of density fluctuations at large length scales. As we have discussed in previous chapter, in a disordered d dimensional system if we sample various parts of the system with growing window sizes, let say with spherical windows with radius R and the density variance within the window scales as $R^{-(d+\alpha)}$, then we have a *hyperuniform disordered* system $(0 < \alpha < 1)$. For point distributions it is directly related to vanishing structure factor in in the long wavelength limit, i.e. $S(k \to 0) \to 0$ and, as a consequence, a vanishing isothermal compressibility χ_T [79]. Given a system, meaning a set of composition and interaction rules, at which condition will it be hyperuniform? Is there any criticality involved? The most exciting finding in this regard was that jammed disordered hard-sphere packing was found to be hyperuniform [112]. Jamming is a non-equilibrium transition at zero temperature, often observed upon crossing a critical geometrical jamming density ρ_c. Later it was conjectured that maximally random jammed configurations of sphere packings are hyperuniform in nature [59, 113, 114]. In general, jamming happens when a disordered system starts behaving like a solid, with finite yield stress. From the jamming phase diagram (Fig. 1.6) [27, 115] we know of three relevant axes of such transition from flow state to jammed state and vise-versa: temperature, density and applied stress. Therefore it naturally follows to investigate in a disordered system what happens to hyperuniformity under applied stress or driven system. In periodically driven systems often a transition from diffusive to absorbing state is found after a transient where in the absorbing states the particle trajectories become reversible and the system stops flowing. In such scenario, colloidal suspensions showed to have hyperuniformity in absorbing state [76] with $S(k) \sim k^{0.45}$ in the intermediate length scales. Another study on random reorganization model [77] also found hyperuniformity in absorbing states for a finite length scale ξ, which diverges at a critical density ρ_c. Similarly for sheared sedimentation [116], many-particle model [78] hyperuniformity in absorbing states have been discovered.

Glasses when applied to periodic shear deformation also undergo such non-equilibrium transition from absorbing

to diffusive states, known as the yielding transition. Earlier studies have shown as a glass system is mechanically driven for many cycles with strain amplitude $\gamma_{\max}$ there exists a critical yielding amplitude γ_y marking this transition [49, 117, 48, 1]. In this work we perform numerical investigation of a model glass system in $3d$ under cyclic shear deformation and study the nature of fluctuations in the system in terms of hyperuniformity across yielding transition. Our results show hyperuniform trend in absobing state and interestingly enough a dramatic change above yielding. Above yielding as the system exhibits mobile shear band, we show that the glass system has two distinct hyperuniform phases inside and outside the shear band regime.

3.2 Results

We work on the very well studied Kob-Andersen model glass former interacting with Lennard-Jones (LJ) potential at reduced density $\rho = 1.2$ and temperature $T = 1$ in LJ units (See model and simulation for details). From the equilibrated liquid we obtain energy minimized inherent structures (IS) at zero temperature, which we refer as the glass. We shear the IS in Athermal Quasi Static (AQS) limit for many deformation cycles with certain strain amplitude $\gamma_{\max}$ untill the system reaches a steady energy state. We sample the steady state configurations for our analysis and the results are averaged over at least 30 realizations. Our system size is $N = 64000$, unless otherwise stated.

3.2.1 Unsheared system: Compressibility depicting hyperuniformity

At first we study the unsheared inherent structures in contrast to liquid configurations. We find that for our binary mixture, it is not the structure factor $S(k)$, but the isothermal compressibility $\chi_T(k)$ is supressed in glassy state and is relevent for the study of hyperuniformity [63]. For a binary system consisting A and B type particles, it is given by,

$$\rho k_B T \chi_T(\mathbf{k}) = \frac{S_{AA}(\mathbf{k})S_{BB}(\mathbf{k}) - S_{AB}(\mathbf{k})^2}{c_A^2 S_{BB}(\mathbf{k}) + c_B^2 S_{AA}(\mathbf{k}) - 2c_A c_B S_{AB}(\mathbf{k})}, \tag{3.1}$$

where, $c_A = N_A/N$ and $c_B = N_B/N$, and S_{AA} *etc.* are partial static structure factors, defined as, $S_{\alpha\beta}(\mathbf{k}) = \frac{1}{N}\left\langle \rho_\alpha(\mathbf{k})\rho_\beta(-\mathbf{k})\right\rangle$, where $\rho_\alpha(\mathbf{k}) = \sum_{j=1}^{N_\alpha} \exp(i\mathbf{k}\cdot\mathbf{r}_j)$, $(\alpha,\beta) \in (A,B)$. For hyperuniform systems, it is expected that

$$\tilde{\chi}_T(k) \equiv \rho k_B T \chi_T(k) \propto k^\alpha, \tag{3.2}$$

where the exponent α is such that $0 < \alpha \leq 1$. This $\tilde{\chi}_T(k)$ is related to structure factor $S(k)$ as follows [118],

$$\tilde{\chi}_T(\mathbf{k}) = S_{NN}(\mathbf{k}) - [\Delta(\mathbf{k})]^2 S_{CC}(\mathbf{k}). \tag{3.3}$$

$$\Delta(\mathbf{k}) = \frac{S_{NC}(\mathbf{k})}{S_{CC}(\mathbf{k})}. \tag{3.4}$$

Here, S_{CC} is relevant to the concentration-concentration fluctuations and S_{NC} is for number-concentration fluctuations. $S(k) \equiv S_{NN}(k)$, the number-number fluctuation.

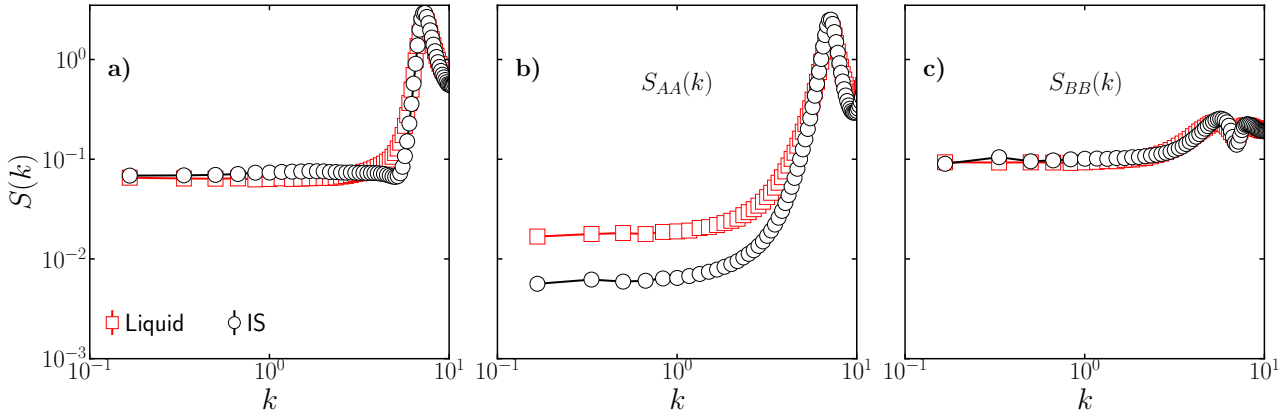

Figure 3.1: (a) Structure factor $S(k)$ for liquid (red square) and inherent structures (black cicrcle), $N = 64000$. (b) and (c) Partial structure factors for A and B type respectively.

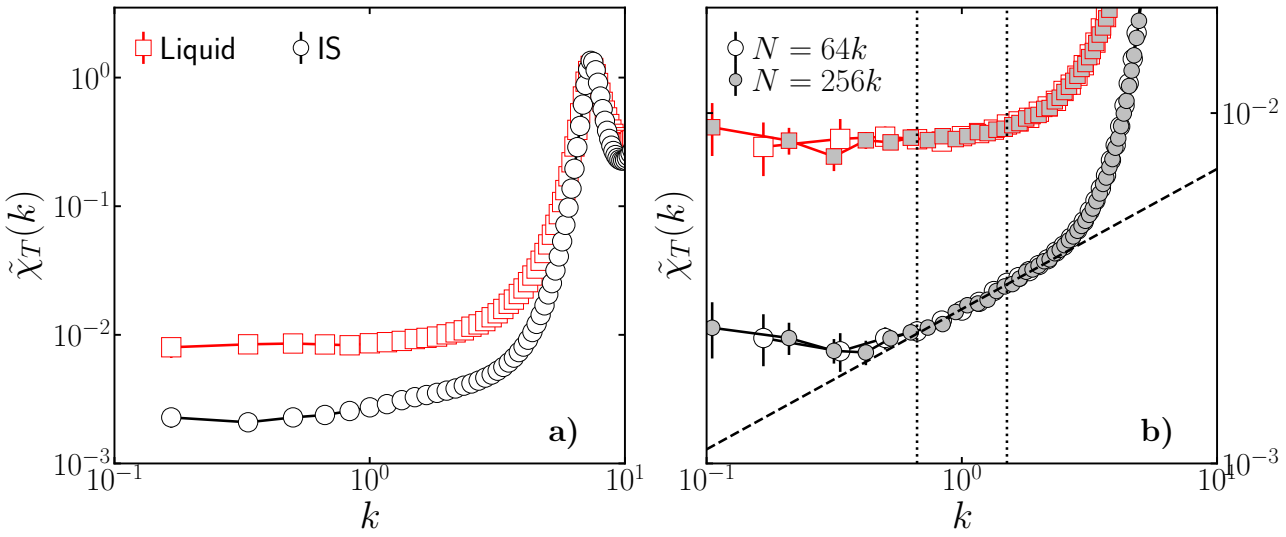

Figure 3.2: (a) Compressibility $\tilde{\chi}_{\mathrm{T}}(\mathrm{k})$ for liquid (red square) and inherent structures (black cicrcle), $N = 64000$. (b) Zoom of $\tilde{\chi}_{\mathrm{T}}(\mathrm{k})$ in low-wave vector regime, for two system sizes, $N = 64000$ and $N = 256000$. Power-law fit shown in broken curve, $k^{\alpha \sim 0.4}$. Vertical dotted lines show the range of fitting.

In Fig.3.1 we plot the total structure factor $S(k)$ and partial structure factors $S_{AA}(k)$ and $S_{BB}(k)$ for both liquid and IS. Only S_{AA} shows a difference in values in $k \to 0$ limit, between liquid and IS. But, we don't find any strong hyperuniform trend, i.e. a power law trend in the structure factors of either the liquid or the IS. On the other hand, when we compute $\tilde{\chi}_{\mathrm{T}}(\mathrm{k})$, from Fig.3.2 we see a clear difference between liquid and IS. In the liquid, the k-dependent compressibility approaches a constant value as $k \to 0$. For the IS, Fig. 3.2 shows that, within intermediate range

of k-vectors, the compressibility is hyperuniform in nature, and follows Eq.3.1. In particular, when fitted on the interval $|\mathbf{k}| = [0.667688; 1.5023]$ corresponding to the length scales $[4.18\sigma_{AA}\ ;\ 9.41\sigma_{AA}]$, we obtain $\alpha \sim 0.40$. We notice, however, that the zero k limit of $\tilde{\chi}_T(k)$ does not drop to zero but attains a finite value. This behavior has been observed in several systems that are named *effectively hyperuniform* [119] but it is the first time that is observed in glasses below jamming. Since hyperuniformity is essentialy related to large length scales, it is important to verify that the limited range of the hyperuniform behaviour is not merely due to finite size of our system. We therefore report here in Fig.3.2(b) two system sizes $N = 64000$ and $N = 256000$ and find that both of them show this hyperuniform trend upto finite length scale. Similar observation has been reported in several other systems [116, 120] and it is not a consequence of finite size effects. This allows us to work with $N = 64000$ for the rest of the work.

3.2.2 Sheared system

We have established that the glass obtained from initial high density and high temperature liquid suppresses compressibility up to a finite length scale. So, now we examine its behaviour in cyclically driven system. As we deform the system for many cycles with strain amplitude $\gamma_{\max}$, each cycle consists of

$$0 \rightarrow \gamma_{max} \rightarrow 0 \rightarrow -\gamma_{max} \rightarrow 0. \tag{3.5}$$

In absorbing states ($\gamma_{\max} < \gamma_{\rm y}$) the steady state energy is lower than the initial IS. This is known as mechanical annealing in glass. As soon as $\gamma_{\max} > \gamma_{\rm y}$ we observe energy rejuvenation, particles start to move chaotically. However, the traditional radial distribution function doesn't capture any structural change from absorbing to diffusive state of the sheared glass system. Therefore if hyperuniformity, a measure of long range correlation and fluctuations, can identify this dynamical transition as a structural one that would open up new questions.

With strain amplitudes: $\tilde{\chi}_{\rm T}(\rm k)$

We compute $\tilde{\chi}_{\rm T}(\rm k)$ in steady states of $\gamma_{\max} \in [0.0, 0.09]$. For our system, the yielding amplitude is $\gamma_{\rm y} = 0.07$ [1]. We sample the systems stroboscopically ($\gamma = 0$) in steady state and average over at least 30 configurations.

Results are presented in Fig. 3.3, which shows clearly different trends for strain amplitudes below and above $\gamma_{\rm y} \approx 0.07$. *(i)* In the absorbing states ($\gamma_{\max} < \gamma_{\rm y}$) the hyperuniform trend of unsheared IS system is preserved. *(ii)* In the diffusive state, $\gamma_{max} > \gamma_y$, two relevant differences emerge with respect to absorbing states. Firstly, the power law exponent changes dramatically as soon as γ_y is crossed, as can be seen from the fit corresponding to $\gamma_{\max} = 0.06$ and $\gamma_{\max} = 0.076$. Secondly, in the lowest accessible wave vector, a strong upturn of $\tilde{\chi}_T(k)$ suggest the presence of strong density fluctuations. Overall, the results presented in Fig. 3.3 suggest a profound difference between the absorbing and diffusive state.

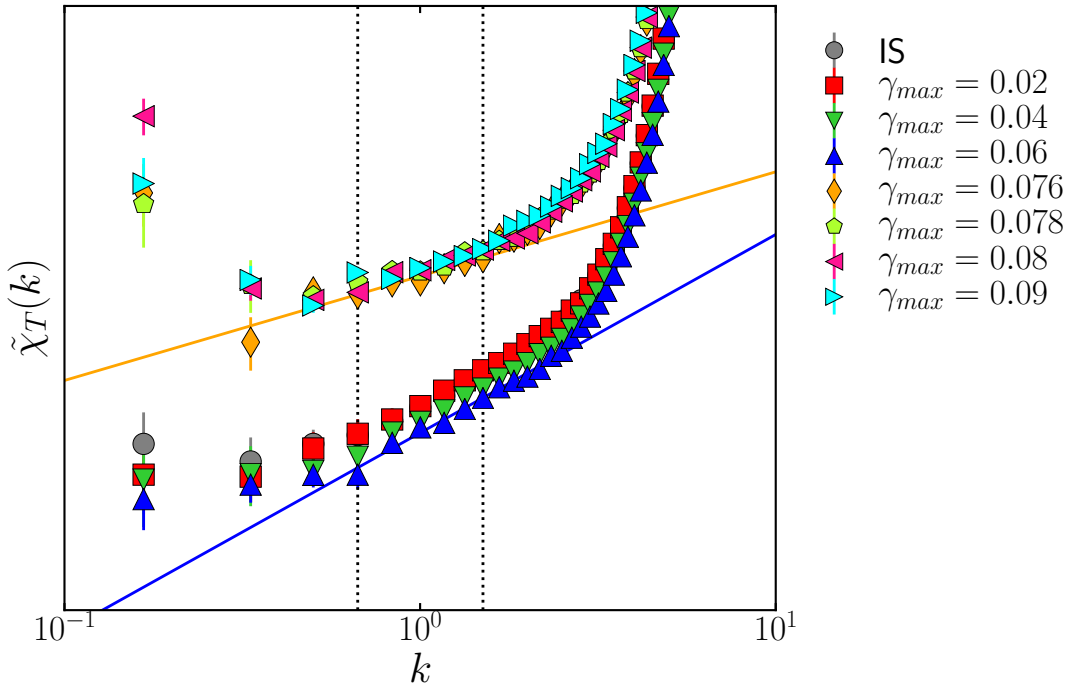

Figure 3.3: Compressibility $\tilde{\chi}_T(k)$ for the cases of shear amplitudes γ_{max} below and above critical yielding amplitude $\gamma_y \simeq 0.07$ are shown with different symbols. Data for IS has also been included. In the cases above yielding, $\tilde{\chi}_T(k)$ has been shifted upwards for clear visibility. The solid lines (blue and orange) show the power law fit to the compressibility curves. The vertical dotted lines mark the wave vector regime fitted with the power law k^{α}.

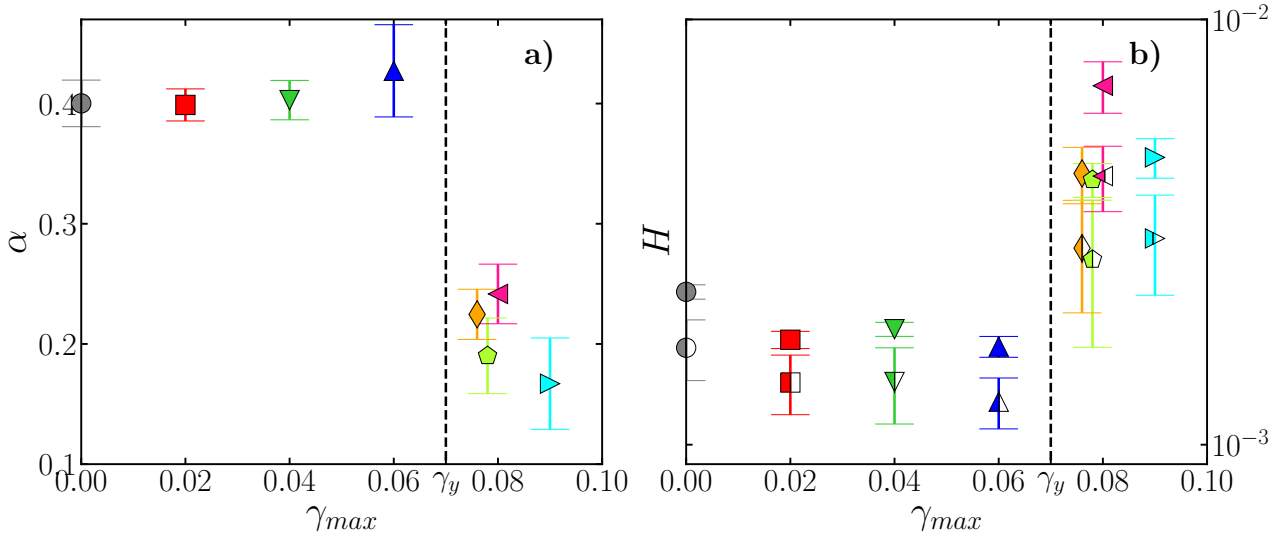

Figure 3.4: (a) The exponent α of power law fit to compressibility $\tilde{\chi}_T(k)$ is plotted against shear amplitude γ_{max}. The value $\gamma_{max} = 0$ is for IS. The vertical dashed line marks the yield amplitude γ_y.
(b) We plot hyperuniformity index H against shear amplitudes γ_{max}. The filled symbols and half filled symbols are for two different routes of estimating H (See in text).

To further quantify the degree of hyperuniformity, we fitted Eq. 3.2 to the compressibility on the same range as in Fig. 3.3 and the results are presented in Fig. 3.4(a). Below yielding, we obtain almost a constant value of $\alpha \approx 0.4$, which is at the same level of that of the unsheared IS. A sudden change, however, is observed as soon as γ_y is

crossed and the exponent α displays a dramatic drop.

The hyperuniform nature of a system can be also verified by computing the *hyperuniformity index* H, which measures how much compressibility has been suppressed by comparing its value in $k \to 0$ limit, with respect to its value at the the first peak [95, 121, 122]. More specifically we define:

$$H = \frac{\tilde{\chi}_T(k_0)}{\tilde{\chi}_T(k_{peak})}, \tag{3.6}$$

where k_{peak} corresponds to the first peak of $\tilde{\chi}_T(k)$. When H is close to 10^{-3} or lower, the system is concluded to be hyperuniform [95, 121, 123, 124, 125]. For the IS, a value of $H \leq 2 \times 10^{-3}$ confirms indeed that our system is hyperuniform. In this work, we estimated H following two routes. In one case, we fit the lowest k twelve points of the $\tilde{\chi}_T(k)$ to a third order polynomial $a_0 + a_1 k + a_2 k^2 + a_3 k^3$ to extract a_0 which is assumed to be a good estimation of the $k \to 0$ limit of the compressibility. We notice that, above yielding $\gamma_{max} > \gamma_y$, the upturn in the compressibility curves in $k \to 0$ limit can make the polynomial fitting procedure misleading and it is for this reason that we use a second approach. In this case, for the $k \to 0$ limit, we used the value $\tilde{\chi}_T(k = k^*)$ where $k^* = 2\pi/L$ is the lowest accessible k-vector. The value of H versus γ_{max} is plotted in Fig. 3.4(b) (half filled symbols). A similar trend as of the exponent α is observed: H decreases as a result of shearing as we approach γ_y and then, above yielding, it jumps to a higher value. This implies that shearing enhances fluctuations in the diffusive states and as a consequence the compressibility of the yielded system is considerably higher.

Real space density fluctuations

In hyperuniform systems, the density fluctuations are suppressed with growing length scales. Hence we now directly examine number density variance in real space for the glass system under shear. we introduce the density variance in real space $\Delta^2(R)$,

$$\Delta^2(R) := \left\langle \rho^2(R) \right\rangle - \left\langle \rho(R) \right\rangle^2 \sim R^{-(d+\alpha)}, \tag{3.7}$$

where R is the radius of the sampling sphere, ρ is the number density within the spherical window of size R and d is the dimensionality. We randomly place the spherical windows in the system and then compute the variance of number density of particles within the windows.

The results of this analysis are presented in Fig. 3.5(a). Here again two clear trends emerge depending on if $\gamma_{\max}$ is below or above γ_y. Below yielding, the exponent α is found to be consistent with those obtained from compressibility $\tilde{\chi}_T(k)$ (Fig. 3.4a). Above yielding, however, one observes deviations from power law behaviour for large window sizes and the exponent α (if one attempts to estimate it) attains negative values, indicating the presence of strong fluctuations.

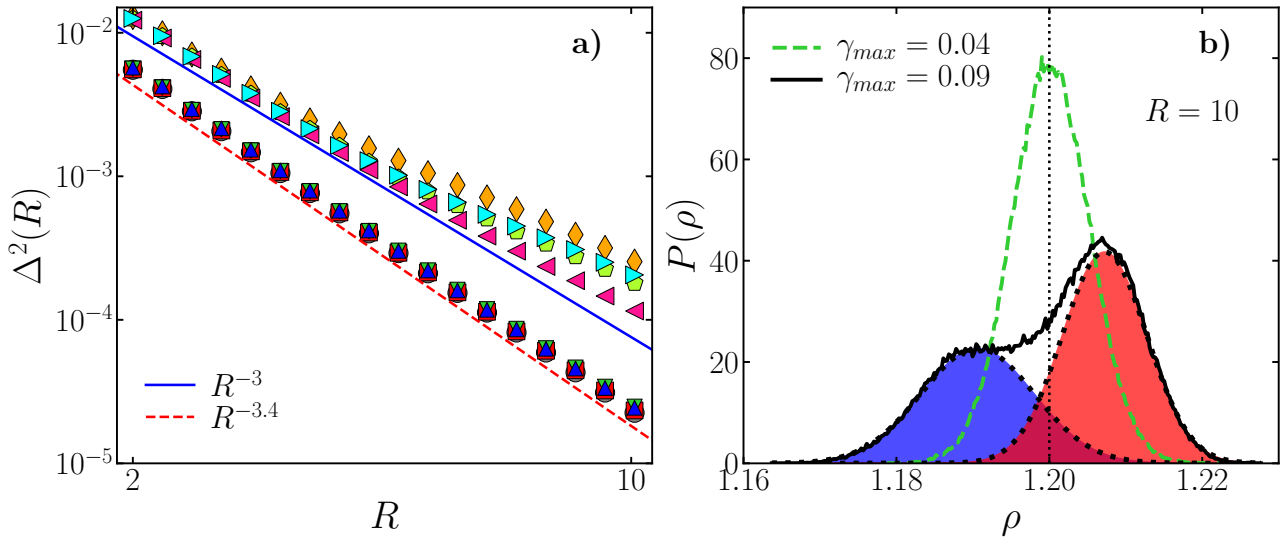

Figure 3.5: (a) Number density variance as a function of sampled-window radius R for the shear amplitudes γ_{max} below and above the yielding amplitude $\gamma_y \sim 0.07$. The symbols used here are same as that of Fig. 3.3. Solid blue line is for reference to a non-hyperuniform system where the dependence is expected to be R^{-3}. The red broken line shows a reference when the variance scales as $R^{-3.4}$.
(b) Local number density distributions of a window of radius $R = 10$ for $\gamma_{max} = 0.04$ ($< \gamma_y$) and $\gamma_{max} = 0.09$ ($> \gamma_y$). Above yielding, the distribution is bimodal, indicating two distinct high and low density regions in the system.

Why at large R we are getting this very puzzling different fluctuations? To answer this question, we investigate in detail the distribution of the local density ρ sampled within a given window of fixed size $R = 10$. As shown in Fig. 3.5(b), the local density distribution shows substantially different behavior below and above yielding. For $\gamma_{\rm max} < \gamma_{\rm y}$, ρ exhibits a unimodal distribution centered around the bulk density $\rho = 1.2$. However, above yielding ($\gamma_{\rm max} > \gamma_{\rm y}$), the distribution becomes bimodal and can be described by the sum of two independent Gaussians, the peaks lying on the different sides of the global density.

3.2.3 In presence of shear band

Above yielding under cyclic shear deformation glass system shows the presence of shear band (SB). In this situation the diffusivity of the system is not homogeniously distributed in space. Rather, a band of particles localized in space, are more mobile compared to others. At this point, we choose the case of $\gamma_{\rm max} = 0.09$ and for the case of $R = 10$, we want to see how these two density profiles observed in Fig. 3.5 b) are distributed in space. For that, we place the windows on the particles, if the local density $\rho < 1.2$, we assign a colour blue, or else red (Fig. 3.6, left).

In Fig. 3.6, we compare the low and high density regime with the shear band present in the system (Fig. 3.6, middle) and we find they are localized and correlated, low density regime depicting the mobile shear band, perpendicular to X. In this case, along the X direction, we have normalized fraction of windows belonging to either blue ($\rho < \rho_c$) or red ($\rho > \rho_c$) class, such that their sum is 1. We see a very smooth variation of this distribution (Fig. 3.6, right). Now, we consider three sub volumes as marked in horizontal colour bars just adjacent to the fractional variation plot:

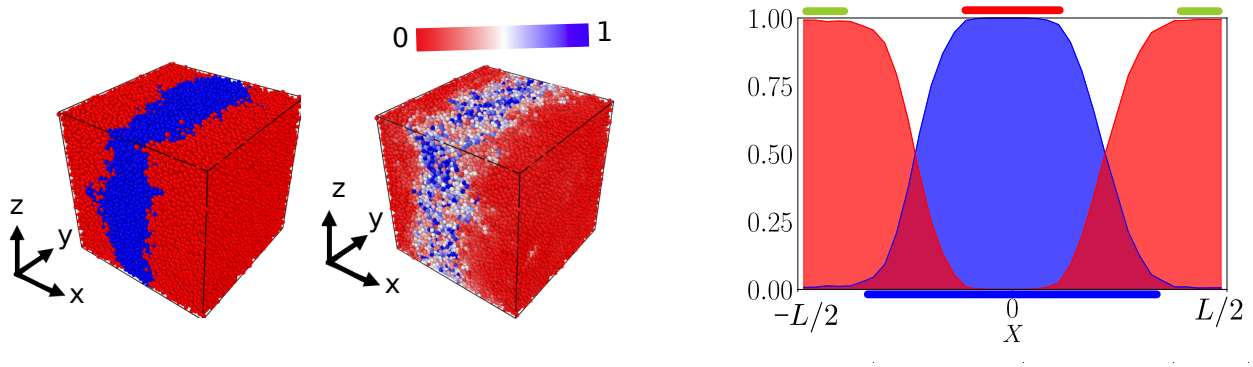

Figure 3.6: Left: For $\gamma_{\max} = 0.09$, we randomly place spherical windows of size $R = 10$ in the system and compute local density ρ. If $\rho < 1.2$ (> 1.2), we assign the colour of central particle as blue (red). we see that they are localized. Middle: We compare it with the displacements of the particles in steady state from one cycle to the next to identity shear band, which is perpendicular to X in this case. The blue particles are more mobile ($\approx 1\sigma_{AA}$) compared to the red particles ($\approx 0.001\sigma_{AA}$)
Right: Along X fraction of particles belonging to either low (blue) or high (red) density. The bars outside denote three regime of interest: *(i)*red bar: Inside shear band, *(ii)* green bar: Outside shear band and *(iii)* shear band along with the interface.

(i) red bar (Inside SB), (ii) green bar (Outside SB) and (iii) blue bar (Inside SB + Interface). We shall later refer to these three regimes to understand better how the presence of shear band effects the fluctuations.

To locate the shear band precisely we compute the mean square displacements of the particles between two consecutive deformation cycles along the direction orthogonal to the plane of the shear band (here X). In this case, with XZ shear, we find that the shear band forms in the YZ plane. We can find the width of the shear band by fitting a Gaussian function to this MSD, as shown in Fig. 3.7(a). Once the position and extent of the band is known, we compute local density ρ along the shear direction in sub volumes parallel to shear plane in Fig. 3.7(b). Inside the shear band the density is lower as already reported in Ref. [1]. Indeed, we are now certain of the correspondence of this low-density sub-volume of Fig. 3.6 to the center of a dynamical shear band. Additionally, we compute the variation in $c_A = \frac{N_A}{N}$ along X. From Fig. 3.7 (c) we find that not only the density but also the composition of the system varies with the shear band. Our results thus confirm that in the yielded system we indeed have distinct structural characteristic inside and outside SB.

So far we have established that there is a relation of the high fluctuations above yielding with the shear band. Now we ask, what is the exact nature of the fluctuation or hyperuniformity inside and outside the shear band and how this effects the overall system.

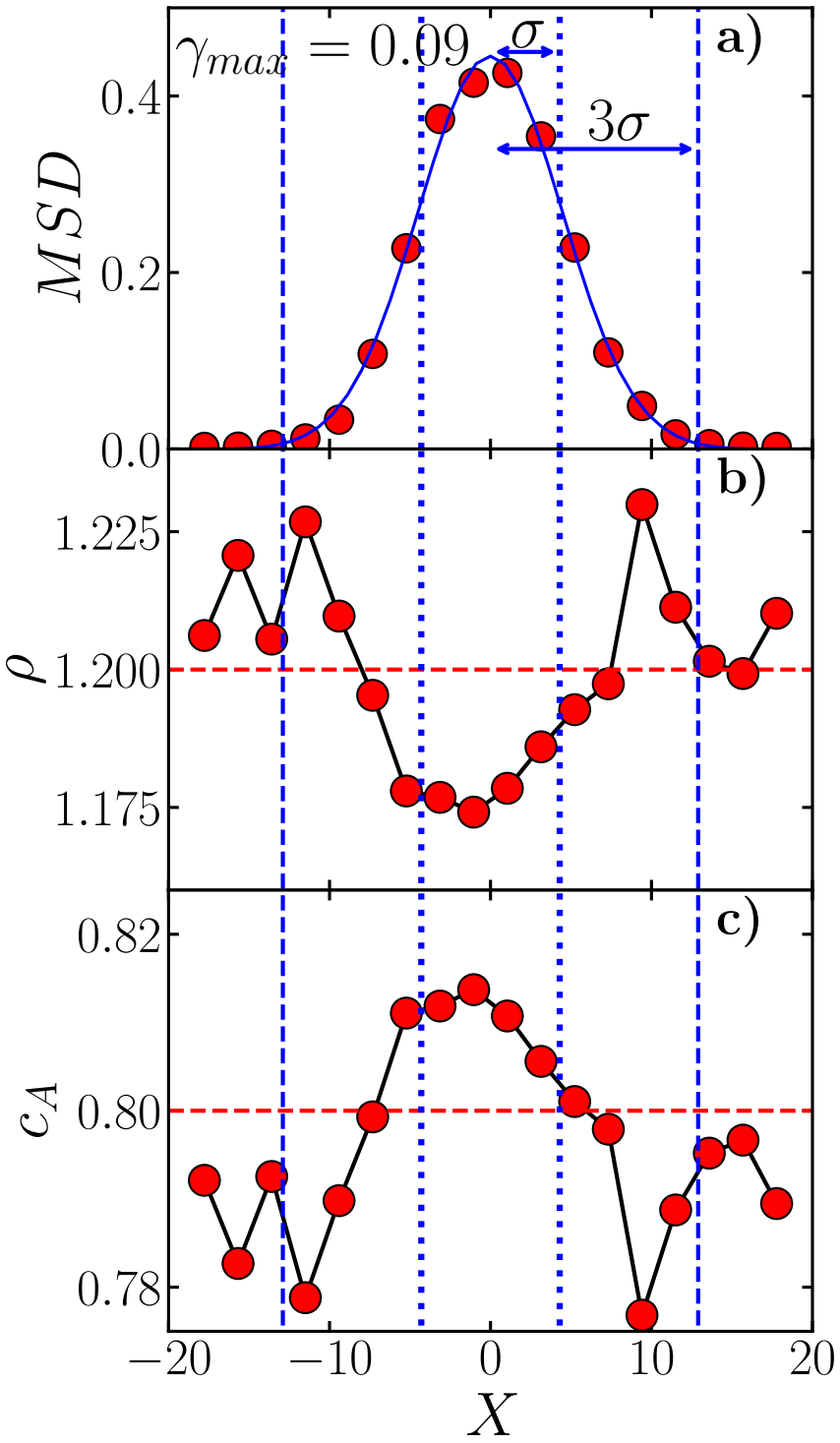

Figure 3.7: a) For an amplitude above yielding $\gamma_{max} = 0.09$ the mean square displacements of the particles along X direction between two consecutive deformation cycles is plotted in red circles. A Gaussian fit is shown as the blue curve.
(b) Along shear direction X, the local density ρ in slabs parallel to the $Y - Z$ plane is plotted, which has a dip in the shear band. Global density $\rho = 1.2$ is shown as a broken red horizontal line for reference.
(c)Along X, local concentration of A type particle $C_A = \frac{N_A}{N}$ is plotted, which also shows a variation across the band.

Compressibility $\tilde{\chi}_{\mathrm{T}}(\mathrm{k})$:

The existence of a large interface between two different density regions might be the origin of the low k upturn in the $\tilde{\chi_T}(k)$ observed in Fig. 3.3. To confirm this expectation, we compute the compressibility, for the case of $\gamma_{max} = 0.09$, restricting the $\mathbf{k}$ vectors to planes parallel ($k_x = 0$) and perpendicular ($k_y = 0$ and $k_z = 0$) to the shear band plane. The results are displayed in Fig. 3.8 a). It is evident that, when k is parallel to the shear band, the hyperuniformity features observed below yielding in Fig. 3.3 are recovered. On the other hand, across the shear band, the density fluctuations are enhanced by the presence of the interface between the shear bands.
At this point, a question naturally arises, how the k-space compressibility behaves in the sub-volumes inside and outside of shear band.? We compute compressibility in sub-volumes by choosing, $k = k(k_x, k_y, k_z)$ with $k_y, k_z = \frac{2\pi}{L}(n_y, n_z)$ and $k_x = \frac{2\pi}{l}(n_x)$. Here, l is the width of the sub-volume along X. From Fig. 3.8 b), we find that, when we include the interface, that follows the non-hyperuniform trend of the overall system. But, inside and outside shear band, even though there are fluctuations, we can see the trend to be hyperuniform.

Real space fluctuations:

Now we turn to real space analysis and directly measure density variance with reference to the shear band. We again consider a case of $\gamma_{max} = 0.09 > \gamma_y$, for which we have a shear band in the YZ plane. Then to probe the number density variance inside the shear band we place the spherical windows of radius R such that the volume of the windows lie between $\pm\sigma$ from the center of shear band (σ obtained from the Gaussian fit to the MSD profile). To probe the variance outside the shear band we place spheres such that their volume resides in regions between $\pm\ \frac{L}{2}$ to $\pm(\frac{L}{2} - \sigma)$. We restrict ourselves to smaller R, since we are dealing with narrow sub-volumes.

As shown in Fig. 3.9 a) for the case of $\gamma_{\max} = 0.09$, we find that for both inside and outside shear band the variance scales as $R^{-3.4}$, showing hyperuniformity. But, for the full system, as has been discussed earlier, we see higher fluctuations disrupting hyperuniformity. We recover the trend of the full system when we include a broader region in the shear banded part of width $\pm 3\sigma$. This includes the interface between the regions of higher and lower densities outside and inside the shear band. We confirm that it is the interface between the states that disrupts hyperuniformity. We repeat the variance calculation for all shear amplitudes to find the dependence of exponent α with γ_{max} in the presence of a shear band. Below yielding, density fluctuations across the system have similar character showing hyperuniformity and are the same level as the ones obtained in k-space and presented in Fig. 3.4 a). Above yielding the behaviour is very similar for the cases inside and outside the shear band. In both regions, we recover the same level of hyperuniformity as below yielding. However, if we enlarge the window of sampling in the shear band such that the interface is included (as marked in the Fig. 3.6 c) and described earlier), the hyperuniformity is completely lost and similar results as in Fig. 3.4 a) are recovered. We conclude that the interface between the two regions of

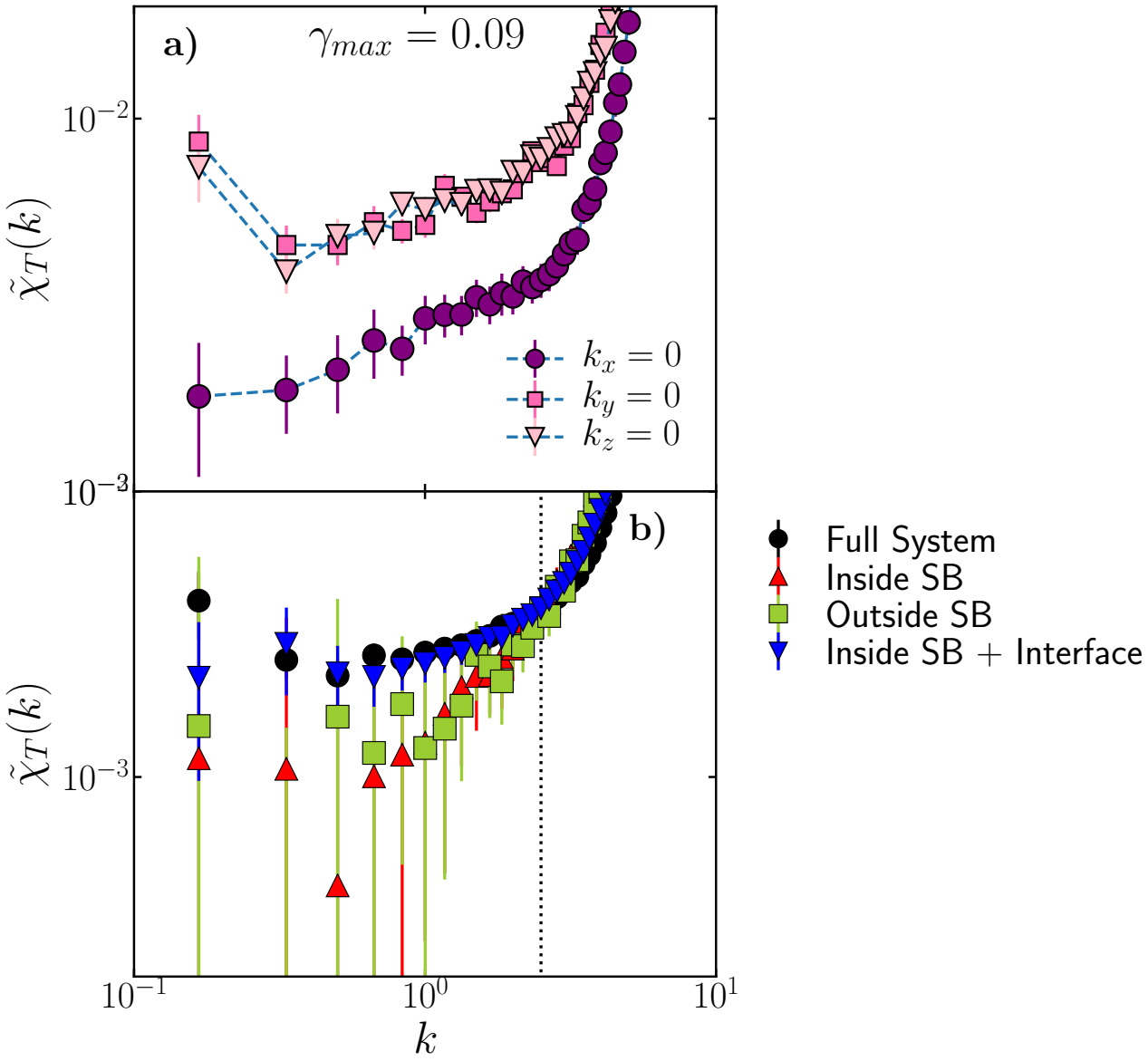

Figure 3.8: We choose one case: shear amplitude $\gamma_{\max} = 0.09$, where the shear band is perpendicular to X, as has been shown in the snapshot in the Fig. 3.6.
(a) Compressibility $\tilde{\chi}_{\mathrm{T}}(\mathrm{k})$ corresponding to different wave vector orientations for this $\gamma_{\max}$ is computed for the whole system. Cases (i) $k_x = 0$, (ii) $k_y = 0$ and $k_z = 0$ correspond to wave vectors being parallel($k_x = 0$) and perpendicular to shear plane. For the perpendicular case, we see an upturn at the lowest wave vectors.
In (b): The compressibility $\tilde{\chi}_{\mathrm{T}}(\mathrm{k})$ has been calculated for sub volumes of the system belonging to different parts w.r.t. shear band (see text). The vertical dotted curve shows the reference k value where the compressibility curves corresponding to different sub volumes have been shifted and converged to have a better sense of the trends of the curves. Black circle: for the full system. Red up triangle: Inside shear band, Green squares: Outside shear band and Blue down triangle: In the shear band regime , which includes the interface of higher and lower density sub-volumes.

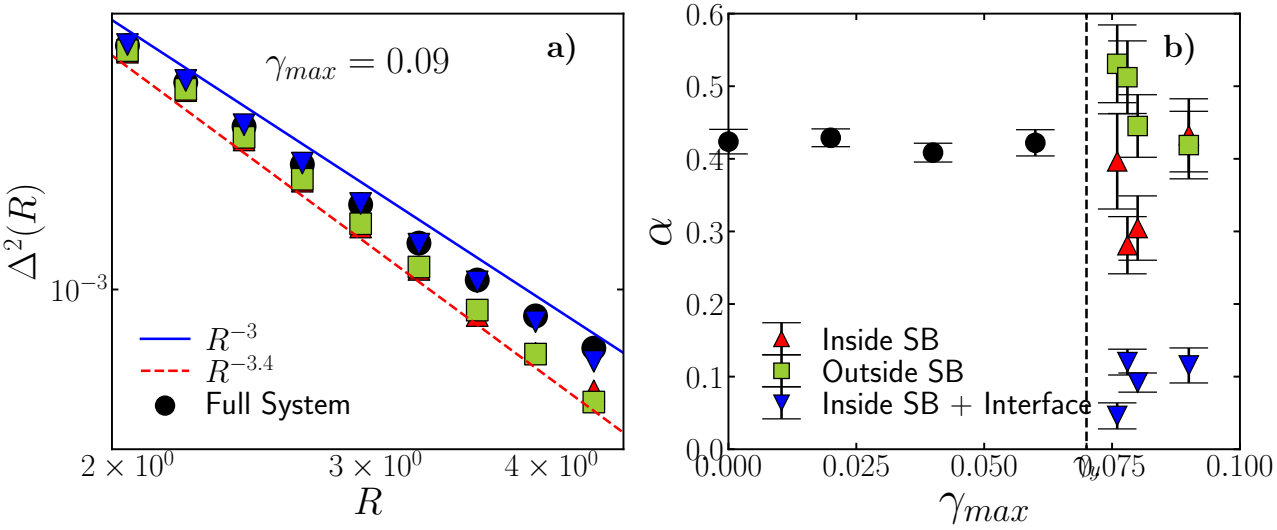

Figure 3.9: (a): Number density variance in spherical windows as a function of its radius R for shear amplitude $\gamma_{max} = 0.09$ (above yielding) calculated in different sub volumes of the system w.r.t. the shear band. For reference, we plot solid blue and broken red curve with R dependence R^{-3} and R^{-4}.
(b): Number density variance exponent α (see text for details) for the cases of γ_{max} below yielding amplitude γ_y are shown as black circles. When the interface is included, the exponent drops to low values indicating a lack of hyperuniformity. Separately inside and outside the shear band the system is hyperuniform.

different densities, as a consequence of shear band formation, is responsible for the disruption of hyperuniformity.

3.3 Discussions

3.3.1 Temperature dependence of hyperuniformity in IS

We have found that for Kob Andersen system at high density $\rho = 1.2$ the inherent structure obtained from liquid at a high temperature $T = 1$ to be hyperuniform up to finite length scales. We also found that in annealed absorbing states due to cyclic shear the hyperuniform nature sustains. The other avenue to get a low energy glass is of course by initially preparing a lower temperature equilibrated liquid and then obtain the IS. Here we seek the temperature dependence of hyperunifom nature in IS obtained from liquids prepared at different temperatures. From Fig. 3.10, we find that the IS of high temperature liquid is showing the hyperuniformity whereas for low temperature, hyperuniformity is lost.

We plot the fitted power law exponent α with temperature in Fig. 3.11 b). It shows that above onset temperature of glass transition, the IS is hyperuniform at a constant level. Below the onset temperature, hyperuniformity is lost. We have compared the energy of IS in Fig. 3.11 a), where we also plotted steady state energies of absorbing states of IS at $T = 1.0$. We have found these absorbing states to be hyperuniform. Interestingly the IS configurations of equivalent energy of low temperature liquids are not.

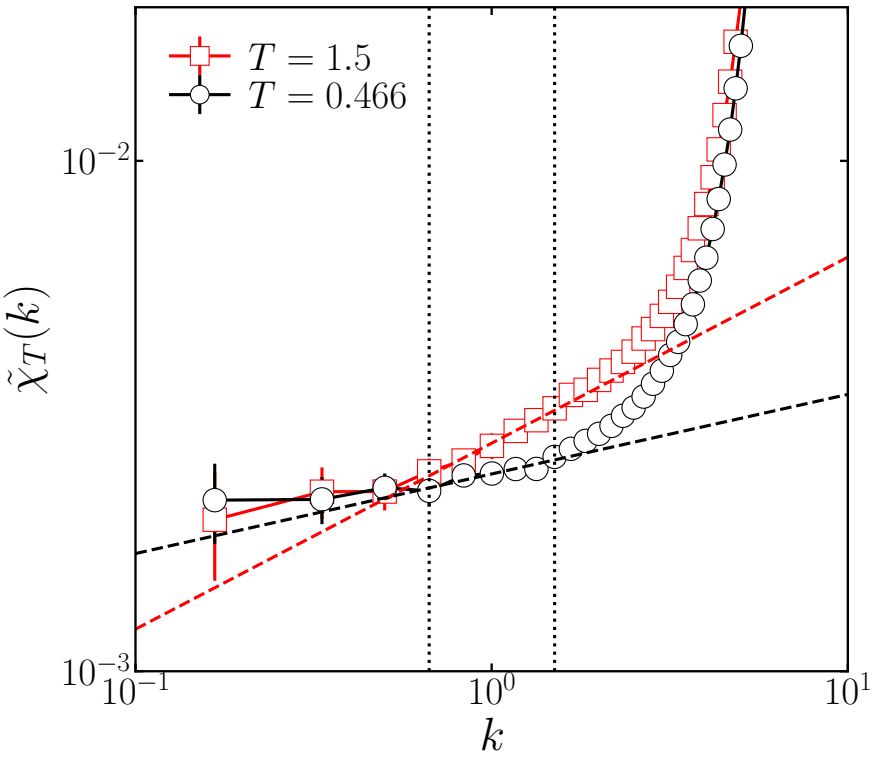

Figure 3.10: $\tilde{\chi}_{\mathrm{T}}(\mathrm{k})$ of inherent structures obtained from high $T = 1.5$ and low $T = 0.466$ temperature, at density $\rho = 1.2$. Broken curves are power-law fits in the range of wave vectors marked by vertical dotted lines.

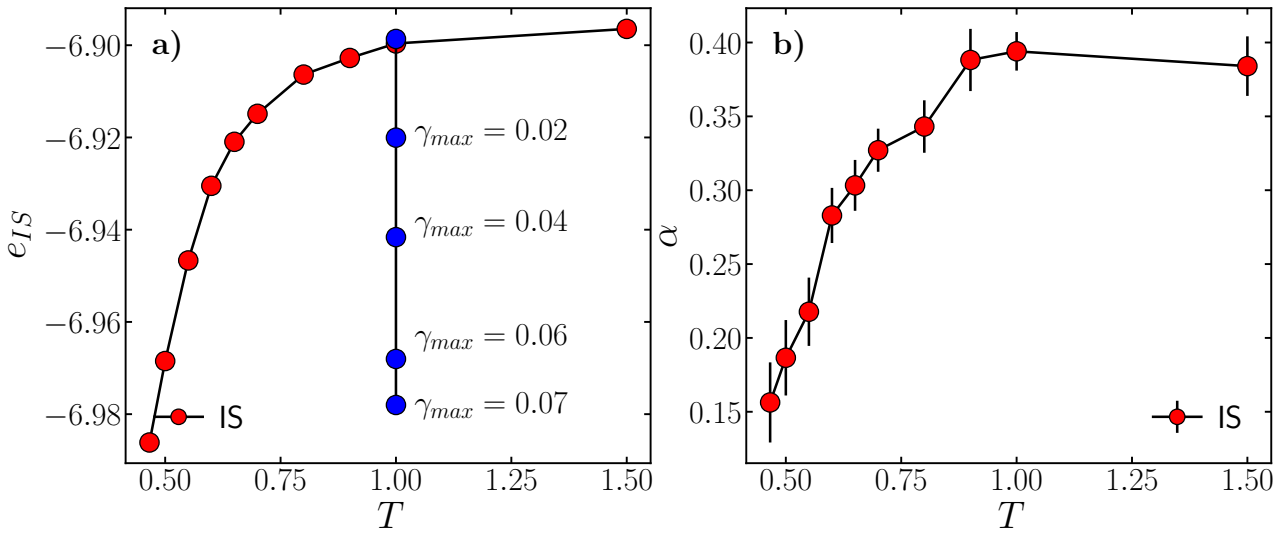

Figure 3.11: (a) Energy of IS at different temperatures in red circle. Energy of absorbing states of IS at $T = 1$ under cyclic deformation. (b) Hyperuniformity exponent α obtained from $\tilde{\chi}_{\mathrm{T}}(\mathrm{k})$ of IS with temperature.

3.4 conclusions

Hyperuniformity has been claimed to be a new exotic state of matter with possible applications with special optical features, experiments showing complete photonic band gaps [104, 126]. Here we have investigated hyperuniformity in a model glass and has extablished that high density glasses produced from high temperature are hyperunifrom upto finte length scale, in our case of the order of 10 diameters. We also studied yielding criticality from the context of hyperuniformity as the glass is subjected to cyclic shear deformation. Previous work has established that under cyclic deformation, a sharp boundary may be identified between a pre- and post-yield regime, corresponding to deformation amplitudes $\gamma_{\rm max} \leq \gamma_{\rm y}$ and $\gamma_{\rm max} > \gamma_{\rm y}$ respectively, and after a transient, these regimes correspond to absorbing and diffusive states when one follows the particle positions stroboscopically at the end of each cycle. With cyclic shear, the glass anneals progressively [1, 51]. We find that the glass remains hyperunifrom in absorbing states , with almost constant hyperuniformity exponent α. With annealing, the compressibility is very slightly suppressed, as reflected by hyperuniformity index H. Above yielding, we demonstrate that hyperuniformity of the system as a whole is lost as a result of increased density fluctuations associated with the formation of an interface between two regions with different densities in presence of shear band. Two dimensional compressibility $\tilde{\chi}_{\rm T}({\rm k})$ parallel to the shear band is hyperuniform and diverges when perpendicular component of wave vector is considered.

If we restrict our evaluation of the fluctuation inside and outside this shearband, excluding the interface, the system continues to be hyperuniform in the same manner as the sheared glasses below yielding. This manifests *directional hyperuniformity* in yielded system. Past studies have considered systems which exhibit hyperuniformity homogeneously in space. Here we demonstrate, for the first time, the possibility of coexistence of hyperuniform regions in a driven glass system.

Chapter 4

Local structures and plastic rearranegements

4.1 Introduction

In the study of rheology, where and how a system will break is one of the fundamental questions. In case of crystals with transnational long range orders theories and experiments suggest that it is the dislocations or the so called defects in crystalline arrangements that initiate flow in the system under applied shear. In absence of such ordered structures where will plastic rearrangements take place in amorphous system is quite a tough question. However, in the spirit of identifying defects the existing theories start with the assumption that there exists local "*soft spots*" or "*shear transformation zones (STZ)*" in the system, constituting approximately $8-10$ particles which are more probable to rearrange under shear stress. This assumption of heterogeneous response to applied deformation seems reasonable as we know for example that the super cooled glassy systems also show dynamical heterogeneity which people have tried to connect with their local structural properties. We shall discuss this point shortly in Methods. Before going further into the basic principals of these theories, let us discuss the nature of plastic rearrangements.

When we deform a system, we want to identify the particles undergoing plastic rearrangements. A well accepted and successful way to do so is the calculation of minimized non-affine displacement $\mathrm{D}^2_{\mathrm{min}}$. Per particle $\mathrm{D}^2_{\mathrm{min}}$ is a measure of local strain, obtained by minimizing the actual mean square displacements of neighbouring atoms compared to what would have been their displacement under uniform shear.

$$\mathrm{D}^2_{\mathrm{min}}(t,\Delta t) = \frac{1}{n}\sum_n \sum_i \Big(\big[r^i_n(t) - r^i_0(t)\big] - \sum_j (\delta_{ij}+\varepsilon_{ij})\big[r^i_n(t-\Delta t) - r^i_0(t-\Delta t)\big] \Big)^2 \tag{4.1}$$

Here, we are computing $\mathrm{D}^2_{\mathrm{min}}$ at time t w.r.t the configuration at a prior time $(t-\Delta t)$ for a particle whose coordinate

is denoted by r_0^i. The (i,j) denote the spacial (x,y,z) components, therefore the sum on (i,j) runs from 1 to 3. n is the number of neighbours of this particle. The term $(\delta_{ij}+\varepsilon_{ij})$ represents a transformation matrix that minimizes the non-affine displacement. δ_{ij} is the standard Kronecker delta and ε_{ij} can be determined by the following sets of equations,

$$\varepsilon_{ij} = \sum_k X_{ik} Y_{jk}^{-1} - \delta_{ij} \tag{4.2}$$

$$X_{ij} = \sum_n \left[\left(r_n^i(t) - r_0^i(t) \right) \left(r_n^j(t-\Delta t) - r_0^j(t-\Delta t) \right) \right] \tag{4.3}$$

$$Y_{ij} = \sum_n \left[\left(r_n^i(t-\Delta t) - r_0^i(t-\Delta t) \right) \left(r_n^j(t-\Delta t) - r_0^j(t-\Delta t) \right) \right] \tag{4.4}$$

For a model $2d$ binary glass system at very low temperature under shear the intensity plots of $\mathrm{D}^2_{\min}$ is shown in Fig. 4.1 from the paper of Falk and Langer [5].

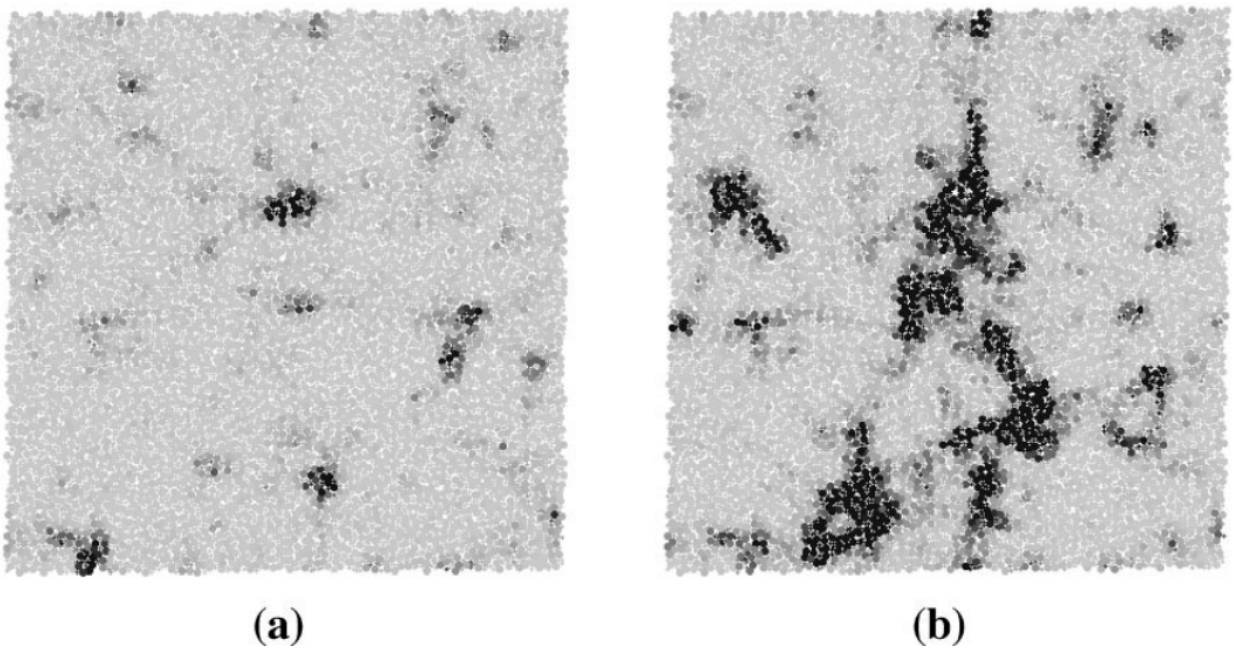

Figure 4.1: Intensity plots of $\mathrm{D}^2_{\min}$ in sheared configuration with $\Delta t = 10$ and $\Delta t = 30$ in (a) and (b) [5].

Fig. 4.1 shows that in shorter time $\Delta t = 10$, the re-arrangements are localized events and in larger time $\Delta t = 30$, the regions of rearrangements are bigger in size with an appearance of band formation. So, the important thing to note is that there are some spots where collectively few particles initiated the rearrangements and in time further some other particles participated in the changes of local stress through plasticity.

A zoom of such a STZ is shown in Fig. 4.2. We find that the local structure is not significantly altered.

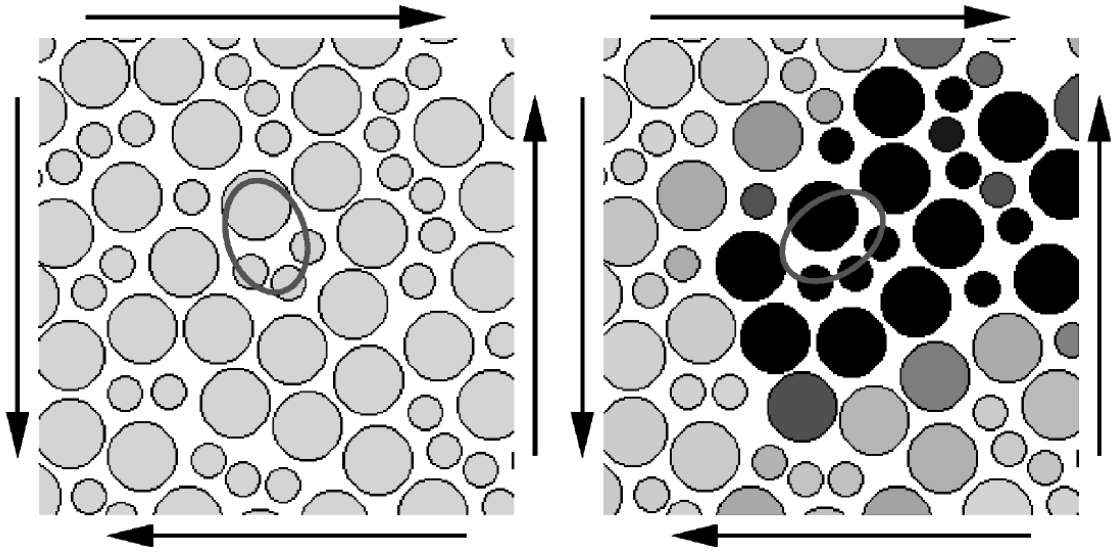

Figure 4.2: A zoom of a shear transformation zone identified with D^2_{min}, snapshots correspond to before and after the transformation due to shear. They grey scale is same for these two snapshots and scaled as per particle D^2_{min} values [5].

So a natural question arises what was special about the local arrangement of the particles inside a STZ prior to the deformation. These STZs appear and disappear in the system and theories of the dynamics of shear transformation zone stands on the basis of two-level property of such systems, where it is assumed that both the states before and after the transformation are equally stable configurations. A short description of the theories is given below.

Shear Transformation Zone (STZ) theory:

STZ theory proposes a dynamic equation for density of states related to the transition of STZ states. Following Falk and Langer [5], the hypothesis is that the STZs are detectable from local geometry. The assumption is that, at a meso-scale level there exists a definite value of yield stress for a given system and the plastic deformations diverge upon approaching to this yield stress, after which the system flows viscoelastically. As a consequence of the two-level system assumption, a STZ can toggle between two accessible states but cannot have repetitive transformation in the same direction and thus giving a limit of maximum deformation up to which the zone remains intact.

The system is considered to have a set of STZs and we are interested in the probability of transition of these STZs. The basic assumption of this theory is that this probability is proportional to the excess free volume V^* available to the particles in the zone. A simplification at this level is to consider that the free volume of the total system is approximately,

$$\Omega - Nv_0 = Nv_f.$$

Here, Ω being the volume of the total system, v_0 the estimated per particle volume. From this the number of states follows to be $(\frac{v_f}{h})^N$. This is in analogy to planks constant but means nothing more. From thermodynamics, we can now have an expression for entropy S and a quantity χ analogous to temperature as follows,

$$S(\Omega,N) = N \ln \frac{v_f}{h} \approx N \ln \frac{\Omega - N v_0}{Nh}.$$
$$\frac{1}{\chi} = \frac{\partial S}{\partial \Omega} \approx \frac{1}{v_f}.$$

Then, analogous to thermal activation, the activation factor for a zone will have a form $\exp(-\Delta V^*/v_f)$. Finally if two states of STZ are denoted by $(\pm)$, and $n_\pm$ is the density of states in these two states, then the proposed dynamical equation is,

$$\dot{n}_\pm = R_\mp n_\mp - R_\pm n_\pm - C_1(\sigma_s \dot{\varepsilon_s}^{in}) n_\pm + C_2(\sigma_s \dot{\varepsilon_s}^{in}) n_\mp.$$

First two terms are for the rate at which a $(\pm)$ state changes to $(\mp)$ state and vise versa. Last two terms are for the creation and annihilation of the states which is proposrtional to the irriversible work done on the system, $\sigma_s \dot{\varepsilon_s}^{in}$. The total strain $\varepsilon = \varepsilon^{el} + \varepsilon^{in}$, with elastic and inelastic components and σ_s is the shear strain.

Soft vibrational modes

When a stable system is sheared, particles have to overcome e certain energy barrier in order to flow or rearrange. These energy barriers are related to the harmonic properties such as vibrational frequency [127]. For a system of N particles in d dimension, one can construct the Hessian matrix [128],

$$H_{ij} = \frac{\partial^2 U(\mathbf{r}_1, \mathbf{r}_2, .., \mathbf{r}_N)}{\partial \mathbf{r}_i \partial \mathbf{r}_j}$$

Where $U(\mathbf{r}_1, \mathbf{r}_2, .., \mathbf{r}_N)$ is the Hamiltonian. H being a symmetric matrix, it will have real eigen values $\{\lambda_i\}_{i=1}^{dN}$. Normal modes will have frequencies, $\omega_i = \sqrt{\lambda_i}$. Low frequency vibrational modes have lower energy barriers to rearrangements when sheared. N_m lowest energy modes are identified and N_p particles in each of these modes with largest polarization vectors are chosen to build "*soft*" spots in the system. The values of N_m and N_p can be optimized in connection to the plastic displacements [129]. Result for a $2d$ glass system is shown in Fig. 4.3

From local structures

The theories of "*soft*" spots suggest that like the dislocations in crystals, for amorphous solids also, local structural arrangements probably play a significant role in the response to applied deformation. On of the interesting works related to finding this correlation and relevant to our work is by Peng et al. [130]. Employing that atomic symmetries

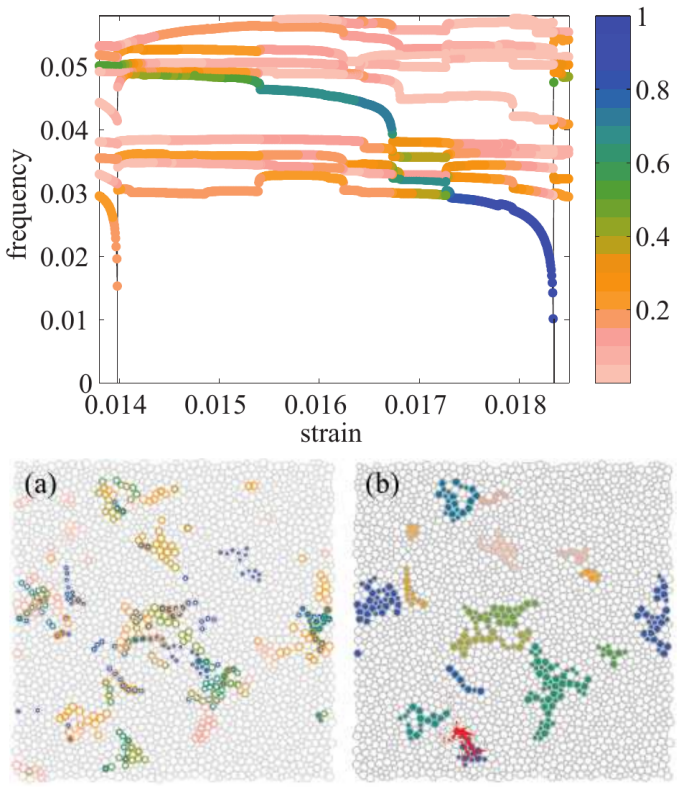

Figure 4.3: The upper pannel shows 10 lowest vibrational frequencies for different values of applied strain for a $2d$ binary glass. In the lower panel (a) shows the plastic displacements and (b) soft spots identified with the vibrational mode analysis at a strain value $3.3X10^{-3}$. Highlighted particles are identified with the chosen values of $N_m = 30$ lowest frequency modes and $N_p = 20$ particles with largest polarization vectors [129].

can be a general way to capture local structures, a Voronoi tessellation method was adopted. This method can identify number of i-edged faces n_i, in a polyhedron. This reflects the local symmetry of the central atom. The triangle, tetragon and hexagon faces have the local translational symmetry feature, while the pentagon faces reflect the local five fold symmetry LFFS. An interesting aspect of this is an icosahedral polyhedron consists of 12 pentagon faces and in many systems icosahedral cluster has been found to be correlated with the dynamical slow down of super cool liquids. From Fig. 4.4 we can see that fraction of LEFS polyhedra increases as non-affine displacement decreases.

In attempt to relating local structures to dynamic heterogeneity in super cool liquids or in the plastic rearrangements under applied shear many more local structural descriptors have been proposed, such as local energy, local density etc. A recent approach has been through machine learning [131, 132, 133, 134] where complex non linear feature vectors are generated starting from few local structural feature vectors such as bond-order parameters. In a recent paper by Richard et al. [33], authors have compared the performance of many of the proposed methods in the prediction of plasticity due to uniform shear deformation in $2d$ and they show that rearrangements are deeply encoded in the structure. The role of local structure in relation to plastic rearrangements has mostly been explored

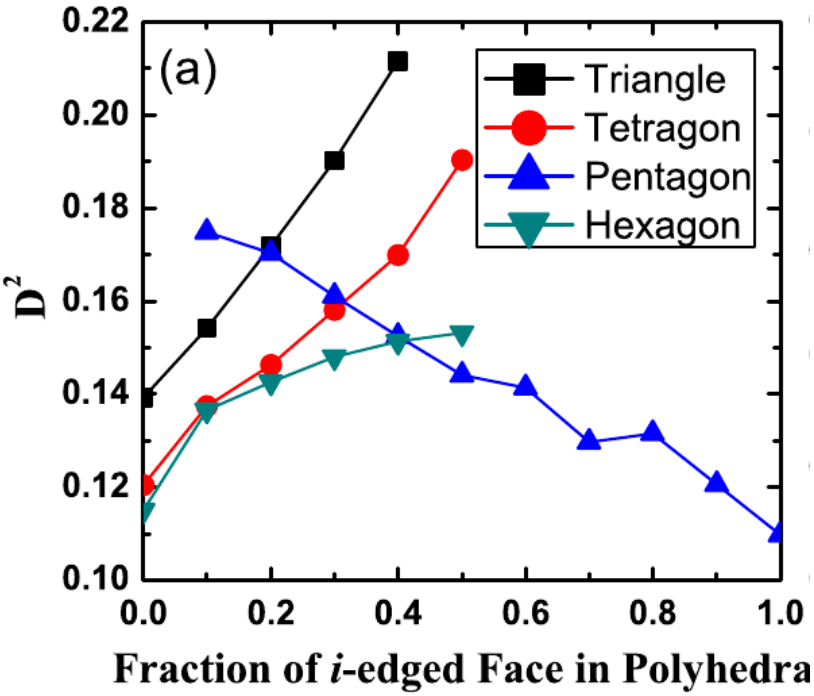

Figure 4.4: Correlation between i-edged faces and non-affine displacements $\mathrm{D}^2_{\mathrm{min}}$ [130].

for systems under uniform shear deformation. In this work we use a binary repulsive $3d$ glass former to explore the structural properties of particles undergoing plastic rearrangements due to cyclic shear deformation. We analyze local structural order of the system by computing the per particle two-body excess entropy S_2 [135] and tetrahedrality n_{tet} [3], the later has not been explored yet in the context of plastic rearrangements. These two are our structural descriptors of choice and their detail will follow in the next section. When a glass is deformed in quasi-static limit at zero temperature [136], compared to uniform shearing, the cyclic shear posses a sharp yielding transition from absorbing to diffusive state at strain amplitude γ_y [48]. With many cycles of deformation the system reaches a steady energy state. In steady state of strain amplitude $\gamma_{\mathrm{max}} < \gamma_y$ the plastic rearrangements during a deformation cycle is reversible[137] and localized. Above yielding the rearrangements with large particle displacements are irreversible and the plastic events correlate specially causing an avalanche and form shear band. We focus on analysing the configuration in steady state and if there is a priori structural difference in particles that will have largest and minimum rearrangements in next cycle.

4.2 Methods

4.2.1 System

We use 50:50 additive Repulsive Wahnström model at packing fraction $\phi = 0.58$ with size ratio $\sigma_{BB}/\sigma_{AA} = 1.2$, as has been described in Appendix. From equilibrated liquid system we obtain energy minimized inherent structures or

IS. We shear the IS in athermal quasi static limit for strain amplitudes $\gamma_{\max} \in [0.02, 0.09]$ for many cycles. The system yields above yielding amplitude $\gamma_y \approx 0.06$. Details of the simulations can be found in Appendix.

4.2.2 Local descriptor: Tetrahedrality

Below the onset temperature of glass transition the diffusivity of glass forming liquids decreases by several orders of magnitude as temperature is decreased. The mechanism involved in how a liquid looses its fluidity upon decreasing temperature or increasing density has been of prime interest for several decades now [7]. In general, along the extreme increase of relaxation time, dynamical heterogeneity appears, where locally some regions of the system have higher mobility compared to others within the time scale of alpha-relaxation. More and more evidence now support a correlation between this heterogeneity with changes in the local structure. One of the pioneer ideas in this regard was by Charles Frank in 1952 indicating the possible prevalence of icosahedral clusters in the glassy regime [138]. Later many studies corroborated the presence of local favored structures in the glassy regime related to the slowdown of dynamics, the spotlight being on the icosahedral clusters [139, 140, 141, 142]. In the same line of thought there has been proposals of simpler tetrahedron based order parameters capable of capturing the changes in local structure and dynamics [143, 144, 145, 146, 3]. In particular, a recent development was the introduction of the tetrahedrality of the local structure (TLS) n_{tet}, which measures the number of tetrahedral clusters each particle is involved in [3], based on the notion that most of the local favoured structures (including icosahedral) can be decomposed into tetrahedrons. It was found that the particles with higher values of n_{tet} are well correlated with slower dynamics as can be seen from Fig. 4.5.

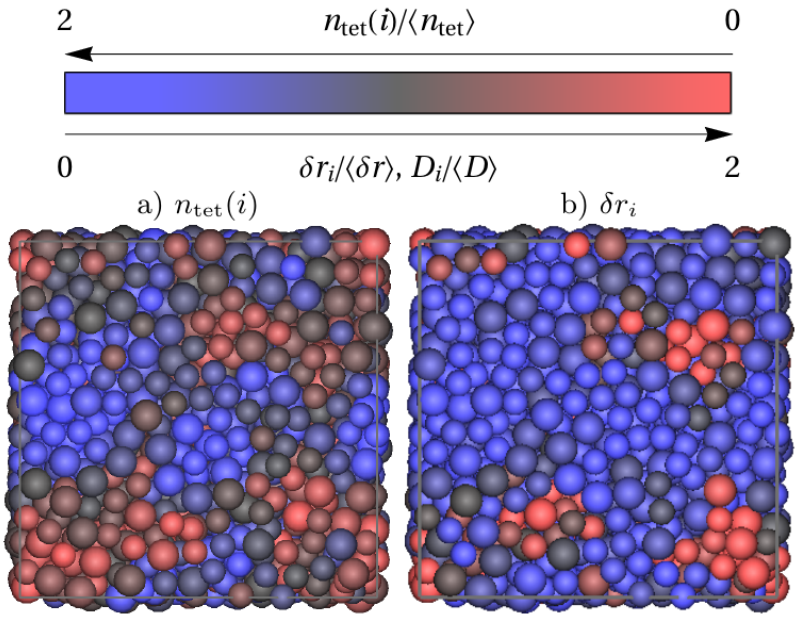

Figure 4.5: A snapshot of hard sphere system colour coded as per a) number of tetrahedra a particle is involved in and b) their absolute displacements over a time scale of 500τ [3].

For a given system, n_{tet} can be obtained from Topological Cluster Classification (TCC) [6] algorithm, which we shall discuss shortly. We have used this newly introduced structural order parameter n_{tet} in the context of plasticity.

4.2.3 Local descriptor: Two body excess entropy

The local favoured structures where the free energy is minimized has both energetic and entropic contribution. Gain in vibrational entropy with the loss of configurational entropy accounts for the local ordering [147]. Whereas energy driven ordering can be found in tetralhedral type liquids, entropy driven ordering can be found in hard sphere type systems. Entropy can be expanded in multiparticle correlations as $S = S_1 + S_2 + S_3 + ..$, here S_1 being the ideal gas limit, S_2 the two-body excess entropy which can be calculated from pair distribution function, S_3 for three-body interaction etc [135]. S_2 [148, 149, 150, 151] can be calculated from radial distribution function.

$$S_2 = -2\pi\rho k_B \int_0^\infty [g_m^i(r) log(g_m^i(r)) - g_m^i(r) + 1] r^2 dr, \tag{4.5}$$

where $g_m(r)$ corresponds to the mollified radial distribution function,

$$g_m(r) = \frac{1}{4\pi N\rho r^2} \sum_{i\neq j} \frac{1}{2\pi\sigma^2} \exp[-(r - r_{ij})^2/(2\sigma^2)]. \tag{4.6}$$

Here, r_{ij} is the distance between the i^{th} and j^{th} particle. The parameters are chosen such that $g_m(r) \sim g(r)$ and we have a smooth integral to compute S_2. To ensure the effectiveness of S_2 in identifying local structural fingerprint we are referring to some results in the paper [4],

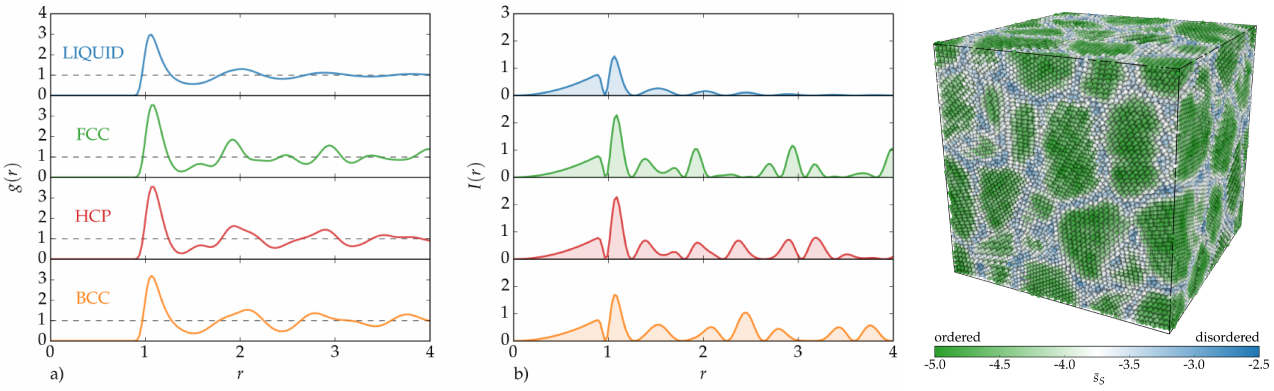

Figure 4.6: First two plots show the radial distribution function $g(r)$ and the integral of S_2 equation. 4.5 $I(r)$ for a Lennard Jones system in different structural phases. We can see, where as from $g(r)$ it is harder to make the difference between ordered and disordered liquid phase, from $I(r)$ it is more clear. In the right it is a colour plot of a snapshot of nanocrystalline Al at temperature $300K$ where atoms are coloured according to their S_2 values, locally averaged over some distance and denoted by $\bar{S}$ [4].

As can be seen from Fig. 4.6 S_2 is clearly capable of identifying ordered and disordered structures. However in this figure of the snapshot, a local averaged version of the per particle S_2 has been considered to smooth out high fluctuation.

For our WH system, we choose $\sigma = 0.09$ and for each particle the limit of the integration in equation 4.5 is from zero to $r_{max} = 5.0$. With this approach we obtain the per particle S_2. In particular, a more negative value of S_2 indicates higher local order.

S_2 [152, 150, 151] has been widely used in the context of transport coefficients and plasticity. S_2 measures the loss of entropy due to positional correlations, a lower value of S_2 corresponds to a more ordered structure. Even though S_2 is a half a century old concept there is place for new applications. As a matter of fact, in 2020, scaling relations have been reported of S_2 with diffusivity in glassy systems [148] and relaxation rates in cyclic sheared systems [149].

4.2.4 Topological Cluster Classification (TCC)

TCC algorithm helps to detect energy minimized clusters for a set of particles in isolation as has been explained in detail in the paper by Malins et al [6]. The idea of local favoured structures was initiated by Charles Frank as we have already mentioned, where he showed for 13 particles in isolation interacting through Lennard-Jones potential, icosahedral cluster arrangement requires 8.4% lower energy than more compact FCC or HCP crystal arrangement. TCC algorithm looks for clusters made up of total number of particles other than 13 as well, and with other interactions. For a given model system, TCC tries to identify clusters of m particles that has a similar bond network with that of the minimum energy cluster of that particular model.

The first job of the algorithm is to identify neighbours for a particle. For this, TCC uses a *modified* Voronoi tessellations method so that the results are robust against thermal fluctuations. Voronoi tessellations divides the space in non intersecting domains with distinctive boundaries. Each domain surrounds one particle and space points inside that domain is closest to this particle only. These domains are called Voronoi cells. In the modified version, two particles are called neighbours if their Voronoi cells share a face and the line connecting the particles intersect the shared face.

Once the neighbours have been identified, the algorithm looks for shortest path rings, known as *spm* rings, m denoting number of particles in the ring. The basic clusters are classified as *(i) spma* if it only got these m particles all bonded, *(ii) spmb* if there is a single extra particle which is neighbour to all m particles in the ring and *(iii) spmc* if there are two extra particles neighbour to all m particles in the ring. To give an example, $m = 3$ particles can form a triangular ring siting on the vertices of the ring. One extra particle can have bond to all these m particles and resulting as a *tetrahedron* cluster. In basic cluster, the usually sorted values of $m = 3, 4, 5$. More compound clusters

are found by either addition of particles to basic clusters or as a combination of basic clusters. There is standard nomenclature for naming the clusters. Fig. 4.7 shows the clusters that TCC identifies [153].

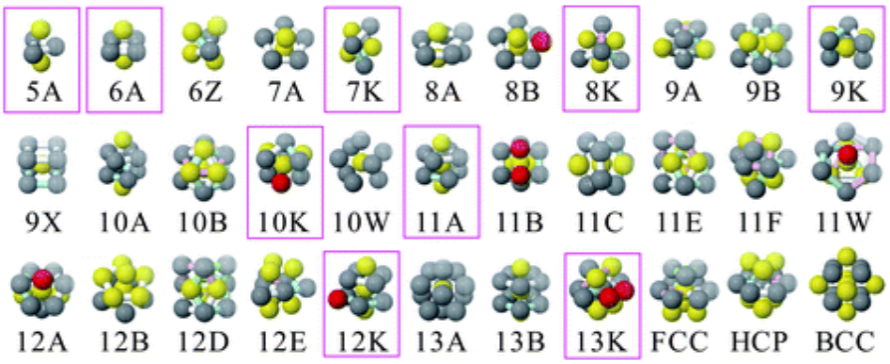

Figure 4.7: These are the clusters identified from TCC algorithm. The highlighted ones with pink squares are the minimum energy clusters for Kob-Andersen system [153]

4.3 Results

As we have discussed we have chosen tetrahedrality n_{tet} and local two body excess entropy S_2 to characterise local structural order. A higher value of n_{tet} and a lower negative value of S_2 accounts for higher ordered structure at local level. We arrange the results as follows: In next subsection, we first report (*i*) the variation of mean local ordering in liquid and inherent structures (IS) with temperature using the $\langle n_{\text{tet}} \rangle$ and $\langle S_2 \rangle$. (*ii*) We correlate the liquid structures and the corresponding IS at different temperatures. Afterwards in another subsection, we present the result from cyclic shear. We sample a high and a low temperature glass and shear the systems athermally for many deformation cycles with strain amplitudes γ_{max}. In steady states (*iii*) we compute the mean values of our structural order parameters as γ_{max} varies in a range across the yielding amplitude γ_y. (*iv*) From one cycle to the next we classify "mobile" and "static" particles with larger and smaller rearrangements respectively by computing the local non-affine displacement D^2_{min} [5]. (*v*) In terms of n_{tet} and S_2 we examine whether there is a difference between the mean local order of the mobile and static particles. (*vi*) Finally, we use the topological cluster classification algorithm (TCC) [6] to point out the different cluster association between the two classes.

4.3.1 Liquid and Inherent structures

We first sample equilibrated liquid configurations of WH system at different temperatures $T \in [0.7 - 2.0]$ and obtain zero temperature inherent structures (IS) from liquid through energy minimization. Our system size is $N = 64000$ and at packing fraction is $\phi = 0.58$. We compute per particle n_{tet} and S_2 for liquid and and IS at different temperatures and average over N particles to obtain $\langle S_2 \rangle$ and $\langle n_{\text{tet}} \rangle$.

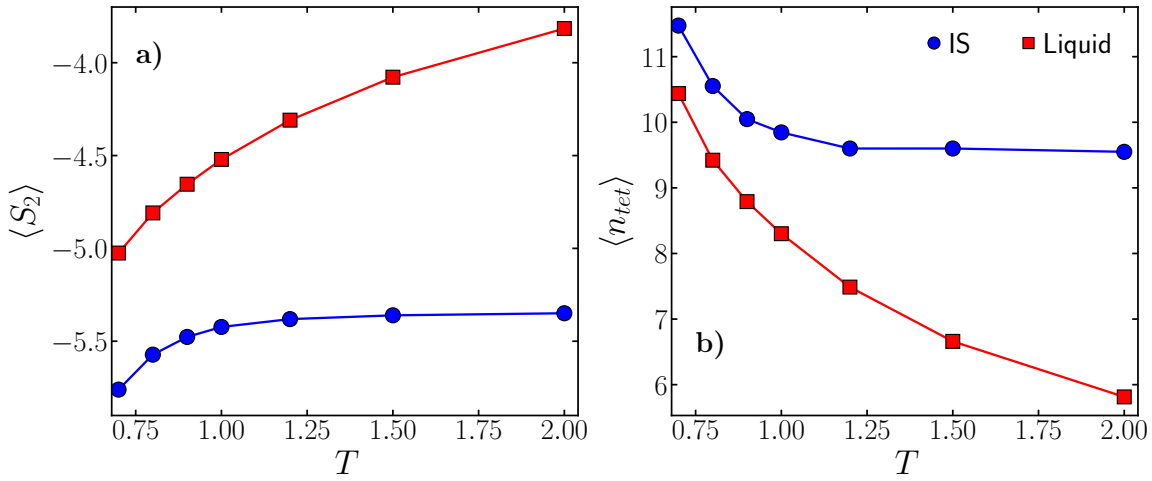

Figure 4.8: a) $\langle S_2 \rangle$ as a function of temperature T for liquid and inherent structure. b) n_{tet} as a function of T for liquid and inherent structure.

In Fig.4.8 we show the dependency of both structural quantities with temperature. In liquid, from high to low temperature the average local order increases as the systems present higher values of $\langle n_{\text{tet}} \rangle$ and lower of $\langle S_2 \rangle$. Higher local order is expected as has been reported earlier in the context of tetrahedrality in hard sphere mixtures [3]. However, for inherent structures (IS) the $\langle S_2 \rangle$ and $\langle n_{\text{tet}} \rangle$ is almost constant at higher temperatures. So, above the onset temperature of glass transition, the structural properties of the energy basin is almost similar and temperature independent. The values indicate higher local ordering in IS compared to liquid and this order increases for low temperatures. At lowest temperatures how close is the local ordering in a liquid versus in a IS? We compute Spearman's rank order correlation [154] between S_2 and n_{tet} values of N particles in Liquid and with their values in IS.

In Fig.4.9 a), we report this correlation as a function of temperature. We find that the correlation grows in lower temperatures and at $T = 0.7$ both S_2 and n_{tet} accounts for 60% correlated structure of supercooled liquid and its IS. Whereas at high temperature the correlation almost vanishes. This high correlation at lowest temperature is because the liquid system is already close to its local energy minimum and therefore posses similar level of local ordering which is also associated to slow down in dynamics.

4.3.2 Sheared inherent structures

By this point, we have established that our structural descriptors are able to capture the growth of local order in super cool regime. Now we will investigate the system under cyclic shear deformation using n_{tet} and S_2. In particular, as we shear the glass (IS) with strain amplitude γ_{max} there are two regimes of interest.

I. Below yielding $\gamma_{max} < \gamma_y$: For low amplitudes of shear below yielding, there is annealing in the system. By annealing we mean that in steady state the system reaches lower energy minimum basins, or the average energy

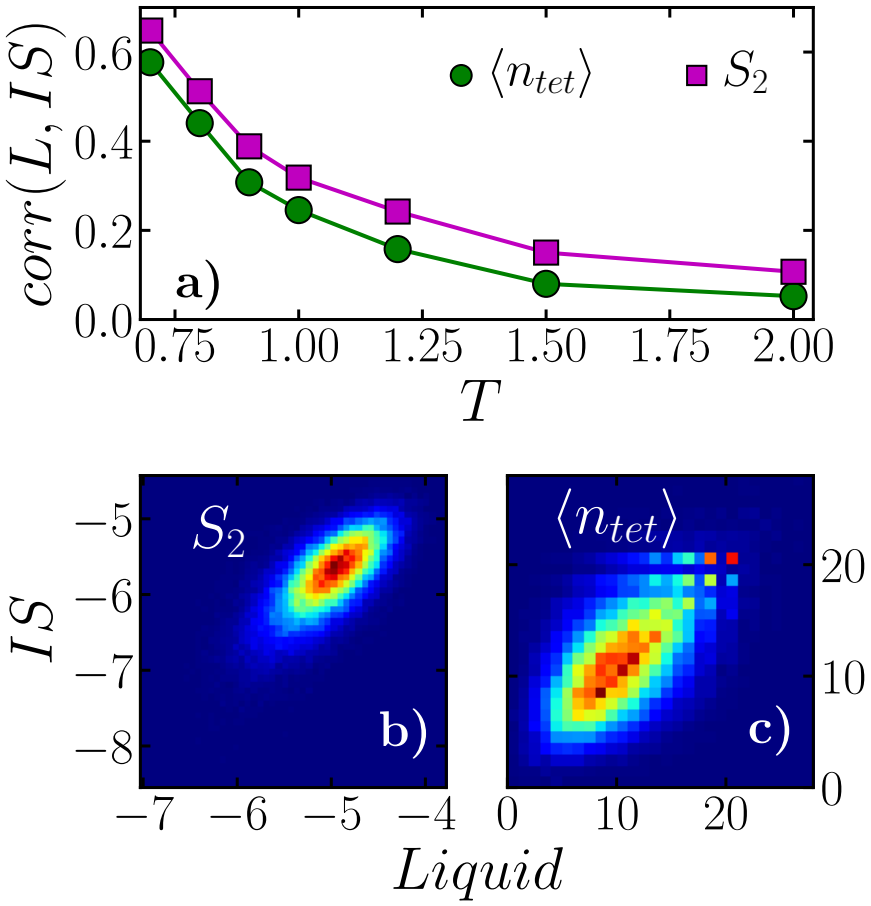

Figure 4.9: a) Spearman's correlation between the structural descriptors of liquid and inherent structures as a function of temperature T. Density plot between inherent structure and liquid of b) S_2 and c) n_{tet} at a temperature $T = 0.7$.

of the system decreases. In our system from $\gamma_{max} = 0.02$ to $\gamma_{max} = 0.06$ we have more and more annealed absorbing states. If the initial configuration is a high temperature liquid, the annealing effect is more pronounced, compared to low temperature initial configuration [155]. Also, in steady state, during a cycle of deformation, all the local plastic rearrangements are reversible in nature. Therefore, from one cycle to another, there is no appreciable net displacement. Even though we are calling the rearrangements during a cycle of deformation as "reversible", the trajectory of a particular particle will not follow the same path as we move forward with strain value $\gamma = 0 \rightarrow \gamma_{\text{max}}$ and backward $\gamma = \gamma_{\text{max}} \rightarrow 0$, for example. This is a peculiarity about cyclic loading in absorbing states that even without following the same path, at the end of a cycle the particles manage to come back to the positions they began with. However depending on the system, mechanism of loading and deformation amplitude, sometimes this reversibility has higher periodicity, meaning it may take more than one cycle, typically $2-4$ for the particles to come back to their positions [156].

II. Above yielding $\gamma_{max} > \gamma_y$: For higher strain amplitude above yielding, the system becomes diffusive. Plastic

rearrangements during a cycle in steady energy state are now irreversible in nature, particles fail to come back to their initial positions at the end of a cycle. For a large enough system, like in our case, $N = 64000$, it is possible to observe formation of shear band [49, 157]. In this case, one part of the system consisting a band of particles parallel to either YZ or XY plane in case of XZ shear, have higher net displacements from n^{th} to $(n+1)^{th}$ cycle, than the particles outside of this shear band (SB), as can be seen from Fig. 4.10. Particles inside the SB has random motions. The more mobile shear band has lower local density, higher local energy [1].

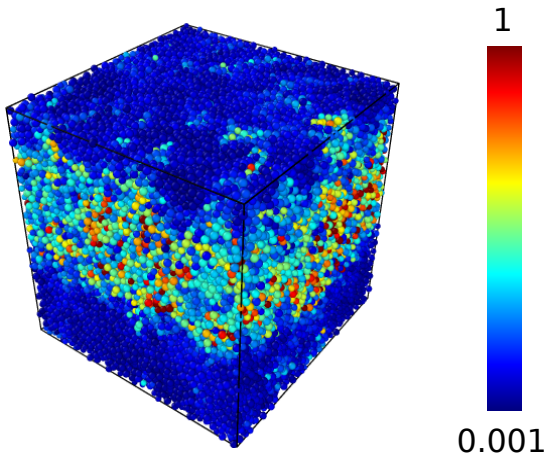

Figure 4.10: Shear band in WH system at $T = 0.7$, $\gamma_{\max} = 0.08$. Colour code shows displacements of particles between two consecutive cycles of deformation.

Now we investigate the local order in the system below and above yielding.

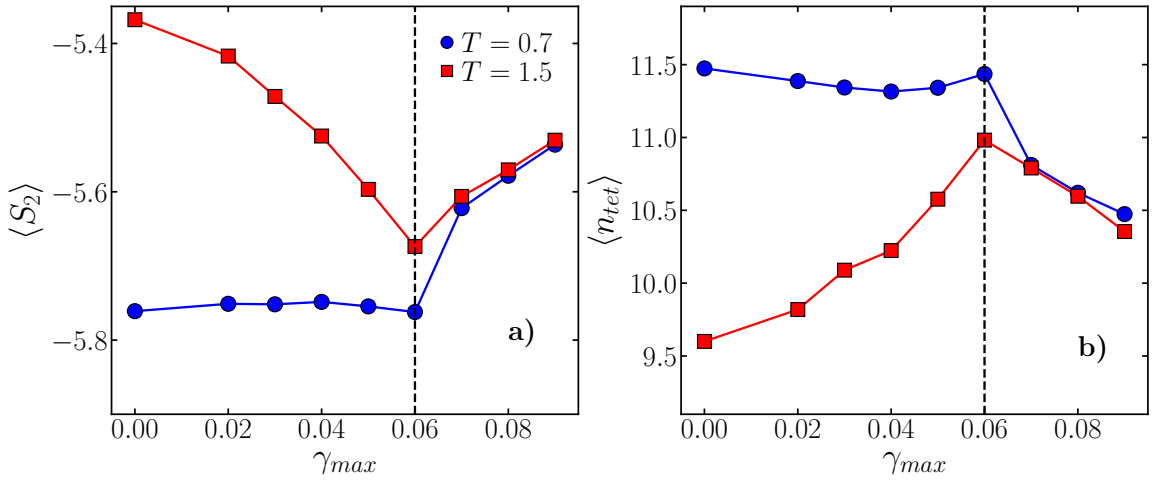

Figure 4.11: From initial equilibrated liquids at temperatures $T = 1.5$ and $T = 0.7$ we obtain the IS and shear the IS with different shear amplitudes γ_{max}. Values of a) $\langle S_2 \rangle$ and b) $\langle n_{\text{tet}} \rangle$ are plotted against γ_{max} in steady state. vertical dashed curve shows the yielding amplitude γ_y.

First we compute $\langle S_2 \rangle$ and $\langle n_{\text{tet}} \rangle$ in steady state of strain amplitudes $\gamma_{max} \in [0.02, 0.09]$ across $\gamma_y \sim 0.06$. In Fig.4.11, we report the variation of mean value of these local descriptors with γ_{max}, for both temperatures $T = 1.5$ and $T = 0.7$. Note that, $\gamma_{max} = 0.0$ is actually the value for the IS. For the high temperature glass, with annealing in the range of $\gamma_{max} \in [0.0, 0.06]$ the average local order increases as reflected by lower $\langle S_2 \rangle$ and higher $\langle n_{\text{tet}} \rangle$. As we cross γ_y in diffusive state on the average local order decreases. The transition across γ_y is sharp. For $T = 0.7$, with no strong annealing, $\langle S_2 \rangle$ and $\langle n_{\text{tet}} \rangle$ is almost constant and upon crossing γ_y jumps to the same level of $T = 1.5$. Above yielding, energy also shows similar trend, that is they jump to the same level irrespective of initial temperature [49], this jump in energy has been shown in Appendix in Fig. A.4.

As we have discussed, above yielding, we can observe shear band formation. The question is now whether $\langle S_2 \rangle$ and $\langle n_{\text{tet}} \rangle$ capture differences in structures inside and outside the shear band. In Fig.4.12, for the case of $T = 0.7$, $\gamma_{max} = 0.08$ we bin the system along the Z axis (perpendicular to the plane of shear band), and we plot the mean square displacement (MSD) between n^{th} and $(n+1)^{th}$ cycle of the particles located inside each bin [1]. We can clearly see the position of the mobile shear band where the MSD takes larger values. We turn our attention to the local structure, we compute the $\langle S_2 \rangle$ and $\langle n_{\text{tet}} \rangle$ per bin along Z, shown in 4.12 b) and c) respectively. Both of them capture a variation across shear band. This indicates that the system is structurally different inside and outside SB. On the average, outside SB we get higher structural order.

Now we will focus on the main objective of this work, seeing local structural differences related to plastic rearrangements in steady state. We use non-affine displacement $\mathrm{D}^2_{\text{min}}$ to identify particles with larger rearrangements, as was introduced by Falk and Langer [5] and we have discussed in the introduction in Equation 4.1. Here we are rewriting the same equation in slightly simpler form even though for the calculation we followed Equation 4.1. In simpler form,

$$D^2_{min} = \frac{1}{n} \sum_n [(r_j(t) - r_i(t)) - \Gamma(r_j(0) - r_i(0))]^2 \tag{4.7}$$

Here, $r_{i,j}(0)$ is the position of the particles at the beginning of a deformation cycle and $r_{i,j}(t)$ is their positions in deformed box at time t. The sense of time here is equivalent to the number of deformation steps taken to complete a cycle using AQS protocol (see Appendix). The sum in equation 4.7 is over nearest neighbors within a cut off $r_{cut} = 1.4\sigma_{AB}$, which corresponds to the first minimum of $g(r)$ of the full system. In our case of cyclic deformation, for the amplitudes below yielding, at steady state if we consider configurations at $t = 0$ and $t = 4\gamma_{max}/d\gamma$ (at the end of the cycle), we shall have $D^2_{min} \approx 0$ due to reversibility. However, we are interested in identifying which particles went through maximum re-arrangements during the deformation cycle, irrespective of reversibility. Therefore, we recorded the maximum value $max(D^2_{min})$ for each particle in a cycle of deformation.

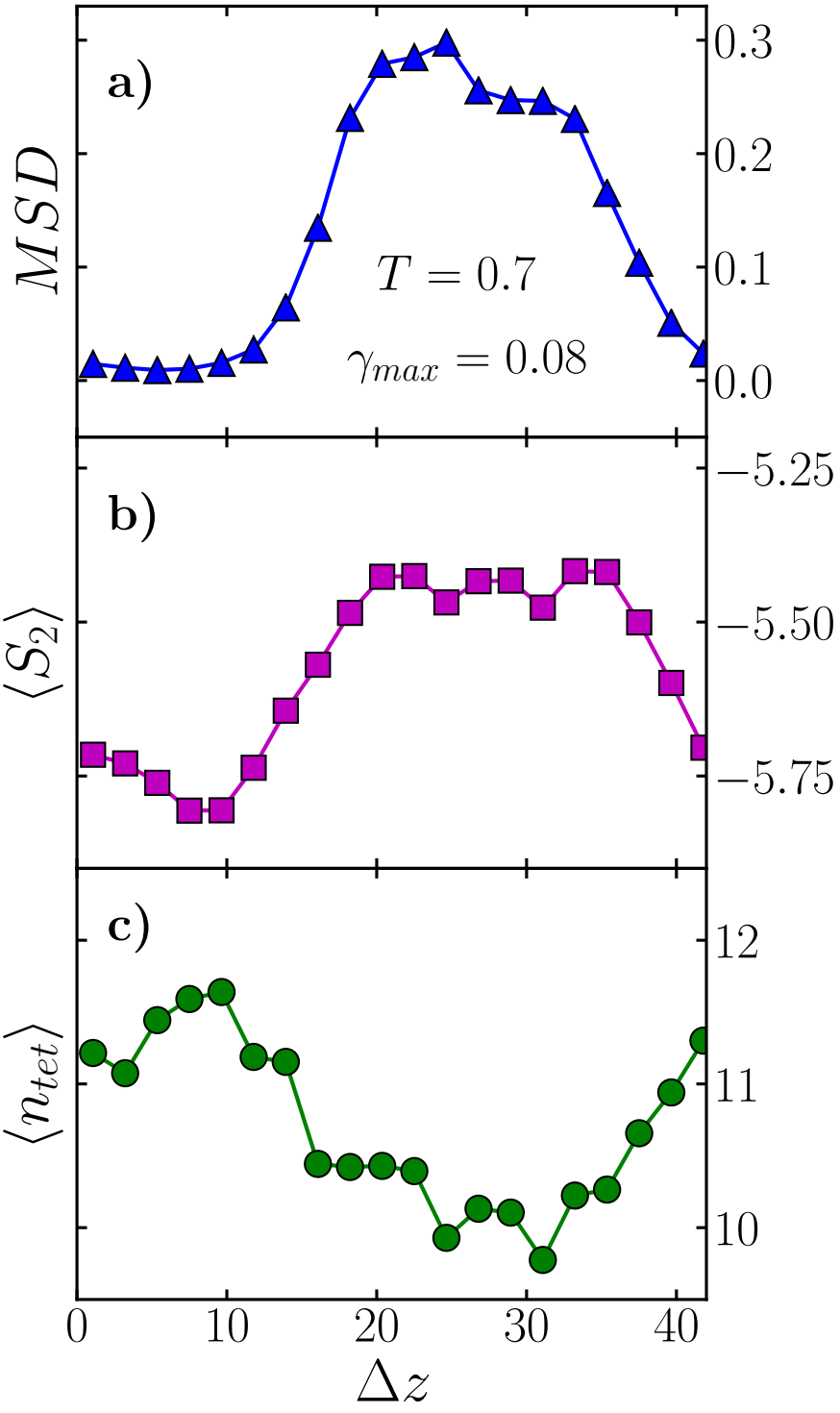

Figure 4.12: We choose a sheared system at strain amplitude $\gamma_{max} = 0.08$ above yielding for IS initially prepared at temperature $T = 0.7$. Shear band is captured by (a) the mean-squared displacement between two consecutive cycles along Z (perpendicular to the shear plane). We also plot b) $\langle S_2 \rangle$ and c) $\langle n_{\rm tet} \rangle$ binned along z in steady state of the same system.

In Fig.4.13, we plot the distribution of $max(D^2_{min})$ for two strain amplitudes below and above yielding. Above yielding,

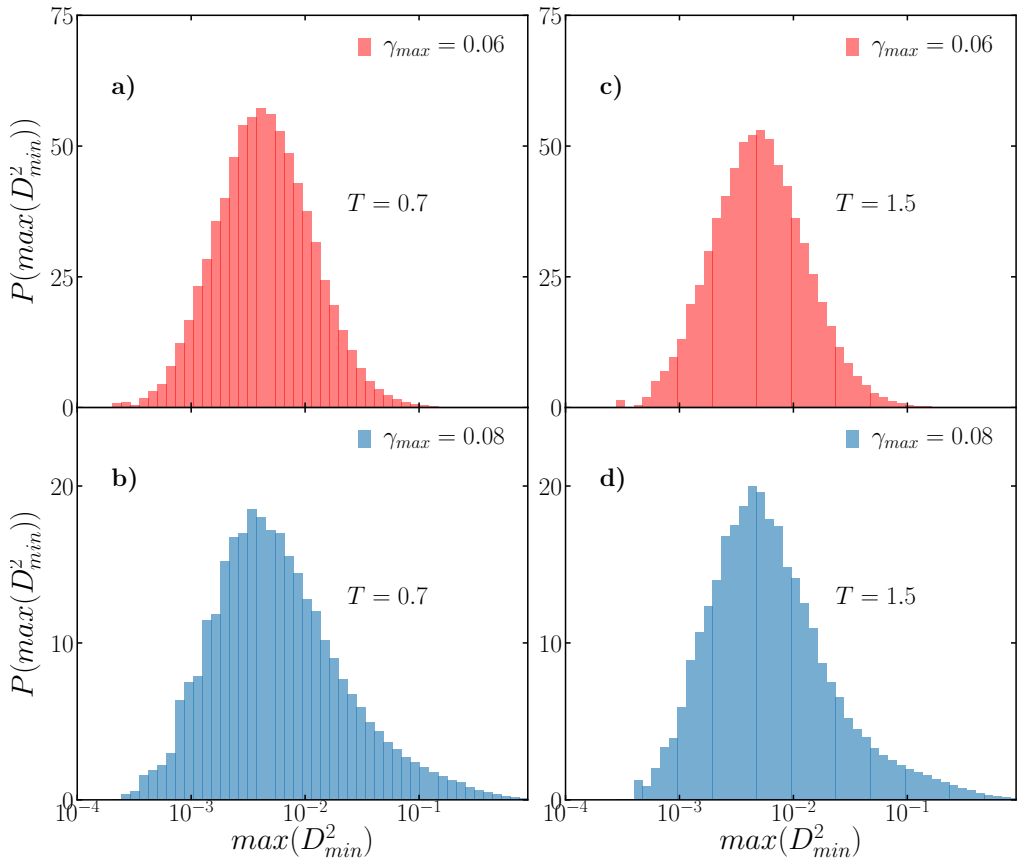

Figure 4.13: For initial configuration at $T = 0.7$, distribution of $max(D^2_{min})$ at steady state of shear amplitude $\gamma_{max} = 0.06 < \gamma_y$ in a) and of $\gamma_{max} = 0.08 > \gamma_y$ in b). Above yielding we have longer tail. We observe the same behaviour for the case of $T = 1.5$ as well in c) and d).

due to shear band, we have long tail in the distribution with higher displacement values.

Calculation of $max(D^2_{min})$ has enabled us to identify particles with higher displacements, owing to plastic rearrangements. At this stage we ask, was there any structural discrepancy among particles that went through higher rearrangements versus the particles that were reluctant to move? In other words, after the end of a cycle, *(i)* particles with highest $max(D^2_{min})$ values and *(ii)* particles with lowest $max(D^2_{min})$: Did they have different structures at the beginning of a cycle?

To answer this question, we use our local structural descriptors S_2 and n_{tet}. In the steady state, we note the per particle values of the descriptors. Thereafter we subject the system to a complete deformation cycle and note the values of $max(D^2_{min})$ per particle. We classify the particles as 'static' or 'mobile' if their $max(D^2_{min})$ values are among the smallest or the largest respectively. In particular, we choose the top 5% as mobile particles and bottom 5% for the static ones, and we plot their distribution in Fig.4.14. We are hereby reporting the case of $T = 0.7$ and $\gamma_{max} = 0.06$, however the trend is similar in all the cases of our system. From $P(S_2)$, we see that static and mobile particles have different $\langle S_2 \rangle$. Static particles have lower $\langle S_2 \rangle$ or higher order, compared to the mobile particles. The same trend we find in n_{tet} as well, static particles having higher tetrahedrality n_{tet}. Interestingly, there is a strong abundance of

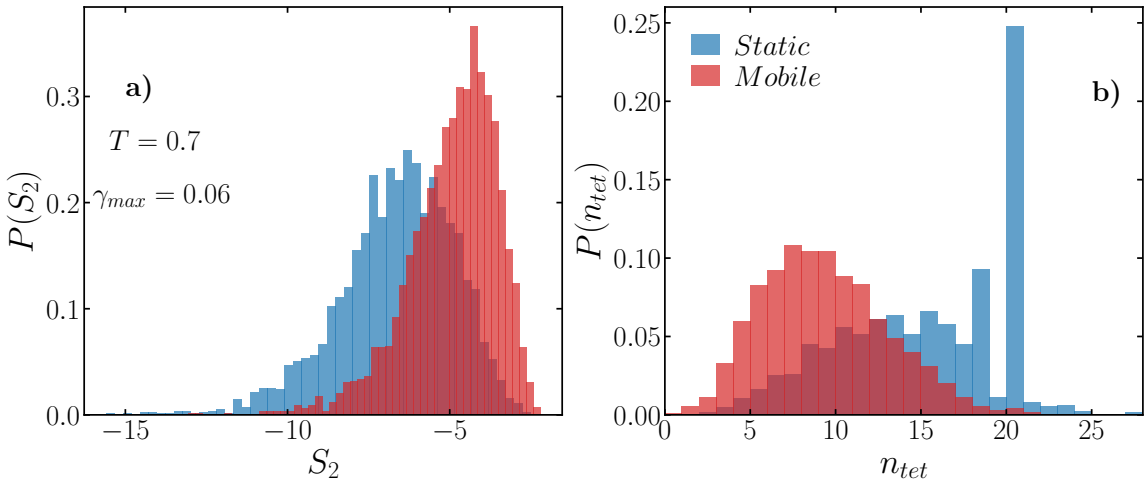

Figure 4.14: For the case of $T = 0.7$ in steady state of $\gamma_{max} = 0.06$, distribution of S_2 in a) and n_{tet} in b) at the beginning of a cycle, for particles with lowest (blue) and highest (red) values of displacements $max(D^2_{min})$ at the end of a cycle.

$n_{\text{tet}} = 20$ in static particles. This value of n_{tet} is equal to a particle sitting at the center of an icosahedral cluster, the appearance of this cluster has been investigated in many occasions in supercooled liquid systems, in connection to dynamic heterogeneity.

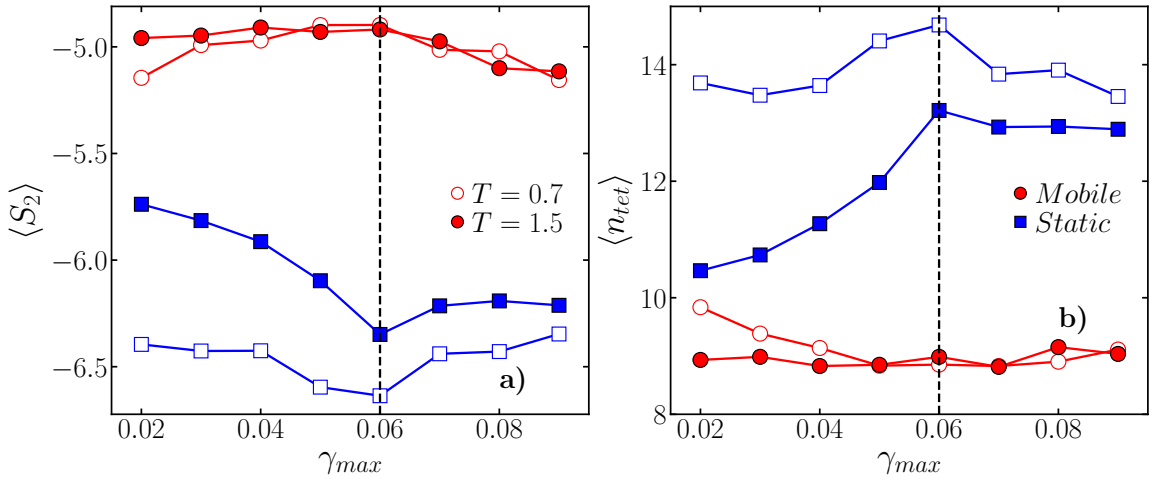

Figure 4.15: $\langle S_2 \rangle$ in a) and $\langle n_{\text{tet}} \rangle$ in b) as a function of γ_{max} in steady state, for 5% most mobile (red circle) and 5% static particles (blue squares) based on their $max(D^2_{min})$ values. Filled symbols correspond to $T = 1.5$ and open symbols for $T = 0.7$.

In Fig.4.15 we plot $\langle S_2 \rangle$ and $\langle n_{\text{tet}} \rangle$ for static and mobile particles as a function of strain amplitude γ_{max} and for both high ($T = 1.5$) and low ($T = 0.7$) temperatures. *(i)* For static particles in the range of $\gamma_{\text{max}} \in [0.0, 0.06]$, the n_{tet} increases and $\langle S_2 \rangle$ decreases. This is more strongly observed for $T = 1.5$ and is related to the fact of increase in ordered structure at local level with annealing, as we observed in Fig.4.11 as well. Above yielding, the static particles belong to the regime outside shear band. We find that upon crossing the yielding amplitude (> 0.06), both $\langle S_2 \rangle$ and $\langle n_{\text{tet}} \rangle$ flattens out. *(ii)* Now coming to the mobile particles, below yielding, they are the particles that

undergo reversible plastic re-arrangements, while above yielding, they belong to the mobile shear band regime with irreversible displacements. From $\langle S_2 \rangle$ and $\langle n_{\text{tet}} \rangle$ we do not see appreciable change in values upon crossing yielding amplitude. However, consistently mobile particles have lower $\langle n_{\text{tet}} \rangle$ and higher $\langle S_2 \rangle$ at the beginning of the cycle.

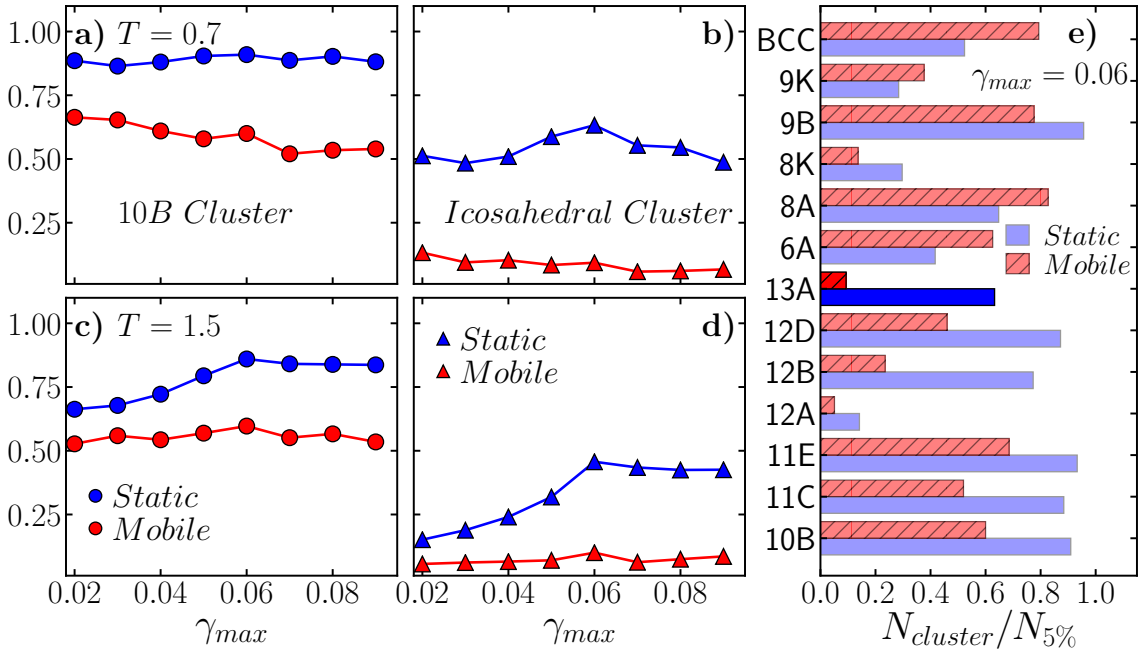

Figure 4.16: We perform TCC analysis for mobile (red) and static (blue) particles during a deformation cycle in steady state. In e) for $T = 0.7$ and $\gamma_{max} = 0.06$ we report the fraction of these mobile and static particles in a particular type of cluster. $13A$ is the icosahedral cluster. Next we plot these fractions against γ_{max} for two particular classes $10B$ (a and c) and $13A$ (b and d) and two initial; temperatures $T = 0.7$(a and b) and $T = 1.5$ (c and d).

At this point we have established that the particles with larger rearrangements and particles unwilling to move have different local environment on the average, as reflect by our local descriptors. Now we investigate the exact local arrangement of these classes by making use of the Topological Cluster Classification (TCC) [6]. From the TCC analysis we can establish the membership of each particle to some predefined clusters. Note that, each particle can be part of different types of clusters simultaneously. For the 5% most mobile and most static particles we examine all possible clusters computed by the TCC and we calculate the fraction of particles involved in a certain cluster for each case. In Fig.4.16 e) we show the results for mobile (red) and static (blue) particles for the case of $T = 0.7$ and $\gamma_{max} = 0.06$. Here, we report only the clusters that show significant differences between the two communities. We highlight the $13A$ cluster corresponding to an icosahedral cluster, where we see that the difference between mobile and static is maximum. Another cluster that presents large differences between the two communities is the $10B$ cluster which corresponds to a defective icosahedral cluster.

Now, we explore the structure for all γ_{max} and the two temperatures $T = 0.7$ and $T = 1.5$, and we focus in the changes of icosahedral and defective icosahedral clusters. In Fig. 4.16 (a-d), we show the fraction of particles involved in the $10B$ and $13A$ cluster for each of the communities as a function of γ_{max}. For $T = 1.5$ the static particles

again show growth in their involvement into these clusters with annealing in the range $\gamma_{\max} \in [0.0, 0.06]$ and then above yielding it flattens out. For mobile particles we do not see significant difference. These trends are consistent with the variation of $\langle S_2 \rangle$ and $\langle n_{\text{tet}} \rangle$ in Fig.4.15.

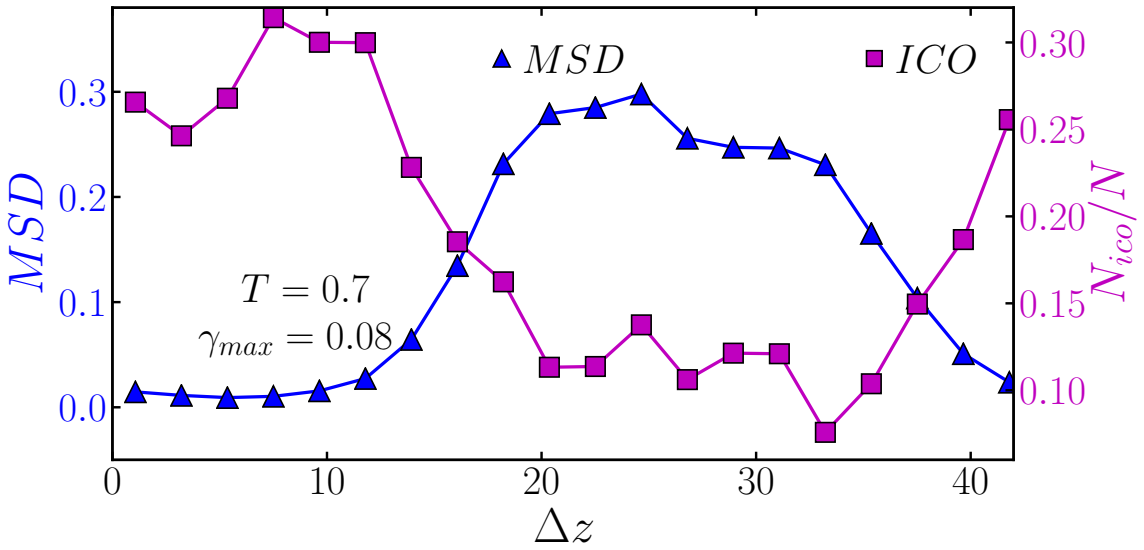

Figure 4.17: For the case of $T = 0.7$ and $\gamma_{max} = 0.08$ in steady state we plot mean square displacement of the particles along Z (blue triangles, capturing the location of shear band. We also plot fraction of particles involved in icosahedral cluster along Z.

From Fig.4.14 b) we see that the majority of the most static particles have $n_{tet} = 20$. This number is interesting because as we mentioned earlier, icosahedral arrangement can be decomposed into 20 tetrahedra. From Fig. 4.16 we again see that the most mobile and the least mobile particles on the average show significant difference regarding to the icosahedral ordering. We know that above yielding, the particles with larger arrangements belong to the localized shear band, therefore we ask whether there is a specific localization of icosahedral clusters above yielding. In Fig. 4.17, we report one case, namely $T = 0.7$, $\gamma_{max} = 0.08$. First we plot the msd between two consecutive cycles along Z (perpendicular to the plane of shear band). As before, this shows us the location of shear band. Now, we consider all particles in the system, bin them along Z and plot in each bin, what fraction of the particles are involved in icosahedral cluster. We find a clear localization, 30% of the particles outside shear band has this icosahedral involvement, where as inside shear band it is negligible. Interestingly we can draw a connection to this finding in case of soft jammed sphere packings where it was observed that icosahedrally packed regions are coupled with flow inhomogeneities, they are locally stiffer [158, 159]. As, we have also found that the non-moving sub-volume of our system is correlated with the higher presence of icosahedral clusters.

4.4 Conclusions

In this work we have connected the local structural information with the plastic rearrangements in steady state of cyclic shear in a model glass system. To address this connection we have chosen local two body excess entropy S_2 and tetrahedrality in local structure n_{tet}. In general a higher n_{tet} value and a lower S_2 value for a particle indicates that the particle is associated with its neighbours in a more ordered local arrangement. We have shown that both n_{tet} and S_2 reveals higher structural order in liquid and inherent structures in lower temperatures. This is consistent with the findings of increase in local order as the liquid starts showing extreme dynamical slow down below the onset of glass transition temperature. We also find that there is a high correlation of structural order in liquid and IS at lowest temperature, in this case $T = 0.7$. Thereafter, we choose two glasses, one prepared at high temperature and one at low and shear the system with certain strain amplitudes γ_{max} in athermal limit for many deformation cycles. We find that below the yielding strain amplitude $\gamma_y \approx 0.06$, shearing induces higher structural order in the system as the system anneals. In the steady states corresponding to $\gamma_{\text{max}} < \gamma_y$ during a deformation cycle particles rearrange but at the end of the cycle it comes back to initial positions, known as "reversible" plastic events. Whereas above yielding the rearrangements are irreversible in nature. We identify the particles going through maximum and minimum rearrangements by computing their non-affine displacements during a cycle w.r.t. the configuration at the beginning of a cycle in steady state. We label them as "mobile" and "static". When we compare their local structures at the beginning of a cycle we see that mobile and static particles have different mean local order. Explicitly, mobile particles have lower $\langle n_{\text{tet}} \rangle$ and higher $\langle S_2 \rangle$. However for mobile particles we do not find a difference in mean local ordering below and above γ_y, which can be a very interesting problem to look at using other descriptors or machine learning in future. We have also analyzed the system with topological cluster classification (TCC) algorithm. Analysis shows structural differences in fast and slow particles on the average. The most interesting finding was that we find above yielding in the subsystem outside shear band has 30% association with icosahedral cluster whereas inside SB it is negligible. This result encompasses the connection of local structure with flow inhomogeneity under shear as has been recently examined in other systems [160, 158].

Chapter 5

Conclusions and discussions

The thesis investigates structural properties of glass forming binary models under cyclic shear deformation in athermal limit. There are two facets of this investigation. Firstly, long-range structural order given by hyperuniformity is probed across yielding transition. Secondly, changes in local structure is analyzed across the yielding transition also during deformation cycles in steady states of cyclic shear.

The glass forming models chosen in this work are well explored Kob-Andersen Lennard Jones system (KALJ) and repulsive Wahnström mixture (WH). They represent metallic glasses [161] which are of immense importance of industrial use. Cyclic shear is an well used technique to test mechanical properties of materials [162, 47, 163], memory effects [164, 165], self organization [166], annealing of glass [51]. When a glass is deformed in quasi-static limit at zero temperature [136], compared to uniform shearing, the cyclic shear posses a sharp yielding transition from absorbing to diffusive state at strain amplitude γ_y [48]. With many cycles of deformation the system reaches a steady energy state. In steady state of strain amplitude $\gamma_{max} < \gamma_y$ the plastic rearrangements during a deformation cycle are reversible [137] and localized. Above yielding the rearrangements with large particle displacements are irreversible and the plastic events correlate spatially causing an avalanche and form shear band [1].

Hyperuniformity means suppression of density fluctuations at large length scales. Hyperuniform states of matter are considered to be new exotic states of amorphous materials with wide scope of use since it can suppress fluctuations at large length scales but is isotropic at shorter length scales like a liquid with no Bragg peak [2]. In sheared active state models such as Manna model, in sheared suspensions the absorbing states were found to be hyperuniform in nature [74, 78, 116, 167]. Our works show that even before shearing, the the compressibility of the inherent structures of the high temperature and high density glass forming liquid is effectively hyperuniform. When the system is sheared, in the steady states of strain amplitudes γ_{max} below yielding the system continues being hyperuniform suppressing number density variance. Above yielding amplitude $\gamma_{max} > \gamma_y$ in presence of shear band there is high density fluctuation in the system. But surprisingly we find that inside the shear band and far from shear band the structure is still hyperuniform and it is the interface between these two phases that enhances overall density

fluctuation. So, in the directions parallel to shear band plane the system is hyperuniform, in the vertical direction hyperuniformity is disrupted. Such directional hyperuniformity means that the system is compressible along one direction whereas in opposite direction in has higher compressibility. This can lead to interesting applications as indicated by Torquato [168].

In supercooled regime many glass forming liquids show an abundance of locally favoured structures which are correlated with dynamic heterogeneity. Local favoured structures can be energy driven or entropy driven. For example in Lennard Jones systems icosahedral clusters are energetically favoured which can be further decomposed into tetrahedral clusters [138]. Marin et al [3] defined tetrahedrality n_{tet} which measures per particle association to total number of tetrahedral clusters and it was reported that for hard sphere system higher value of n_{tet} highly correlates to slower moving regions in glassy regime. We have shown in this thesis that average n_{tet} in WH system increases in lower temperature equilibrated liquid and corresponding IS. This shows higher local order at lower temperatures which is also reflected in the decrease of local two-body excess entropy S_2. We also find average local order increases with annealing in the absorbing states as we cyclically deform the system. In steady state, we tracked the particle displacements during deformation cycle. Our results reveal that particles with larger displacements on the average have lower structural order. Here we would like to stress that connecting local structural order to plastic rearrangements have not been explored in the context of periodic shear. We expect use of machine learning techniques will be able to distinguish between rearrangements below and above yielding [169, 131, 134]. Our results also demonstrate distinct characteristics of local structures inside and outside of shear band.

In this thesis the glass forming models we worked on are of "repulsive" type, as for both of them the decay of intermediate scattering function at low temperatures shows a plateau corresponding to beta relaxation. This plateau can be interpreted as if particles are trapped by the cages formed by their neighbours. However there is another class of "attractive" colloidal glass formers where the interaction between the particles can be modeled as a hard-core repulsion (for length scale $0 < r < \sigma$) plus a very short range attraction (for length scale $\sigma < r <\approx 1.03\sigma$) [170, 171]. In such models the slow down in the dynamics in glass transition regime is dictated by particle-particle bond formation due to attraction part of the interaction. Interestingly, under periodic shear they show a two-step yielding [172]. First, at lower strains the inter-particle bonds break even though the topology of the neighbours does not change. Second, at a higher strain values finally due to stronger rearrangements the topology changes and the system flows. As a future direction of research it will be very interesting to investigate if the two-step yielding can be associated with the structural changes in attractive colloidal glass. We would like to conclude by opening a question common to both of the above works. Comparing the plots of Fig. 3.11 and Fig. 4.8 we observe that inherent structures are less hyperuniform at lowest temperatures, depicting loss of long range order, whereas local order grows at lowest temperatures. This seems puzzling since commonly one would expect that local ordering will enhance correlation. It will be interesting to examine if the non-homogeneous nature of the structure in low temperature inherent structure prohibits long range hyperuniformity.

Appendix A

Numerical preparation of glass system

Computer simulations are employed to study glass systems at the atomic level, it is an alternative to laboratory experiments to extract information about the underlying thermodynamics as well as structural properties [173]. Specially more often we are interested in qualitative behaviour of materials which can be compared to experimental counter parts with proper tuning. The two most popular technique to simulate a glass forming liquid is the Monte Carlo (MC) method and the Molecular Dynamics (MD) method.

In MC the statistical randomness of a physical configuration space, i.e. a set of coordinates for N particles, is exploited to end up with an *accepted* configuration. Starting from a random initial configuration, a new random configuration is generated and compared with the initial. If the new configuration has lower energy, it is accepted. Otherwise, the Boltzman factor $\exp(-\frac{\Delta U}{k_B T})$ is computed and compared with a random number generator in the range of $0-1$. If the random number is less than the calculated Boltzman factor, the new configuration is accepted. The idea here is that particles eventually evolve to lower energetic states and even though a move to a higher energy state is possible, it is less probable.

In MD the idea is to track time evolution of a system of particles starting out with initial positions and momenta by solving the deterministic Newton's equation of motion. One of the advantage over MC is obviously that we can compute time dependent quantities. In this thesis , the MD simulation has been used to generate equilibrated liquid samples.

A.1 Molecular Dynamics

A.1.1 Steps

Typical steps in a MD simulation involve:

- Initialize the system : Choose a set of initial positions and make sure particles DO NOT overlap. Randomly

assign velocities. Velocities are chosen according to desired temperature, as it is related to the kinetic energy of the system.

- Given a form of potential energy $V(\mathbf{r})$, Calculate forces acting on the particles:

$$\mathbf{F}(\mathbf{r}) = -\frac{dV(\mathbf{r})}{d\mathbf{r}} \tag{A.1}$$

- Solve for the equation of motion for each particle i,

$$\mathbf{F}_i = m_i \mathbf{a}_i \tag{A.2}$$

$\mathbf{a}_i$ being the acceleration acting on the particle of mass m_i. Now,

$$\mathbf{a}_i = \frac{d^2\mathbf{r}_i}{dt^2} \tag{A.3}$$

So we have to solve this second order differential equation for each particle.

- Updating position and velocity: Most commonly used algorithm to solve the above equation is the Leapfrog Verlet algorithm. If the time step chosen is Δt,

$$\mathbf{v}_i(t+\frac{\Delta t}{2}) = \mathbf{v}_i(t-\frac{\Delta t}{2}) + \mathbf{a}_i(t)\Delta t \tag{A.4}$$

$$\mathbf{r}_i(t+\Delta t) = \mathbf{r}_i(t) + \mathbf{v}_i(t+\frac{\Delta t}{2})\Delta t \tag{A.5}$$

- Calculate the updated force and repeat the update steps.

A.1.2 Periodic Boundary Condition (PBC)

MD is applied to system sizes with total number of particles N of the order of hundreds or thousands. Practically the system sizes are small and surface effect would dominate the outcomes. This is handled by implementation of PBC. If N particles are in a domain of volume V, referred as the *primary* cell, it is imagined that this sell is surrounded by exact replicas of itself, known as *image* cells. We need to solve for the interactions and follow the trajectories of the particles contained in primary cell only. In course of time, if a particle moves to an image cell, image from opposite cell moves into the primary.

A.1.3 Initialization

Initialization involves assignment of initial positions, velocities and if needed system specific some higher order derivatives of positions. Initial velocities are randomly assigned with the constrained $< \frac{p_x^2}{2m} >= \frac{1}{2}k_BT$, for each degrees of freedom. Velocities are drawn from random distribution to ensure the temperature and then adjusted such that there is no overall momentum, $\sum m_i \mathbf{v}_i = 0$. In equilibrium MD simulation, some important parameters are total number of particles N, volume V, energy E, temperature T, pressure P. For example, to simulate a liquid at a particular density we shall have different box sizes with different N.

A.1.4 Thermostat

For constant temperature thermodynamics, we need to attach a heat bath with the system. In other words, we need to keep adjusting the velocities to achieve a target temperature. Commonly used algorithms are Berendsen and Nosé–Hoover thermostat. In our simulation, we have used the later.

Nosé–Hoover thermostat

In this algorithm an additional fictitious degree η of freedom is introduced whose function is similar to that of friction. In $3d$, the equation of motion is now,

$$m_i \frac{d^2\mathbf{r}_i}{dt^2} = \mathbf{F}_i - \eta m_i \mathbf{v}_i \tag{A.6}$$

$$\frac{d\eta(t)}{dt} = \frac{1}{Q}\left[\sum m_i \mathbf{v}_i^2 - \frac{3N+1}{2}k_BT\right] \tag{A.7}$$

Here Q determines the relaxation dynamics of the friction.

A.1.5 How to know if system has equilibrated?

As we keep integrating the equations of motion in MD simulation with some small time step dt, it may take hundreds or thousands of steps to relax from its initial configuration. Therefore, it is important to monitor thermodynamic quantities as a function of time. For example, in NVT simulation, one may keep track of the temperature , energy and as the system equilibrates they reach to constant values with small fluctuations.

A.2 Interaction potentials and Models used in thesis

In general for non-bonded systems, the interaction potential will have the following form,

$$V(\mathbf{r}^N) = \sum_i u(\mathbf{r}_i) + \sum_{i<j} v(\mathbf{r}_i, \mathbf{r}_j) + ... \tag{A.8}$$

. The first term accounts for external force field, the second for two-body interaction and then there are higher order terms. For most of the situations contribution from higher ordered terms are not significant and at most one can come up with *effective* two-body interaction. In absence of external field the simplest approach is to define a pair potential $V(r) = v(r_{ij})$. For a pair of neutral atoms there are two limits of force field: A Van Der Walls type attraction for longer range and a repulsive force at shortest distance due to overlapping electron orbitals and Pauli repulsion. Historically among the pair potentials, the most popular choice has been the Lennard Jones (LJ) potential with its wide application in noble gasses, liquids, glass forming models.

$$V(r) = 4\varepsilon\left[(\frac{\sigma}{r})^{12} - (\frac{\sigma}{r})^{6}\right] \tag{A.9}$$

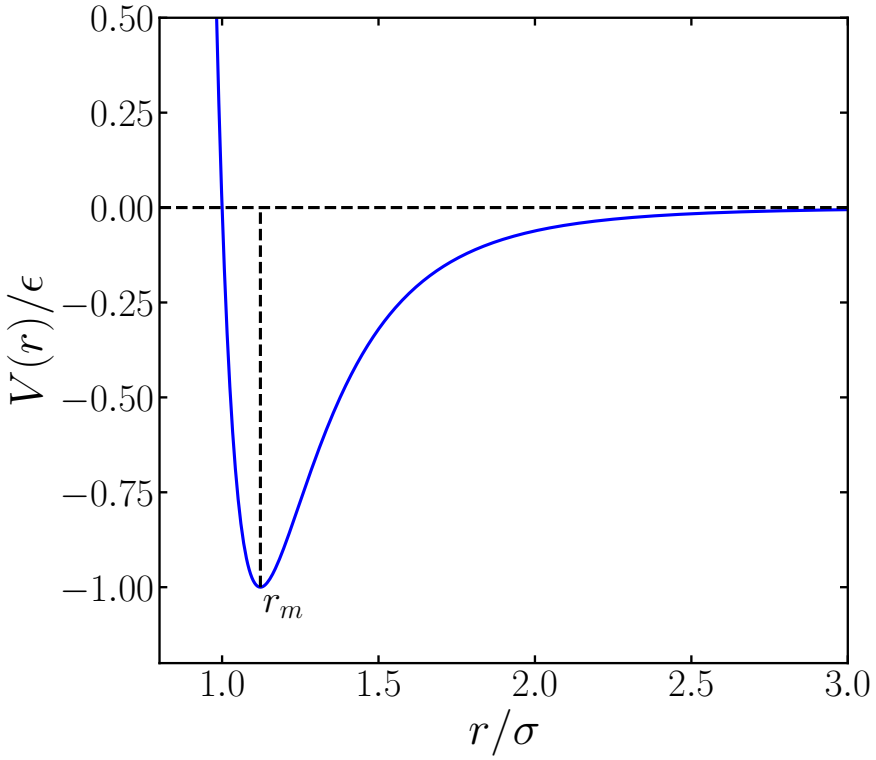

Figure A.1: Lennard Jones potential

Here r is the distance between the particles, ε is the depth of the potential and σ is the distance where the

potential is zero. σ denotes the size of the atomic molecules as for $r < \sigma$, the potential is positive and soon becomes infinitely large due to the repulsive $\left(\frac{\sigma}{r}\right)^{12}$ term. Usually in simulation a cut-off distance r_c is defined beyond which particles do not interact with each other. Also at this cut-off the potential and the force should vanish to have smooth integrability.

Apart from the interaction potential the polydispersity, i.e. particles with different sizes, of the system has been an essential tool to avoid crytalization of the sample and get a glassy behaviour. Of course the simpler form is to choose binary mixtures. Two such well established model systems are, **Wahnström** model [174] and **Kob-Andersen** model [175]. They are very good representative metallic alloy type of glasses [176].

A.2.1 Kob Andersen Lennard Jones Model

Kob Andersen model is a mixture of 80% larger atoms A and 20% smaller sized atoms B. they interact with Lennard Jones potential. But, we have introduced an additional square term in the potential so that at cutoff distance the potential smoothly goes to zero, meaning the force is also zero at r_c.

$$V_{\alpha\beta}(r) = 4\varepsilon_{\alpha\beta}\left[\left(\frac{\sigma_{\alpha\beta}}{r}\right)^{12} - \left(\frac{\sigma_{\alpha\beta}}{r}\right)^{6}\right] + 4\varepsilon_{\alpha\beta}\left[c_{0\alpha\beta} + c_{2\alpha\beta}\left(\frac{r}{r_{c\alpha\beta}}\right)^{2}\right], r_{\alpha\beta} < r_{c\alpha\beta} \tag{A.10}$$

The parameters $c_{0\alpha\beta}$ and $c_{2\alpha\beta}$ are chosen such that at a cutoff distance $r_{c\alpha\beta}$, both the pair potential and the force smoothly go to zero. Here α and β represents particle types A and B. Interaction parameters are expressed with respect to those corresponding to type A: $\sigma_{BB}/\sigma_{AA} = 0.88$, $\sigma_{AB}/\sigma_{AA} = 0.80$, $\varepsilon_{BB}/\varepsilon_{AA} = 0.5$, $\varepsilon_{AB}/\varepsilon_{AA} = 1.5$ and cutoff distance $r_{c\alpha\beta} = 2.5\sigma_{\alpha\beta}$.

A.2.2 Repulsive Wahnström model

As a model glass system, we have explored the behavior of the Wahnström (WH) system [174]. It consists of a $50:50$ mixture of additive particles interacting through only with the repulsive part of the Lennard-Jones (LJ) potential,

$$V_{\alpha\beta}(r) = \begin{cases} 4\varepsilon_{\alpha\beta}\left[\left(\frac{\sigma_{\alpha\beta}}{r}\right)^{12} - \left(\frac{\sigma_{\alpha\beta}}{r}\right)^{6}\right] - V_{r_c}, & r < r_c \\ 0, & r \geq r_c \end{cases} \tag{A.11}$$

where α and β denote the type of particle (A or B), the cut-off distance is defined as $r_c = 2^{\frac{1}{6}}\sigma_{\alpha\beta}$ which is the minima of LJ equation A.9. So at this point, the first derivative of the potential is essentially zero. V_{r_c} is the value of the LJ potential evaluated at r_c. Note that, with this only the repulsive interaction between two particles is retained. The potential parameters are defined with respect to type A: $\sigma_{BB}/\sigma_{AA} = 1.2$, $\sigma_{AB}/\sigma_{AA} = 1.1$ and $\varepsilon_{AA} = \varepsilon_{BB} = \varepsilon_{AB} = 1.0$.

A.3 Simulation parameters

We use LAMMPS package [177] to perform molecular dynamics simulation of the system. We choose a time step size of $dt = 0.005$. For most part of the thesis for both the models we have worked on a system size $N = 64000$. For Kob-Andersen model, we worked with a high density system at $\rho = 1.2$. For Wahnström model we have worked with packing fraction $\phi = \frac{\pi}{6V}(N_A\sigma_{AA}^3 + N_B\sigma_{BB}^3) = 0.58$.

Initially, we prepare equilibrated liquid samples at temperature T with the Nosé-Hoover thermostat (NVT) for time steps of the order of 2×10^5 (high T) - 2×10^6 (low T) depending on temperature and model, followed by constant energy (NVE) relaxation. We sample the configurations from equilibrated liquid with an interval where density density correlation from previous recorded sample has dropped to zero. We can observe dynamical slow down by computing this self part of the density density correlation with time. For example here we are reporting the self part of intermediate scattering function for Wahnström model,

$$F_s(k,t) = \frac{1}{N}\Big\langle \sum_{i=1}^{N} \exp i\mathbf{k}\cdot(\mathbf{r}_i(t) - \mathbf{r}_i(0))\Big\rangle \tag{A.12}$$

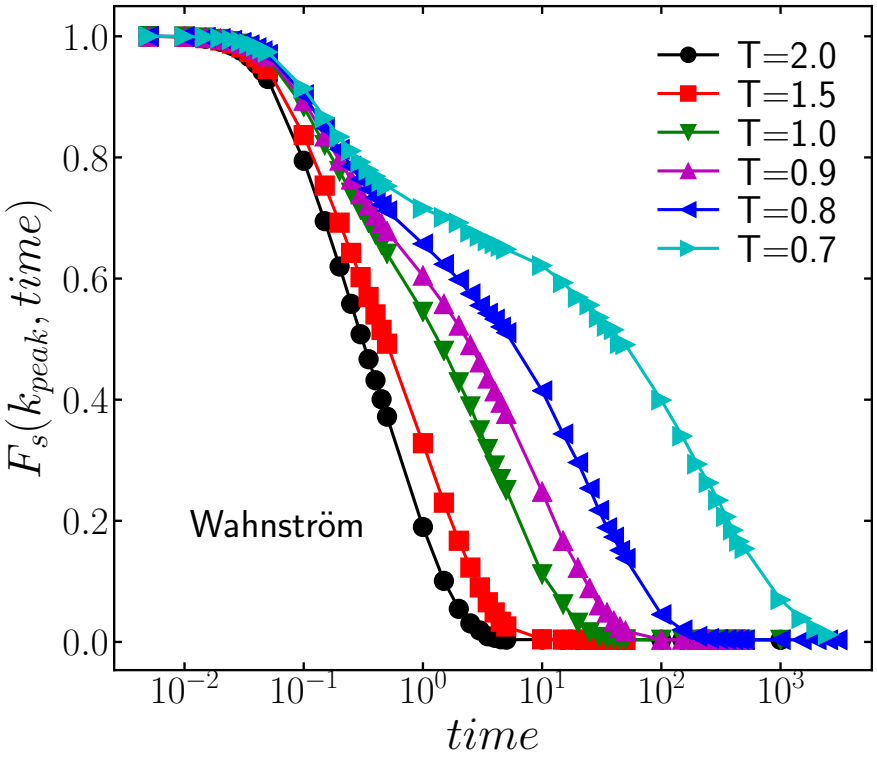

Figure A.2: Intermediate scattering function corresponding the wave vector where first peak of structure factor appears

In Fig.A.2, we plot $F_s(k,t)$ for first peak k_{peak} of structure factor $S(k)$. This basically gives the time scale for the

decay of density correlation at the level of first cell. We can see that for lower temperature the decay is slower due t glassy dynamics. The plateau appearing for lower temperatures are related to the cage effect.

A.4 Oscillatory shear deformation using AQS protocol

In this thesis we have studied the structural properties of model glass system under cyclic shear deformation. For that, we have used Athermal Quasi Static (AQS) protocol of shear deformation [178, 136]. The inspiration of this protocol is the energy landscape description of super cooled liquid or atomic glasses. A N particle system interacting through some potential has a very complicated energy landscape and the dynamics of the system can be thought of diffusion between the rugged energy surface. In AQS we track the evolution of inherent structures under applied shear. One AQS step is composed of two steps:

- Deformation of simulation box by applying homogeneous shear transformation of the coordinates with some small strain increment $d\gamma$.
- Minimization of energy at zero temperature so that the system moves the current local minimum induced only because of the shear step.

The idea here is that the system in absence of external bias prefers to sit in the local energy minimum. When the system is sheared, typically it will escape the local minimum. This can be caused from thermal agitation for a system at finite temperature and finite shear rate. However, In the limit of vanishing shear rate $\dot{\gamma} \to 0$ and $T \to 0$, escape from the minima is primarily due to strain increment. When a series of AQS steps are repeated the total accumulated strain $\gamma_{acc} = \sum d\gamma$ increases and stress strain curves show clear reversible smooth branches separated by sudden drops corresponding to plastic rearrangements. Along the reversible branch what happens is that due to the deformation of simulation box, the landscape around the minima changes gradually until at some point the minima vanishes and the system has to evolve to a new minima.

AQS is a very useful technique with the use of advanced energy minimizers to computationally study mechanical response under shear in the low temperature, low shear rate and thermodynamic limit. There are many minimizers available on LAMMPS like steepest descent (sd) , **conjugate gradient (cg)**, fire etc. We have used CG algorithm as the minimizer which has been used in many papers.

A.5 Cyclic shear parameters

We have used athermal quasi static shear (AQS) protocol to study yielding under cyclic shear of the glasses. For that, at zero temperature the XZ plane of the simulation box is deformed in very small shear steps of strain value

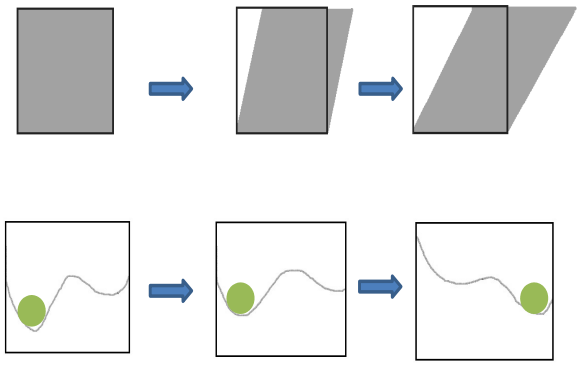

Figure A.3: Schematic diagram of evolution of potential energy landscape with deformation of simulation box. In AQS, the box is deformed with small steps of $d\gamma$ followed by energy minimization. With large deformation, system jumps to new energy minimum.

$d\gamma = 0.0002$. The coordinate transformation is,

$$\begin{bmatrix} 1 & 0 & d\gamma \\ 0 & 1 & 0 \\ 0 & 0 & 1 \end{bmatrix} \begin{bmatrix} x \\ y \\ z \end{bmatrix} \tag{A.13}$$

Each step is followed by energy minimization using CG. For deformed unit cell always Lees-Edwards boundary condition is implemented.

Lees-Edwards boundary condition pseudo code:

For two particles i and j the minimum image convention for Lees-Edwards can be summarized as follows,

$$
\begin{aligned}
&dx = x[i] - x[j] \\
&dy = y[i] - y[j] \\
&dz = z[i] - z[j] \\
&If(dz < L_z/2) : \{dz+ = L_z; dx+ = tilt_{xz}; dy+ = tilt_{yz}\} \\
&If(dz > L_z/2) : \{dz- = L_z; dx- = tilt_{xz}; dy- = tilt_{yz}\} \\
&If(dy < L_y/2) : \{dy+ = L_y; dx+ = tilt_{xy}\} \\
&If(dy > L_y/2) : \{dy- = L_y; dx- = tilt_{xy}\} \\
&If(dx < L_x/2) : \{dx+ = L_x\} \\
&If(dx > L_x/2) : \{dx- = L_x\}
\end{aligned}
$$

Here, $L_{x,y,z}$ is the box size of the unit cell. For XZ shear, $tilt_{xz} = \gamma L_z$ and $tilt_{yz} = tilt_{xy} = 0$. These steps of small strain increments continue until the strain γ attains the value γ_{max} along one direction. Then, the deformation steps are repeated in the opposite direction. Thus, one complete deformation cycle consists of strains following the sequence,

$$0 \to \gamma_{max} \to 0 \to -\gamma_{max} \to 0. \tag{A.14}$$

AQS deformation corresponding to different shear amplitudes γ_{max} are performed for many cycles, in the range of $50 - 500$ typically, depending on the amplitude of shear and the system, so that the system reaches steady states where the energies fluctuate around a fixed mean value as can be seen in Fig. A.4. Configurations at steady states are stroboscopically (at zero strain at the end of each cycle) sampled for further analysis.

In Fig. A.4 we plot energy of IS initially obtained from equilibrated liquids at two different temperatures for the Wahnström mixture with deformation cycle. We can identify pre-yield and post-yield strain amplitudes γ_{max}. Note that for $\gamma_{max} \in [0.02, 0.06]$, the energy of the IS is different for the two temperatures. Above yielding amplitude $\gamma_y \approx 0.06$ the energy increases and irrespective of their preparation history they now fluctuate around a mean value.

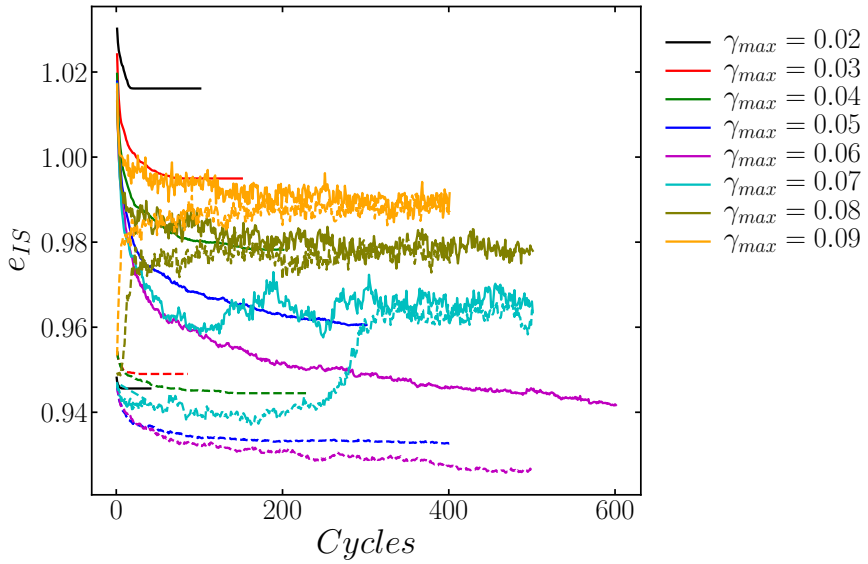

Figure A.4: For Wahnström mixture, energy of inherent structure e_{IS} with deformation cycle. The solid curves correspond to initial temperature $T = 1.5$ and broken curves are for $T = 0.7$. Above yielding ($\gamma_{max} > 0.06$) the energy fluctuates around a same value irrespective of initial temperature.

Bibliography

[1] Anshul DS Parmar, Saurabh Kumar, and Srikanth Sastry. “Strain localization above the yielding point in cyclically deformed glasses”. In: *Physical Review X* 9.2 (2019), p. 021018.

[2] Salvatore Torquato. “Hyperuniform states of matter”. In: *Physics Reports* 745 (2018), pp. 1–95.

[3] Susana Marın-Aguilar et al. “Tetrahedrality Dictates Dynamics in Hard Sphere Mixtures”. In: *Physical Review Letters* 124.20 (2020), p. 208005.

[4] Pablo M Piaggi and Michele Parrinello. “Entropy based fingerprint for local crystalline order”. In: *The Journal of chemical physics* 147.11 (2017), p. 114112.

[5] Michael L Falk and James S Langer. “Dynamics of viscoplastic deformation in amorphous solids”. In: *Physical Review E* 57.6 (1998), p. 7192.

[6] Alex Malins et al. “Identification of structure in condensed matter with the topological cluster classification”. In: *The Journal of chemical physics* 139.23 (2013), p. 234506.

[7] Ludovic Berthier and Giulio Biroli. “Theoretical perspective on the glass transition and amorphous materials”. In: *Reviews of Modern Physics* 83.2 (2011), p. 587.

[8] James S Langer. “Theories of glass formation and the glass transition”. In: *Reports on Progress in Physics* 77.4 (2014), p. 042501.

[9] Yoshiaki Sugimoto et al. “Chemical identification of individual surface atoms by atomic force microscopy”. In: *Nature* 446.7131 (2007), pp. 64–67.

[10] *KOPP Glass: ebook*. https://www.koppglass.com/blog/mechanical-properties-glass-design-survive-stress-impact-and-abrasion.

[11] Franz Faupel et al. “Diffusion in metallic glasses and supercooled melts”. In: *Reviews of modern physics* 75.1 (2003), p. 237.

[12] Gregory B McKenna. “Physical aging in glasses and composites”. In: *Long-term durability of polymeric matrix composites*. Springer, 2012, pp. 237–309.

[13] Charles Austen Angell. “Structural instability and relaxation in liquid and glassy phases near the fragile liquid limit”. In: *Journal of non-crystalline solids* 102.1-3 (1988), pp. 205–221.

[14] Heinz Bässler. “Viscous flow in supercooled liquids analyzed in terms of transport theory for random media with energetic disorder”. In: *Physical review letters* 58.8 (1987), p. 767.

[15] Pablo G Debenedetti and Frank H Stillinger. “Supercooled liquids and the glass transition”. In: *Nature* 410.6825 (2001), pp. 259–267.

[16] Jürgen Horbach and Walter Kob. “Relaxation dynamics of a viscous silica melt: The intermediate scattering functions”. In: *Physical Review E* 64.4 (2001), p. 041503.

[17] B Doliwa and Andreas Heuer. “Cage effect, local anisotropies, and dynamic heterogeneities at the glass transition: A computer study of hard spheres”. In: *Physical review letters* 80.22 (1998), p. 4915.

[18] Liesbeth Janssen. “Mode-coupling theory of the glass transition: A primer”. In: *Frontiers in Physics* 6 (2018), p. 97.

[19] Valeriy V Ginzburg. “A simple mean-field model of glassy dynamics and glass transition”. In: *Soft matter* 16.3 (2020), pp. 810–825.

[20] Michio Tokuyama. “Mean-field theory of glass transitions”. In: *Physica A: Statistical Mechanics and its Applications* 364 (2006), pp. 23–62.

[21] Frank H Stillinger. “A topographic view of supercooled liquids and glass formation”. In: *Science* 267.5206 (1995), pp. 1935–1939.

[22] Francesco Sciortino. “Potential energy landscape description of supercooled liquids and glasses”. In: *Journal of Statistical Mechanics: Theory and Experiment* 2005.05 (2005), P05015.

[23] Eric I Corwin, Heinrich M Jaeger, and Sidney R Nagel. “Structural signature of jamming in granular media”. In: *Nature* 435.7045 (2005), pp. 1075–1078.

[24] Dapeng Bi et al. “Jamming by shear”. In: *Nature* 480.7377 (2011), pp. 355–358.

[25] Aleksandar Donev et al. “Jamming in hard sphere and disk packings”. In: *Journal of applied physics* 95.3 (2004), pp. 989–999.

[26] Silke Henkes, Yaouen Fily, and M Cristina Marchetti. “Active jamming: Self-propelled soft particles at high density”. In: *Physical Review E* 84.4 (2011), p. 040301.

[27] Andrea J Liu and Sidney R Nagel. “Jamming is not just cool any more”. In: *Nature* 396.6706 (1998), pp. 21–22.

[28] Swadhin Kumar Patel et al. “Metallic Glasses: A Revolution in Material Science”. In: *Metallic Glasses*. IntechOpen, 2020.

[29] *Application of metallic glasses*. https://www.indiastudychannel.com/resources/135533-Metallic-glasses-Types-Applications.aspx.

[30] Alexandre Nicolas et al. “Deformation and flow of amorphous solids: Insights from elastoplastic models”. In: *Reviews of Modern Physics* 90.4 (2018), p. 045006.

[31] Baran Sarac and Jan Schroers. “Designing tensile ductility in metallic glasses”. In: *Nature communications* 4.1 (2013), pp. 1–7.

[32] Dongchan Jang and Julia R Greer. “Transition from a strong-yet-brittle to a stronger-and-ductile state by size reduction of metallic glasses”. In: *Nature materials* 9.3 (2010), pp. 215–219.

[33] D Richard et al. “Predicting plasticity in disordered solids from structural indicators”. In: *Physical Review Materials* 4.11 (2020), p. 113609.

[34] Todd C Hufnagel, Christopher A Schuh, and Michael L Falk. “Deformation of metallic glasses: Recent developments in theory, simulations, and experiments”. In: *Acta Materialia* 109 (2016), pp. 375–393.

[35] Fathollah Varnik et al. “Shear localization in a model glass”. In: *Physical review letters* 90.9 (2003), p. 095702.

[36] CC Hays, CP Kim, and William L Johnson. “Microstructure controlled shear band pattern formation and enhanced plasticity of bulk metallic glasses containing in situ formed ductile phase dendrite dispersions”. In: *Physical Review Letters* 84.13 (2000), p. 2901.

[37] Yunfeng Shi. “Size-independent shear band formation in amorphous nanowires made from simulated casting”. In: *Applied Physics Letters* 96.12 (2010), p. 121909.

[38] LF Liu et al. “Behavior of multiple shear bands in Zr-based bulk metallic glass”. In: *Materials Chemistry and Physics* 93.1 (2005), pp. 174–177.

[39] AL Greer, YQ Cheng, and E Ma. “Shear bands in metallic glasses”. In: *Materials Science and Engineering: R: Reports* 74.4 (2013), pp. 71–132.

[40] Futoshi Shimizu, Shigenobu Ogata, and Ju Li. “Yield point of metallic glass”. In: *Acta materialia* 54.16 (2006), pp. 4293–4298.

[41] Gaurav Prakash Shrivastav, Pinaki Chaudhuri, and Jürgen Horbach. “Yielding of glass under shear: A directed percolation transition precedes shear-band formation”. In: *Physical Review E* 94.4 (2016), p. 042605.

[42] R Maaß et al. “A single shear band in a metallic glass: Local core and wide soft zone”. In: *Applied Physics Letters* 105.17 (2014), p. 171902.

[43] ML Falk, JS Langer, and L Pechenik. “Thermal effects in the shear-transformation-zone theory of amorphous plasticity: comparisons to metallic glass data”. In: *Physical Review E* 70.1 (2004), p. 011507.

[44] Vitalij Schmidt et al. “Quantitative measurement of density in a shear band of metallic glass monitored along its propagation direction”. In: *Physical review letters* 115.3 (2015), p. 035501.

[45] Wei-Ting Yeh et al. “Glass stability changes the nature of yielding under oscillatory shear”. In: *Physical review letters* 124.22 (2020), p. 225502.

[46] Minh Triet Dang et al. “Reversibility and hysteresis of the sharp yielding transition of a colloidal glass under oscillatory shear”. In: *The European Physical Journal E* 39.4 (2016), pp. 1–11.

[47] N Koumakis, JF Brady, and G Petekidis. “Complex oscillatory yielding of model hard-sphere glasses”. In: *Physical review letters* 110.17 (2013), p. 178301.

[48] Premkumar Leishangthem, Anshul DS Parmar, and Srikanth Sastry. “The yielding transition in amorphous solids under oscillatory shear deformation”. In: *Nature communications* 8 (2017), p. 14653.

[49] Davide Fiocco, Giuseppe Foffi, and Srikanth Sastry. “Oscillatory athermal quasistatic deformation of a model glass”. In: *Physical Review E* 88.2 (2013), p. 020301.

[50] Nikolai V Priezjev. “Accelerated relaxation in disordered solids under cyclic loading with alternating shear orientation”. In: *Journal of Non-Crystalline Solids* 525 (2019), p. 119683.

[51] Pallabi Das, Anshul DS Parmar, and Srikanth Sastry. “Annealing glasses by cyclic shear deformation”. In: *arXiv preprint arXiv:1805.12476* (2018).

[52] Nikolai V Priezjev. “The effect of cryogenic thermal cycling on aging, rejuvenation, and mechanical properties of metallic glasses”. In: *Journal of Non-Crystalline Solids* 503 (2019), pp. 131–138.

[53] Daniel J Lacks and Mark J Osborne. “Energy landscape picture of overaging and rejuvenation in a sheared glass”. In: *Physical review letters* 93.25 (2004), p. 255501.

[54] Obioma U Uche, Frank H Stillinger, and Salvatore Torquato. “Constraints on collective density variables: Two dimensions”. In: *Physical Review E* 70.4 (2004), p. 046122.

[55] Robert D Batten, Frank H Stillinger, and Salvatore Torquato. “Classical disordered ground states: Super-ideal gases and stealth and equi-luminous materials”. In: *Journal of Applied Physics* 104.3 (2008), p. 033504.

[56] Andrea Gabrielli, Michael Joyce, and Francesco Sylos Labini. “Glass-like universe: Real-space correlation properties of standard cosmological models”. In: *Physical Review D* 65.8 (2002), p. 083523.

[57] Aleksandar Donev, Salvatore Torquato, and Frank H Stillinger. “Pair correlation function characteristics of nearly jammed disordered and ordered hard-sphere packings”. In: *Physical Review E* 71.1 (2005), p. 011105.

[58] Monica Skoge et al. “Packing hyperspheres in high-dimensional Euclidean spaces”. In: *Physical Review E* 74.4 (2006), p. 041127.

[59] Chase E Zachary, Yang Jiao, and Salvatore Torquato. “Hyperuniform long-range correlations are a signature of disordered jammed hard-particle packings”. In: *Physical review letters* 106.17 (2011), p. 178001.

[60] Yang Jiao and Salvatore Torquato. “Maximally random jammed packings of Platonic solids: Hyperuniform long-range correlations and isostaticity”. In: *Physical Review E* 84.4 (2011), p. 041309.

[61] Duyu Chen, Yang Jiao, and Salvatore Torquato. “Equilibrium phase behavior and maximally random jammed state of truncated tetrahedra”. In: *The Journal of Physical Chemistry B* 118.28 (2014), pp. 7981–7992.

[62] Leonardo E Silbert and Moises Silbert. “Long-wavelength structural anomalies in jammed systems”. In: *Physical Review E* 80.4 (2009), p. 041304.

[63] Ludovic Berthier et al. “Suppressed compressibility at large scale in jammed packings of size-disperse spheres”. In: *Physical review letters* 106.12 (2011), p. 120601.

[64] Rei Kurita and Eric R Weeks. “Incompressibility of polydisperse random-close-packed colloidal particles”. In: *Physical Review E* 84.3 (2011), p. 030401.

[65] Remi Dreyfus et al. “Diagnosing hyperuniformity in two-dimensional, disordered, jammed packings of soft spheres”. In: *Physical Review E* 91.1 (2015), p. 012302.

[66] Joshua Ricouvier et al. “Optimizing hyperuniformity in self-assembled bidisperse emulsions”. In: *Physical review letters* 119.20 (2017), p. 208001.

[67] Salvatore Torquato, A Scardicchio, and Chase E Zachary. “Point processes in arbitrary dimension from fermionic gases, random matrix theory, and number theory”. In: *Journal of Statistical Mechanics: Theory and Experiment* 2008.11 (2008), P11019.

[68] Salvatore Torquato, Ge Zhang, and Frank H Stillinger. “Ensemble theory for stealthy hyperuniform disordered ground states”. In: *Physical Review X* 5.2 (2015), p. 021020.

[69] Ge Zhang, Frank H Stillinger, and Salvatore Torquato. “Ground states of stealthy hyperuniform potentials: I. Entropically favored configurations”. In: *Physical Review E* 92.2 (2015), p. 022119.

[70] Ge Zhang, Frank H Stillinger, and Salvatore Torquato. “Ground states of stealthy hyperuniform potentials. II. Stacked-slider phases”. In: *Physical Review E* 92.2 (2015), p. 022120.

[71] ML Metha. “Random Matrices Academic Press”. In: *New York* (1991).

[72] Freeman J Dyson. “Correlations between eigenvalues of a random matrix”. In: *Communications in Mathematical Physics* 19.3 (1970), pp. 235–250.

[73] Robert L Jack, Ian R Thompson, and Peter Sollich. “Hyperuniformity and phase separation in biased ensembles of trajectories for diffusive systems”. In: *Physical review letters* 114.6 (2015), p. 060601.

[74] Daniel Hexner and Dov Levine. “Hyperuniformity of critical absorbing states”. In: *Physical review letters* 114.11 (2015), p. 110602.

[75] Joost H Weijs et al. “Emergent hyperuniformity in periodically driven emulsions”. In: *Physical review letters* 115.10 (2015), p. 108301.

[76] Elsen Tjhung and Ludovic Berthier. “Hyperuniform density fluctuations and diverging dynamic correlations in periodically driven colloidal suspensions”. In: *Physical review letters* 114.14 (2015), p. 148301.

[77] Daniel Hexner, Paul M Chaikin, and Dov Levine. “Enhanced hyperuniformity from random reorganization”. In: *Proceedings of the National Academy of Sciences* 114.17 (2017), pp. 4294–4299.

[78] Daniel Hexner and Dov Levine. “Noise, diffusion, and hyperuniformity”. In: *Physical review letters* 118.2 (2017), p. 020601.

[79] Salvatore Torquato and Frank H Stillinger. “Local density fluctuations, hyperuniformity, and order metrics”. In: *Physical Review E* 68.4 (2003), p. 041113.

[80] Erdal C Oğuz et al. “Hyperuniformity of quasicrystals”. In: *Physical Review B* 95.5 (2017), p. 054119.

[81] D Levesque, J-J Weis, and JL Lebowitz. “Charge fluctuations in the two-dimensional one-component plasma”. In: *Journal of Statistical Physics* 100.1-2 (2000), pp. 209–222.

[82] G Zhang, FH Stillinger, and S Torquato. “The perfect glass paradigm: Disordered hyperuniform glasses down to absolute zero”. In: *Scientific reports* 6 (2016), p. 36963.

[83] Andrea Gabrielli. “Point processes and stochastic displacement fields”. In: *Physical Review E* 70.6 (2004), p. 066131.

[84] Andrea Gabrielli, Michael Joyce, and Salvatore Torquato. “Tilings of space and superhomogeneous point processes”. In: *Physical Review E* 77.3 (2008), p. 031125.

[85] A Gabrielli et al. “Generation of primordial cosmological perturbations from statistical mechanical models”. In: *Physical Review D* 67.4 (2003), p. 043506.

[86] Chase E Zachary and Salvatore Torquato. “Anomalous local coordination, density fluctuations, and void statistics in disordered hyperuniform many-particle ground states”. In: *Physical Review E* 83.5 (2011), p. 051133.

[87] Jaeuk Kim and Salvatore Torquato. “Effect of imperfections on the hyperuniformity of many-body systems”. In: *Physical Review B* 97.5 (2018), p. 054105.

[88] Steven Atkinson et al. “Critical slowing down and hyperuniformity on approach to jamming”. In: *Physical Review E* 94.1 (2016), p. 012902.

[89] Yegang Wu, Peter Olsson, and S Teitel. “Search for hyperuniformity in mechanically stable packings of frictionless disks above jamming”. In: *Physical Review E* 92.5 (2015), p. 052206.

[90] Atsushi Ikeda, Ludovic Berthier, and Giorgio Parisi. “Large-scale structure of randomly jammed spheres”. In: *Physical Review E* 95.5 (2017), p. 052125.

[91] Leonard S Ornstein. “Accidental deviations of density and opalescence at the critical point of a single substance”. In: *Proc. Akad. Sci.* 17 (1914), p. 793.

[92] Yang Jiao et al. “Avian photoreceptor patterns represent a disordered hyperuniform solution to a multiscale packing problem”. In: *Physical Review E* 89.2 (2014), p. 022721.

[93] B Jancovici. “Exact results for the two-dimensional one-component plasma”. In: *Physical Review Letters* 46.6 (1981), p. 386.

[94] Enrique Lomba, Jean-Jacques Weis, and Salvatore Torquato. “Disordered hyperuniformity in two-component nonadditive hard-disk plasmas”. In: *Physical Review E* 96.6 (2017), p. 062126.

[95] Fausto Martelli et al. “Large-scale structure and hyperuniformity of amorphous ices”. In: *Physical review letters* 119.13 (2017), p. 136002.

[96] Sven Lübeck. “Universal scaling behavior of non-equilibrium phase transitions”. In: *International Journal of Modern Physics B* 18.31n32 (2004), pp. 3977–4118.

[97] Yuanjian Zheng and Massimo Pica Ciamarra. “Spatio-temporal Heterogeneity and Hyperuniformity in 2D Conserved Lattice Gas”. In: *arXiv preprint arXiv:2009.07187* (2020).

[98] Michela Rossi, Romualdo Pastor-Satorras, and Alessandro Vespignani. “Universality class of absorbing phase transitions with a conserved field”. In: *Physical review letters* 85.9 (2000), p. 1803.

[99] Laurent Corte et al. “Random organization in periodically driven systems”. In: *Nature Physics* 4.5 (2008), pp. 420–424.

[100] Charles Reichhardt and CJ Olson Reichhardt. “Random organization and plastic depinning”. In: *Physical review letters* 103.16 (2009), p. 168301.

[101] Andreas Mayer et al. “How a well-adapted immune system is organized”. In: *Proceedings of the National Academy of Sciences* 112.19 (2015), pp. 5950–5955.

[102] Marian Florescu, Salvatore Torquato, and Paul J Steinhardt. “Designer disordered materials with large, complete photonic band gaps”. In: *Proceedings of the National Academy of Sciences* 106.49 (2009), pp. 20658–20663.

[103] Marian Florescu, Paul J Steinhardt, and Salvatore Torquato. “Optical cavities and waveguides in hyperuniform disordered photonic solids”. In: *Physical Review B* 87.16 (2013), p. 165116.

[104] Weining Man et al. “Isotropic band gaps and freeform waveguides observed in hyperuniform disordered photonic solids”. In: *Proceedings of the National Academy of Sciences* 110.40 (2013), pp. 15886–15891.

[105] Mikael C Rechtsman and Salvatore Torquato. “Effective dielectric tensor for electromagnetic wave propagation in random media”. In: *Journal of Applied Physics* 103.8 (2008), p. 084901.

[106] Bi-Yi Wu, Xin-Qing Sheng, and Yang Hao. “Effective media properties of hyperuniform disordered composite materials”. In: *PloS one* 12.10 (2017), e0185921.

[107] Olivier Leseur, Romain Pierrat, and Rémi Carminati. “High-density hyperuniform materials can be transparent”. In: *Optica* 3.7 (2016), pp. 763–767.

[108] Ge Zhang, Frank H Stillinger, and Salvatore Torquato. “Transport, geometrical, and topological properties of stealthy disordered hyperuniform two-phase systems”. In: *The Journal of chemical physics* 145.24 (2016), p. 244109.

[109] Quan Le Thien et al. “Enhanced pinning for vortices in hyperuniform pinning arrays and emergent hyperuniform vortex configurations with quenched disorder”. In: *Physical Review B* 96.9 (2017), p. 094516.

[110] S Torquato. “Modeling of physical properties of composite materials”. In: *International Journal of Solids and Structures* 37.1-2 (2000), pp. 411–422.

[111] Yaopengxiao Xu et al. “Microstructure and mechanical properties of hyperuniform heterogeneous materials”. In: *Physical Review E* 96.4 (2017), p. 043301.

[112] Aleksandar Donev, Frank H Stillinger, and Salvatore Torquato. “Unexpected density fluctuations in jammed disordered sphere packings”. In: *Physical review letters* 95.9 (2005), p. 090604.

[113] Chase E Zachary, Yang Jiao, and Salvatore Torquato. “Hyperuniformity, quasi-long-range correlations, and void-space constraints in maximally random jammed particle packings. I. Polydisperse spheres”. In: *Physical Review E* 83.5 (2011), p. 051308.

[114] Chase E Zachary, Yang Jiao, and Salvatore Torquato. “Hyperuniformity, quasi-long-range correlations, and void-space constraints in maximally random jammed particle packings. II. Anisotropy in particle shape”. In: *Physical Review E* 83.5 (2011), p. 051309.

[115] Thomas K Haxton, Michael Schmiedeberg, and Andrea J Liu. “Universal jamming phase diagram in the hard-sphere limit”. In: *Physical Review E* 83.3 (2011), p. 031503.

[116] Jikai Wang, Jennifer M Schwarz, and Joseph D Paulsen. “Hyperuniformity with no fine tuning in sheared sedimenting suspensions”. In: *Nature communications* 9.1 (2018), pp. 1–7.

[117] Ido Regev et al. “Reversibility and criticality in amorphous solids”. In: *Nature communications* 6.1 (2015), pp. 1–8.

[118] AB Bhatia and DE Thornton. “Structural aspects of the electrical resistivity of binary alloys”. In: *Physical Review B* 2.8 (1970), p. 3004.

[119] Michael A. Klatt et al. “Universal hidden order in amorphous cellular geometries”. In: *Nature Communications* 10.1 (Feb. 2019). DOI: 10.1038/s41467-019-08360-5. URL: https://doi.org/10.1038/s41467-019-08360-5.

[120] Yuanjian Zheng, Yan-Wei Li, and Massimo Pica Ciamarra. “Hyperuniformity and density fluctuations at a rigidity transition in a model of biological tissues”. In: *Soft Matter* (2020).

[121] Duyu Chen, Enrique Lomba, and Salvatore Torquato. “Binary mixtures of charged colloids: a potential route to synthesize disordered hyperuniform materials”. In: *Physical Chemistry Chemical Physics* 20.26 (2018), pp. 17557–17562.

[122] Salvatore Torquato. “Hyperuniform states of matter”. In: *Physics Reports* 745 (June 2018), pp. 1–95. DOI: 10.1016/j.physrep.2018.03.001. URL: https://doi.org/10.1016/j.physrep.2018.03.001.

[123] Alexandros Chremos and Jack F. Douglas. “Particle localization and hyperuniformity of polymer-grafted nanoparticle materials”. In: *Annalen der Physik* 529.5 (Mar. 2017), p. 1600342. DOI: 10.1002/andp.201600342. URL: https://doi.org/10.1002/andp.201600342.

[124] Alexandros Chremos and Jack F. Douglas. “Hidden Hyperuniformity in Soft Polymeric Materials”. In: *Physical Review Letters* 121.25 (Dec. 2018). DOI: 10.1103/physrevlett.121.258002. URL: https://doi.org/10.1103/physrevlett.121.258002.

[125] Alexandros Chremos. “Design of nearly perfect hyperuniform polymeric materials”. In: *The Journal of Chemical Physics* 153.5 (Aug. 2020), p. 054902. DOI: 10.1063/5.0017861. URL: https://doi.org/10.1063/5.0017861.

[126] Weining Man et al. “Photonic band gap in isotropic hyperuniform disordered solids with low dielectric contrast”. In: *Optics express* 21.17 (2013), pp. 19972–19981.

[127] Ning Xu et al. “Anharmonic and quasi-localized vibrations in jammed solids—Modes for mechanical failure”. In: *EPL (Europhysics Letters)* 90.5 (2010), p. 56001.

[128] Prasenjit Das, Valery Ilyin, and Itamar Procaccia. “Instabilities of time-averaged configurations in thermal glasses”. In: *Physical Review E* 100.6 (2019), p. 062103.

[129] M Lisa Manning and Andrea J Liu. “Vibrational modes identify soft spots in a sheared disordered packing”. In: *Physical Review Letters* 107.10 (2011), p. 108302.

[130] HL Peng, MZ Li, and WH Wang. “Structural signature of plastic deformation in metallic glasses”. In: *Physical review letters* 106.13 (2011), p. 135503.

[131] Emanuele Boattini, Marjolein Dijkstra, and Laura Filion. “Unsupervised learning for local structure detection in colloidal systems”. In: *The Journal of chemical physics* 151.15 (2019), p. 154901.

[132] Emanuele Boattini et al. “Autonomously revealing hidden local structures in supercooled liquids”. In: *Nat. Commun.* 11.5479 (2020).

[133] Samuel S Schoenholz et al. “A structural approach to relaxation in glassy liquids”. In: *Nature Physics* 12.5 (2016), pp. 469–471.

[134] Ekin D Cubuk et al. “Identifying structural flow defects in disordered solids using machine-learning methods”. In: *Physical review letters* 114.10 (2015), p. 108001.

[135] Duane C Wallace. “On the role of density fluctuations in the entropy of a fluid”. In: *The Journal of chemical physics* 87.4 (1987), pp. 2282–2284.

[136] Craig E Maloney and Anaël Lemaıtre. “Amorphous systems in athermal, quasistatic shear”. In: *Physical Review E* 74.1 (2006), p. 016118.

[137] Nikolai V Priezjev. “Reversible plastic events during oscillatory deformation of amorphous solids”. In: *Physical Review E* 93.1 (2016), p. 013001.

[138] Frederick Charles Frank. “Supercooling of liquids”. In: *Proceedings of the Royal Society of London. Series A. Mathematical and Physical Sciences* 215.1120 (1952), pp. 43–46.

[139] Hannes Jónsson and Hans C Andersen. “Icosahedral ordering in the Lennard-Jones liquid and glass”. In: *Physical review letters* 60.22 (1988), p. 2295.

[140] Toshiharu Kondo and K Tsumuraya. “Icosahedral clustering in a supercooled liquid and glass”. In: *The Journal of chemical physics* 94.12 (1991), pp. 8220–8226.

[141] Paul J Steinhardt, David R Nelson, and Marco Ronchetti. “Icosahedral bond orientational order in supercooled liquids”. In: *Physical Review Letters* 47.18 (1981), p. 1297.

[142] Jun Ding, Yong-Qiang Cheng, and Evan Ma. “Full icosahedra dominate local order in Cu64Zr34 metallic glass and supercooled liquid”. In: *Acta materialia* 69 (2014), pp. 343–354.

[143] Hua Tong and Hajime Tanaka. “Revealing hidden structural order controlling both fast and slow glassy dynamics in supercooled liquids”. In: *Physical Review X* 8.1 (2018), p. 011041.

[144] Chengjie Xia et al. “The structural origin of the hard-sphere glass transition in granular packing”. In: *Nature communications* 6.1 (2015), pp. 1–9.

[145] AV Anikeenko and NN Medvedev. “Polytetrahedral nature of the dense disordered packings of hard spheres”. In: *Physical review letters* 98.23 (2007), p. 235504.

[146] Benoit Charbonneau, Patrick Charbonneau, and Gilles Tarjus. “Geometrical frustration and static correlations in a simple glass former”. In: *Physical review letters* 108.3 (2012), p. 035701.

[147] Hajime Tanaka et al. “Revealing key structural features hidden in liquids and glasses”. In: *Nature Reviews Physics* 1.5 (2019), pp. 333–348.

[148] Ian H Bell, Jeppe C Dyre, and Trond S Ingebrigtsen. “Excess-entropy scaling in supercooled binary mixtures”. In: *Nature communications* 11.1 (2020), pp. 1–12.

[149] K Lawrence Galloway et al. “Scaling of relaxation and excess entropy in plastically deformed amorphous solids”. In: *Proceedings of the National Academy of Sciences* 117.22 (2020), pp. 11887–11893.

[150] Yaakov Rosenfeld. “Relation between the transport coefficients and the internal entropy of simple systems”. In: *Physical Review A* 15.6 (1977), p. 2545.

[151] Yaakov Rosenfeld. “A quasi-universal scaling law for atomic transport in simple fluids”. In: *Journal of Physics: Condensed Matter* 11.28 (1999), p. 5415.

[152] Jeppe C Dyre. “Perspective: Excess-entropy scaling”. In: *The Journal of chemical physics* 149.21 (2018), p. 210901.

[153] Alex Malins et al. “Lifetimes and lengthscales of structural motifs in a model glassformer”. In: *Faraday discussions* 167 (2013), pp. 405–423.

[154] Charles Spearman. “The proof and measurement of association between two things.” In: (1961).

[155] Himangsu Bhaumik, Giuseppe Foffi, and Srikanth Sastry. “The role of annealing in determining the yielding behavior of glasses under cyclic shear deformation”. In: *arXiv preprint arXiv:1911.12957* (2019).

[156] Ido Regev, Turab Lookman, and Charles Reichhardt. “Onset of irreversibility and chaos in amorphous solids under periodic shear”. In: *Physical Review E* 88.6 (2013), p. 062401.

[157] Nikolai V Priezjev. “Shear band formation in amorphous materials under oscillatory shear deformation”. In: *Metals* 10.3 (2020), p. 300.

[158] Vishwas Venkatesh Vasisht, Gabrielle Roberts, and Emanuela Del Gado. “Emergence and persistence of flow inhomogeneities in the yielding and fluidization of dense soft solids”. In: *Physical Review E* 102.1 (2020), p. 010604.

[159] Vishwas V Vasisht and Emanuela Del Gado. “Computational study of transient shear banding in soft jammed solids”. In: *Physical Review E* 102.1 (2020), p. 012603.

[160] Erin G Teich et al. “Crystalline shielding mitigates structural rearrangement and localizes memory in jammed systems under oscillatory shear”. In: *arXiv preprint arXiv:2004.06065* (2020).

[161] W Klement, RH Willens, and POL Duwez. “Non-crystalline structure in solidified gold–silicon alloys”. In: *Nature* 187.4740 (1960), pp. 869–870.

[162] Simon A Rogers et al. “A sequence of physical processes determined and quantified in LAOS: Application to a yield stress fluid”. In: *Journal of rheology* 55.2 (2011), pp. 435–458.

[163] Thomas Gibaud et al. “Multiple yielding processes in a colloidal gel under large amplitude oscillatory stress”. In: *Soft Matter* 12.6 (2016), pp. 1701–1712.

[164] Nathan C Keim and Sidney R Nagel. “Generic transient memory formation in disordered systems with noise”. In: *Physical review letters* 107.1 (2011), p. 010603.

[165] Davide Fiocco, Giuseppe Foffi, and Srikanth Sastry. “Encoding of memory in sheared amorphous solids”. In: *Physical review letters* 112.2 (2014), p. 025702.

[166] John R Royer and Paul M Chaikin. “Precisely cyclic sand: Self-organization of periodically sheared frictional grains”. In: *Proceedings of the National Academy of Sciences* 112.1 (2015), pp. 49–53.

[167] Sam Wilken et al. “Hyperuniform structures formed by shearing colloidal suspensions”. In: *Physical Review Letters* 125.14 (2020), p. 148001.

[168] Salvatore Torquato. “Hyperuniformity and its generalizations”. In: *Physical Review E* 94.2 (2016), p. 022122.

[169] Qi Wang and Anubhav Jain. “A transferable machine-learning framework linking interstice distribution and plastic heterogeneity in metallic glasses”. In: *Nature communications* 10.1 (2019), pp. 1–11.

[170] K Dawson et al. “Higher-order glass-transition singularities in colloidal systems with attractive interactions”. In: *Physical Review E* 63.1 (2000), p. 011401.

[171] Gary L Hunter and Eric R Weeks. “The physics of the colloidal glass transition”. In: *Reports on progress in physics* 75.6 (2012), p. 066501.

[172] KN Pham et al. “Yielding of colloidal glasses”. In: *EPL (Europhysics Letters)* 75.4 (2006), p. 624.

[173] Pawel Koziatek. “Atomistic contribution to the understanding of metallic and silica glasses”. PhD thesis. 2014.

[174] Göran Wahnström. “Molecular-dynamics study of a supercooled two-component Lennard-Jones system”. In: *Physical Review A* 44.6 (1991), p. 3752.

[175] Walter Kob and Hans C Andersen. “Testing mode-coupling theory for a supercooled binary Lennard-Jones mixture I: The van Hove correlation function”. In: *Physical Review E* 51.5 (1995), p. 4626.

[176] Kai Zhang et al. “Beyond packing of hard spheres: The effects of core softness, non-additivity, intermediate-range repulsion, and many-body interactions on the glass-forming ability of bulk metallic glasses”. In: *The Journal of chemical physics* 143.18 (2015), p. 184502.

[177] Steve Plimpton. *Fast parallel algorithms for short-range molecular dynamics*. Tech. rep. http://lammps.sandia.gov. Sandia National Labs., Albuquerque, NM (United States), 1993.

[178] Craig Maloney and Anael Lemaitre. “Subextensive scaling in the athermal, quasistatic limit of amorphous matter in plastic shear flow”. In: *Physical review letters* 93.1 (2004), p. 016001.

université PARIS-SACLAY | ÉCOLE DOCTORALE Physique en l'Île-de-France (PIF)

Titre : Modifications structurelles des verres sous déformation périodique par cisaillement

Mots clés : rhéologie, systèmes vitreux, hyperuniformité, structure locale, bande de cisaillement, matière molle, yielding, simulation

Résumé : Dans cette thèse, nous avons étudié les changements structurels des verres subissant des déformations périodiques. Nous avons utilisé la dynamique moléculaire pour échantillonner des configurations liquides équilibrées de modèles de formation de verre binaire, puis cisaillé le système en utilisant un protocole quasi statique athermique avec des amplitudes maximales γ_{max}. À une certian valeur $\gamma_{max} = \gamma_y$, le systéme céde, ce qui se manifeste par une transition de l'état absorbant à l'état diffusif. A l'état diffusif, le systéme consiste en une bande de cisaillement qui est un sous-volume localisé de deformation élevée du système. Le but de la thèse était d'examiner les changements dans les propriétés structurelles dans les états stationnaires de cisaillement cyclique à travers cette yielding transition.

La caractéristique structure à longue portée est caractérisée par "l'hyperuniformité", qui décrit la suppression des fluctuations de densité. Nos résultats montrent que dans les états absorbants, le verre est hyperuniforme et au-dessus, le système se divise en deux phases hyperuniformes séparées par une interface qui coïncide avec la limite de la bande de cisaillement. Par conséquent, dans les sous-volumes à l'intérieur et à l'extérieur de la bande, nous avons une hyperuniformité mais dans la direction perpendiculaire à la bande, l'hyperuniformité est perdue.

L'ordre structurel local a été examiné en calculant l'entropie excédentaire à deux corps par particule S_2 et la tétraédricité dans la structure local n_{tet}. Il a été constaté que les états absorbants ont un ordre local moyen plus élevé. De plus, à l'état stationnaire, les particules participant à des réarrangements plastiques plus importants ont en moyenne un ordre structurel local inférieur. En particulier, les particules engages dans 12 tétraèdres ($n_{tet} = 12$), associées à une empilement icosaédrique, tendent à rester immobile. En analysant le système en présence d'une bande de cisaillement, nous constatons que près de 30% des particules sont impliquées dans un agencement icosaédrique local hors de la bande de cisaillement alors que cette fraction tombe à < 5 % dans la bande de cisaillement. Ce résultat marque la différence dispositions structurelles à l'intérieur et à l'extérieur de la bande de cisaillement.

Title : Structural changes in glasses under periodic shear deformation

Keywords : rheology, glassy systems, hyperuniformity, local structure, shear band, soft matter , yielding, simulation

Abstract : In this thesis we have investigated structural changes in glasses undergoing periodic deformation. We have used molecular dynamics for sampling equilibrated liquid configurations of binary glass forming models and then sheared the system using athermal quasi static protocol with strain amplitudes γ_{max}. At a certain value of $\gamma_{max} = \gamma_y$ the system yields, identified by a transition from absorbing to diffusive state. In diffusive state the system consists a shear band which is a high strain localized subvolume of the system. The purpose of the thesis has been to examine changes in structural properties in steady states of cyclic shear across this yielding transition.

Long range structural feature is characterised by "Hyperuniformity", which describes suppression of density fluctuations. Our results show that in absorbing states the glass is hyperuniform and above yielding the system splits into two hyperuniform phases separated by an interface which coincides with the boundary of the shear band. Therefore, in the sub-volumes inside and outside the band we have hyperuniformity but in the direction perpendicular to the band, the hyperuniformity is lost.

Local structural order was examined by computing per particle two-body excess entropy S_2 and tetrahedrality in local structure n_{tet} . It was found that absorbing states have higher mean local order. Additionally, in steady state particles participating in larger plastic rearrangements on the average have lower local structural order. Specially particles with $n_{tet} = 12$, a number associated to icosahedral clustering, prefer to remain immobile. As we analysed the system in presence of shear band, we find that outside shear band almost 30% of the particles have local icosahedral clustering whereas inside shear band this percentage is very low (below 5 %) This result marks the different structural arrangements inside and outside shear band.